

# TURBINE BLADE INTERNAL HEAT TRANSFER AND FILM COOLING STUDIES

A Dissertation

by

NIAN WANG

Submitted to the Office of Graduate and Professional Studies of  
Texas A&M University  
in partial fulfillment of the requirements for the degree of

DOCTOR OF PHILOSOPHY

Chair of Committee,	Je-Chin Han
Committee Members,	Yassin A. Hassan
	Alan Palazzolo
	Sy-Bor Wen
Head of Department,	Andreas A. Polycarpou

December 2018

Major Subject: Mechanical Engineering

Copyright 2018 Nian Wang

## ABSTRACT

Gas turbine engines are widely used in many industrial applications including aircraft propulsion, land-based power generation, and marine oil & gas industries. Currently, the highest turbine inlet temperature is around 1700°C. This turbine inlet temperature has already exceeded the yielding point of the blade material (1200°C). Therefore, advanced cooling techniques are employed to protect the hot-gas-path components from being heated and also ensure the long-lasting operation of gas turbines. In this study, experiments on the leading edge jet impingement cooling (first part), the flat plate film cooling (second part) and the endwall film cooling (third part) with more realistic features are proposed to improve the turbine airfoil cooling design.

The first part studies the impinging jet position effects (normal jet and tangential jet) and camera viewing angle effects. The impingement heat transfer distribution on the target wall is expected to obtain by using the transient liquid crystal (TLC) technique. Jet Reynolds numbers, 10,000, 20,000 and 30,000, based on the jet hole diameter, will be tested respectively. Numerical simulations using RANS will be carried out to explore the flow physics inside the impingement cavity.

The second part is focused on the film cooling effectiveness of two-row compound angled cylindrical holes by using the pressure sensitive paint (PSP) technique. The coolant-to-mainstream density ratio (DR) includes DR = 1.0 (low-temperature experiments), DR = 1.5 (intermediate DR) and DR = 2.0 (close to engine conditions) will be evaluated. Film cooling effectiveness distribution on the flat plate and the area-averaged film cooling effectiveness will be presented and compared for the optimization of the two-row compound cylindrical cooling hole design.

The third part investigates the endwall film cooling from two different cooling hole patterns: mid-chord row and downstream row. The isentropic exit Mach number will be at 0.5 corresponding to inlet Reynolds number of 380,000, based on the axial chord length of the vane. The free-stream turbulence intensity will be kept at 19%. This study will discuss the effects of the upstream injection flow to the endwall film cooling.

## DEDICATION

To the people for who cared me, helped and loved me

## ACKNOWLEDGEMENTS

I would like to express my appreciation to the committee chair, Dr. Han, and the committee members, Dr. Hassan, Dr. Palazzolo, and Dr. Wen for giving their precious time. Sincerely thanks to Dr. Han for his professional and patient direction, helpful suggestion, and warm consideration during the research.

Great thanks to Dr. Mingjie Zhang, Dr. Andrew F Chen and Dr. Chao-Cheng Shiau for teaching me to do experiments, writing the paper and providing technical help when I always got difficulties. Also appreciate the previous, current colleagues and visiting scholars met in the Turbine Heat Transfer Laboratory. Wish you all have a bright future and a beautiful life.

Thanks to the Department of Mechanical Engineering and ASME IGTI Student Advisory Committee for providing me travel fund to the 2018 Turbo Expo. Thanks to the faculty and staff from the Department of Mechanical Engineering and the technicians in the Physics Machine Shop. This research cannot be completed without their help and support.

## CONTRIBUTORS AND FUNDING SOURCES

### **Contributors**

This research was supported by a thesis (or) dissertation committee consisting of Professor Je-Chin Han, Professor Alan Palazzolo and Professor Sy-Bor Wen of the Department of Mechanical Engineering and Professor Yassin A. Hassan of the Department of Nuclear Engineering.

All study for the thesis (or) dissertation was completed by the student, in collaboration with Mingjie Zhang, Andrew F Chen and Chao-Cheng Shiau of the Department of Mechanical Engineering.

### **Funding Sources**

This work was supported through the Marcus Easterling endowment fund. The numerical simulations were supported by High Performance Research Computing of Texas A&M University.

## NOMENCLATURE

A	Area [m <sup>2</sup> ]
AOI	Area of interest
C	Vane chord length [m]; concentration by volume [-]
CCD	Charge-coupled device
DAQ	Data acquisition system
D	Leading edge impingement target surface diameter
DR	Coolant-to-mainstream density ratio = $\rho_c/\rho_m$ [-]
d	Jet hole diameter; Cooling hole diameter, jet hole diameter [m]
e	Slot height [cm]
h	Heat transfer coefficient [W/m <sup>2</sup> ·K]
I	Intensity [-]
k	Conductivity
l	Film cooling hole length
L	Length [m]
LE	Leading edge of vane; three rows of leading edge cooling holes
LED	Light-emitting device
M	Blowing ratio = $\rho_c V_c / \rho_m V_m$ [-]
Ma	Mach number [-]
N	Number of jet holes
MFR	Coolant-to-mainstream mass flow ratio = $\dot{m}_c/\dot{m}_m$ [-]
OD	Outside diameter

P	Pressure [Pa]
p	Hole-to-hole spacing
R	Radius of target surface [cm]
Re	Reynolds number
s	Jet-to-jet spacing; row-to-row spacing of cooling holes [m]
T	Temperature [°C]
t	Time [s]
Tu	Turbulence intensity [%]
v	Velocity [m/s]
W	Width[cm]; Molecular weight [kg]
X	Distance from the leading edge of hardware [m]; Span-wise direction
Z	Jet to target surface distance ( $z = R+e$ ); Normal direction

### **Greek Symbols**

$\alpha$	Thermal diffusivity [m <sup>2</sup> /s]; Axial angle to the mainstream [°]
$\beta$	Compound angle to the mainstream [°]
$\theta$	Angle on test surface [°]
$\gamma$	Specific heat ratio [-]
k	Thermal conductivity [W/m·K]
$\eta$	Film cooling effectiveness [-]
$\rho$	Fluid density [kg/m <sup>3</sup> ]
$\mu$	Fluid dynamic viscosity [Pa·s]

### **Subscripts**

air	Property with air injection
-----	-----------------------------



avg	Area-averaged
ax	Axial
b	Black condition
c	Coolant
fg	Property with foreign gas injection
i	Initial
j	Jet
is	Isentropic
m	Mainstream
ref	Reference condition
w	Impermeable wall

# TABLE OF CONTENTS

	Page
ABSTRACT.....	ii
DEDICATION.....	iv
ACKNOWLEDGEMENTS.....	v
CONTRIBUTORS AND FUNDING SOURCES .....	vi
NOMENCLATURE .....	vii
TABLE OF CONTENTS.....	x
LIST OF FIGURES .....	xii
LIST OF TABLES .....	xv
1. INTRODUCTION .....	1
1.1 Literature Review on Turbine Blade Leading Edge Jet Impingement .....	3
1.2 Literature Review on Turbine Blade Flat Plate Film Cooling.....	6
1.3 Literature Review on Turbine Blade Endwall Film Cooling.....	9
1.4 Conclusions.....	10
2. TURBINE BLADE LEADING EDGE COOLING WITH ONE ROW NORMAL OR TANGENTIAL IMPINGING JETS .....	13
2.1 Experimental Setup and Method.....	13
2.2 Numerical Setup and Method .....	30
2.3 Test Matrix.....	33
2.4 Results and Discussion .....	34
2.5 Conclusions.....	48
3. FILM COOLING EFFECTIVENESS FROM TWO-ROW OF COMPOUND ANGLED CYLINDRICAL HOLES USING PSP TECHNIQUE .....	49
3.1 Experimental Setup and Method.....	49
3.2 Test Matrix.....	56
3.3 Results and Discussion .....	58
3.4 Conclusions.....	77

	Page
4. TURBINE VANE ENDWALL FILM COOLING FROM MID-CHORD OR DOWNSTREAM ROWS AND UPSTREAM COOLANT INJECTION .....	79
4.1 Experimental Setup and Method.....	79
4.2 Test Matrix.....	83
4.3 Results and Discussion .....	85
4.4 Conclusions.....	97
5. SUMMARY .....	99
REFERENCES .....	101

## LIST OF FIGURES

	Page
Figure 1 Typical gas turbine cooling schematic for (a) internal cooling and (b) external (film) cooling [1] .....	2
Figure 2 Schematic diagram of the test facility .....	14
Figure 3 Schematic diagram of the air loop and test setup .....	16
Figure 4 Configuration of jet plate.....	18
Figure 5 Jet-hole position and flow direction .....	18
Figure 6 Mainstream temperature variation with time .....	20
Figure 7 Curved surface calibration test setup.....	22
Figure 8 Coordinate transformation from image to surface.....	24
Figure 9 Calibration curves for viewing angle $90^\circ$ .....	26
Figure 10 Calibration curves for viewing angle $45^\circ$ .....	26
Figure 11 Calibration curves effect at viewing angle $90^\circ$ .....	28
Figure 12 Calibration curves effect at viewing angle $45^\circ$ .....	28
Figure 13 Corrected results of two viewing angles .....	28
Figure 14 Data comparison with published correlation .....	29
Figure 15 Computational domain for two cases .....	31
Figure 16 Comparison of turbulence models at $Re = 30k$ .....	32
Figure 17 Liquid crystal image (a) normal jet impingement at $t=25s$ , viewing angle $90^\circ$ ; (b) tangential jet impingement at $t=45s$ , viewing angle $45^\circ$ .....	34
Figure 18 Detailed Nusselt number distribution (a) normal jet impingement; (b) tangential jet .	36
Figure 19 Numerical Nu contour (a) normal jet; (b) tangential jet.....	38
Figure 20 Velocity contour on YZ plane (a) normal jet; (b) tangential jet.....	40

Figure 21 Span-wise averaged Nusselt number.....	42
Figure 22 Stream-wise averaged Nusset Number.....	44
Figure 23 CFD and TLC comparison .....	46
Figure 24 Averaged Nusselt numbers ( $0^\circ < \theta < 135^\circ$ ). .....	47
Figure 25 Schematic diagram of test loop .....	50
Figure 26 Coolant feed geometry .....	50
Figure 27 Two-row designs for $p/d = 4$ .....	51
Figure 28 PSP calibration curves .....	55
Figure 29 Film cooling effectiveness distribution at DR 1.0.....	60
Figure 30 Film cooling effectiveness distribution at DR 2.0.....	61
Figure 31 Laterally averaged film-cooling effectiveness .....	63
Figure 32 Laterally averaged film-cooling effectiveness with all M.....	65
Figure 33 Film cooling effectiveness distribution of design A at DR = 1.5 .....	67
Figure 34 Film cooling effectiveness distribution of design B at DR = 1.5 .....	68
Figure 35 Effect of $p/d$ on spanwise averaged effectiveness on design A.....	70
Figure 36 Effect of $p/d$ on spanwise averaged effectiveness on design B.....	71
Figure 37 Area averaged cooling effectiveness .....	73
Figure 38 Data distribution along the proposed correlation .....	76
Figure 39 Flow loop of the endwall cascade facility .....	80
Figure 40 Schematic view of the endwall test section.....	81
Figure 41 Schematic of film-hole patterns on the endwall .....	82
Figure 42 Local film cooling effectiveness, IL=1.0%, DR=1.5 .....	86
Figure 43 Pitchwise averaged film cooling effectiveness, IL=1.0%, DR=1.5 .....	88

Figure 44 Local film cooling effectiveness, $EW=1.0\%$ , $DR=1.5$ .....	90
Figure 45 Pitchwise averaged film cooling effectiveness, $EW=1.0\%$ , $DR=1.5$ .....	92
Figure 46 Pitchwise averaged film cooling effectiveness, $IL = 1\%$ , $EW = 1\%$ .....	94
Figure 47 Area averaged film cooling effectiveness .....	96

## LIST OF TABLES

	Page
Table 1 Grid independence study .....	31
Table 2 Test matrix for leading edge jet impingement study .....	33
Table 3 Test matrix for two-row film cooling study.....	57
Table 4 Test matrix for endwall film cooling study. ....	84

## 1. INTRODUCTION

In modern gas turbines, the turbine inlet temperature (TIT) has far exceeded the melting point of the blade material. To protect the turbine blade from being damaged, many cooling techniques are used to adequately cool the gas turbine components to ensure the safety and reliability of the engine. From turbine cooling aspect, the turbine blades are cooled internally and externally. As shown in Figure 1, for internal cooling, the coolant passes through several serpentine passages inside the airfoils and remove the heat from the outside of the blades; for external cooling, the internal coolant is ejected from the discrete holes and form a thin film to protect the blade surface from the hot combustions gases.

Due to different flow and heat transfer characteristics at different regions, different cooling techniques are employed. For example, jet impinging cooling method is implemented at leading edge region; rib-roughened augmented convective cooling is used along the serpentine passage, and the pin-fin cooling is used at the trailing edge region. It is essential to understand the heat transfer behavior in the region, and then the engine cooling system can be designed to minimize the use of cooling air. After all, the cooling air is initially extracted from the compressor. There is a weigh between the usage of cooling air and the thermal efficiency. Too little coolant extraction results in higher blade temperatures and reduced components lift, while too much coolant implied a waste and cut the engine efficiency.



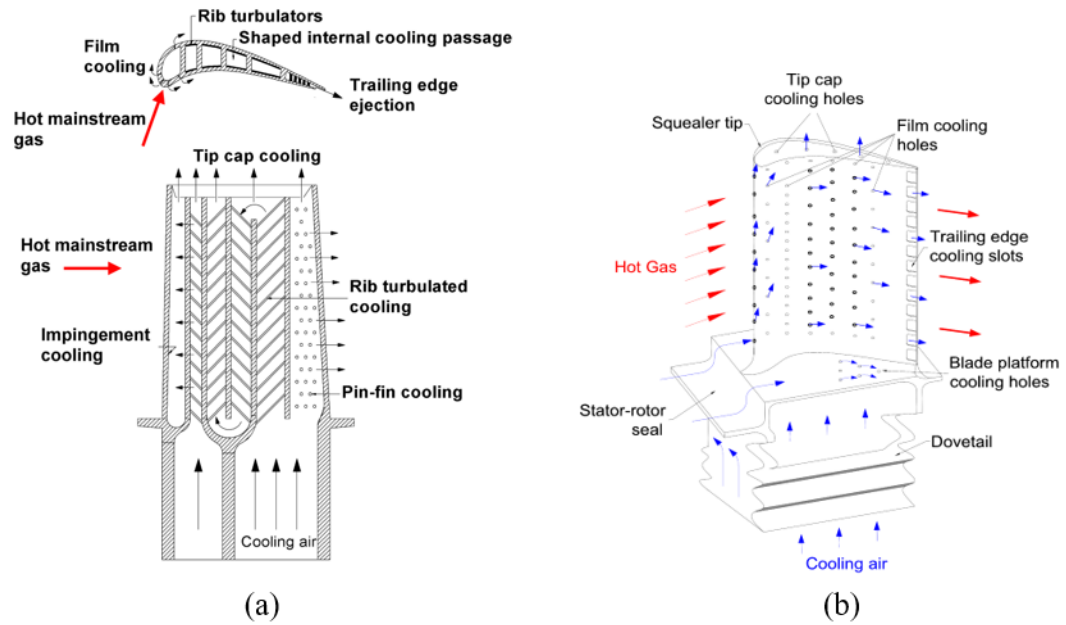


**Figure 1 Typical gas turbine cooling schematic for (a) internal cooling and (b) external (film) cooling [1]**

This study will focus on three parts: leading edge impinging cooling, the blade surface film cooling, and the endwall film cooling. For the first part, there are many geometric parameters influence the jet impinging cooling including jet Reynolds number ( $Re_j$ ), jet-to-jet spacing ( $s$ ) and jet-to-target plate spacing ( $D$ ), etc. Parameters that influence the flat plate film cooling and end wall film cooling include coolant to mainstream blowing ratio ( $M$ ), density ratio ( $DR$ ), the pitch-to-diameter ratio ( $p/d$ ). Both the flow parameters and the geometrical design of the cooling features play an essential role in the cooling performance. A comprehensive review of various effects on film cooling is documented in 1. Detail literature survey of each part and experimental methods will be presented in the following sections.

### **1.1 Literature review on turbine blade leading edge jet impingement cooling**

In turbine blade, the leading edge region suffers from very high heat load. Jet impingement cooling is utilized to keep the blade surface temperature at acceptable levels. A considerable amount of research has been carried out in the past. The heat transfer characteristics of jet impingement are summarized in several publications 2, 3 and 4.

In the early investigations, studies mainly focused on jet impingement on either flat or curved smooth surfaces. For jet impingement on a curved surface, the heat transfer correlations  $3,000 < Re < 15,000$  were experimentally obtained by Chupp et al. 5. Florschuetz et al. [6-8] developed the correlations of jet array impingement on a flat surface, which is widely used for jet impingement cooling design. Both their results suggest that jet diameter ( $d$ ), jet Reynolds number ( $Re$ ), jet-to-jet spacing ( $s$ ), jet-to-target-plate distance ( $Z$ ) are critical parameters affecting heat transfer coefficient. They also demonstrated that the presence of cross-flow reduces the heat transfer performance. The inline arrangement showed better performance by reducing the negative

effect of cross-flow. In the 1990s, the transient liquid crystal (TLC) technique was used to resolve the local detailed heat transfer distribution. Huang et al. [9] obtained the detailed heat transfer distributions of circular jets impinging on a smooth flat plate with  $Re$  from 4,800 to 18,300. They reported the cross-flow direction significantly affected the flow structure and heat transfer coefficient distribution. Flow exiting at both sides can reduce the cross-flow effect. Ekkad et al. [10] used the same experimental technique to study the combined impact of film cooling hole and cross flow. Their findings showed that with the existing film cooling holes, the cross-flow impact is reduced and the heat transfer on the surface is improved. Jordan et al. [11-13] carried out transient liquid crystal experiments to investigate the effect of jet-hole geometry (circular, racetrack, and fillets). A jet impinged on a curved target surface, which modeled the leading edge region of an airfoil. The best heat transfer performance was observed for racetrack hole.

Research on jet impingement coupled with turbulators has been developed as well. Azad et al. [14, 15] used transient liquid crystal technique to investigate jet impingement on a flat surface with pinned and dimpled turbulators. Their results indicated a pinned surface provided a higher or lower heat transfer coefficient than a smooth surface, depending on the crossflow direction. Mhetras et al. [16] studied jet impinging on a flat surface with the roughness of riblets, hemispherical dimples and short pins with  $Re$  ranging from 50,000 to 450,000. They reported that the short pinned surface provided the best heat transfer performance. Buzzard et al. [17, 18] investigated the heat transfer enhancement of jet impingement on a flat surface. Eight jet plates designed with the different combination of large pins and small rectangle were tested. Different size of triangle and rectangle turbulators were used to study the roughness shape effect.

In the open literature, most of the leading edge film cooling studies are based on the semi-cylindrical model. Cruse [16] et al. investigated various influences on turbine airfoil leading edge

film cooling. They studied  $DR = 1.8$ ,  $M = 2.0$ ,  $Tu = 0.5\%$  for circular and elliptical leading edge shapes with cylindrical holes. It was found that film cooling effectiveness distributions are similar. Chowdhury et al. [17] studied the leading edge shape effect on film cooling with radial angle cylindrical holes, including one semi-cylinder and two semi-ellipses leading edge. In the current study, cylindrical holes are changed to shaped holes. Compared with their results, we also found that shaped holes had much higher effectiveness than cylindrical holes for all the three leading edge shapes.

Many numerical simulations were carried out and compared with experimental results. Kumar et al. [19, 20] computationally studied the heat transfer of a row of circular jets impinging on concave surface with  $k-\omega$  turbulence model. Their results were 12% lower than the results of Chupp et al. 5. Ling et al. 21 obtained the surface heat transfer coefficients of a circular cooling passage with the tangential injection jets, suitable for turbine blade leading edge cooling by using the conventional TLC technique. Hot-wire anemometry measured the velocity field. The Reynolds number ranged from 7500 to 12500. Their results show that the vortex cooling system provides a more uniform heat transfer distribution in the span-wise direction through the peak heat transfer value is lower. The  $k-\epsilon$  turbulence model performed the Numerical simulation. They concluded that the heat transfer coefficient predictions from the CFD showed excellent agreement with the results via TLC for the vortex chamber. Inflow field prediction, the CFD prediction also proved a good agreement in the near-wall region but poor agreement near the core due to grid size limitation. Taslim et al. 22 performed a CFD analysis to examine the impingement heat transfer in the leading edge region while considering cross-flow effects. They found numerical results were 8% to 20% lower than experimental results by using  $v2f$  turbulence model. Xing et al. 23 experimentally and numerically studied an inline jet impinging on a micro-rib roughened flat surface at different cross-

flow conditions. SST turbulence model was used in their computations. Their CFD predictions showed remarkable agreement with experimental results for all different crossflow schemes. Liu et al. 24 numerically studied the effect of jet-hole position on a curved surface heat transfer. The SST turbulence model was employed. Their results indicated that the weighted average Nusselt number increased with the decrease of the spacing between the jet hole and the pressure side wall. It is worthy to know that their model geometry was based on the first stage rotor blade of GE-E<sup>3</sup>. Hossain et al. 25 studied the heat transfer of jet arrays impinging on a ribbed curved surface: 90° rib and W rib. The curved surface radius was 32 times the diameter of the impingement hole. They compared experimental results obtained by temperature sensitive paint and the numerical results predicted by the  $v_2f$  model. The CFD predictions showed good agreement with experimental data at  $Re = 125,000$ . Parbat et al. 26 studied impingement cooling in a rectangular cavity with surface features including airfoil shaped dimples, chevron elements on jet issuing plate and 45° degree wedges on the jet plate. Local heat transfer coefficient distribution was obtained by TLC experiments and compared with the numerical results predicted by the SST model. The numerical results were in favorable trend with the experimental results; however, the heat transfer coefficients were over-predicted.

## **1.2 Literature review on turbine blade flat plate film cooling**

Researchers have been performing film cooling measurements on the flat plate to study the heat transfer at the downstream portion of the turbine blade. Previous experimental results suggest that hole geometry and coolant/mainstream conditions are two major category factors that significantly affect film cooling effectiveness. The hole shape covers cylindrical, fan-shaped or laid-back fan-shaped, simple or compound angle, forward or laterally diffused and the hole

spacing, etc. The flow conditions include the coolant/mainstream blowing ratio and density ratio, free stream turbulence intensity and unsteady wake, etc. The influence of these parameters and significant conclusions are available in the review articles [28-33].

A single row of the cooling holes is usually employed to investigate the fundamental heat transfer on a flat plate. Some researchers [34-36] have studied the density ratio effect on film cooling effectiveness by a row of holes. They agreed that at the same blowing rate  $M$ , the film cooling effectiveness was found to increase with the density ratio. In real engine condition, the density ratio is about 2.0. Ekkad et al. 37 employed one-row cooling hole to evaluate the cooling performance of compound angle hole. Figure 1 presents the compound hole geometry,  $\alpha$  is the inclination angle, and the  $\beta$  is the compound angle. Film cooling effectiveness of three hole configurations ( $\alpha = 35^\circ$ ,  $\beta = 0^\circ$ ,  $45^\circ$ , and  $90^\circ$ ) was measured by using the transient liquid crystal technique. They reported that at higher  $M$ , the increase in  $\beta$  produces better cooling performance. Goldstein and Jin 38 used the naphthalene sublimation technique to assess the film cooling performance for one row of holes with  $\alpha = 35^\circ$  and  $\beta = 45^\circ$ . They claimed that the compound angle holes provide the better effectiveness at higher blowing ratio because of less lift-off and better coverage along the surface. The effect of hole length-to-diameter ratio ( $l/d$ ) is found to be negligible on film cooling at high turbulence 39. Chen et al. 40 studied the combined effects of the hole configurations (cylindrical, fan-shaped, simple and compound angle), blowing ratio, density ratio and turbulence intensity by one row of holes on the flat plate by using the pressure-sensitive paint technique.

In the real application, as the sharp decay in one-row film cooling hole, multi-row of the cooling holes is introduced to sustain sufficient coolant coverage along the surface. Many researchers employed the two-row of cooling holes to explore the film cooling features. Numerous

experimental results indicated the cooling performance of two-row of holes is considered more efficient in protecting the wall than a single row 41. And the cooling performance is influenced by the combined effects of injection angles, row spacing, hole spacing and turbulent intensity 42. The flow field measurement of two-row cooling holes performed by Sinha et al. 43 indicates the thicker boundary layer significantly altered the mean flow field and the turbulence as well as the shear stress fields. The thicker boundary layer at the second row resulted in higher penetration of the jets into the mainstream and should be responsible for the nature difference between one-row and two-row cooling structure. It is noted that in their experiments, the row-to-row spacing is 40 hole-diameter, which is significantly larger than typical spacing in the two-row film cooling. Ligrani et al. 44 discussed the effects of row-to-row spacing, spanwise hole spacing, pitch distance, and the hole geometry on two-row flat plates. Ahn et al. 45 described the injection behaviors from two-row of cooling holes with opposite orientation angles (first-row  $\beta = +45^\circ$  and second-row  $\beta = -45^\circ$ ). They concluded that at high blowing ratio ( $M = 1.0 \sim 2.0$ ), the inline pattern provides greater film cooling effectiveness. Jubran et al. 46, Jubran and Maitech 47, and Maitech et al. 48 studied the film cooling effectiveness from two-row of simple and compound angle holes in combination. They concluded that two staggered rows arrangement outperforms two inline rows arrangement. The combination of one simple angle hole row and one compound angle hole row in staggered arrangement tends to provide better and more uniform cooling than that of two-row compound angle holes. It is learned that the above mentioned two-row film cooling studies with compound angle cylindrical holes have not included the density ratio up to 1.5 and 2.0. And the film cooling correlations for two-row cooling holes are not given as well.

Most investigations of the flat plate film cooling focus on the single row and two-row design, the three-row film cooling study is insufficient. Yang et al. [49] studied the heat transfer

coefficient of four-hole arrangements: one-row, two-row (staggered arrangement), two-row (aligned arrangement) and three-row arrangement. Bashir et al. [50] studied the three-row compound angle cooling hole with four configurations: the inline row with equal orientation angles, the staggered row with the same orientation angles, the inline row with the opposite orientation angle and staggered row with the opposite orientation angles. Their results show that staggered with the same orientation angles and inline row with opposite angles are superior designs.

### **1.3 Literature review on turbine vane endwall film cooling**

Turbine endwall film cooling is very important due to the complicated flow field in this region including the horseshoe vortex from the incoming mainstream boundary layer that is prone to impede the coolant coverage near leading edge, as well as the secondary vortices (passage vortex, corner vortices) created by the large pressure difference between the pressure side and suction side between the endwall passage. Several studies are available in open literature describing the upstream injection behavior on endwall film cooling by coolant injection using slots or cooling hole rows. Back to 1979, some researchers found that the near-endwall cooling performs not effective in the mid-passage region where the hot gases maybe most detrimental. Studies from Blair 55 and Granser and Schulenberg 56 concluded that with the upstream slot injection, the secondary flow in the passage had been reduced due to the reduced boundary layer thickness from the upstream injected flow. Burd and Simon 57 reported that the inclined-slot combustor bleed cooling flow is capable of reducing secondary flow effect because the streamwise momentum from bleed flow thins the boundary layer and weakens the cross-stream flow. Zhang and Jaiswal 58 compared the endwall film cooling from upstream injection from double-row hole injection with



a single-row discrete slot injection. Their results indicated that uniform effectiveness distribution could be achieved using discrete slot injection for higher MFR, while higher effectiveness near the trailing edge can be obtained using injection from double-row of the staggered hole. Liu et al. 59 studied the upstream injection using either one or two rows of the hole. They found that while double row injection is always better than a single row regarding averaged effectiveness. Knost and Thole 60 studied the endwall film cooling combining both coolants from a flush slot and film cooling from two distinct hole patterns. They found that with slot and film cooling flows present; there was a large region in the center of the inlet to the passage that was overcooled. Zhang et al. 61 investigated the optimal hole diameter for upstream injection using two rows of the staggered cooling hole and found the optimized diameter/blowing ratio based on their particular design. Chowdhury et al. [62-64] presented complete information about film cooling effectiveness variation under different coolant-to-mainstream conditions on various endwall film-hole patterns with when upstream injection which is realized by two rows of the staggered cooling hole.

## **1.4 Conclusions**

For turbine internal cooling, the normal jet impingement is typically utilized in leading edge region, which implies the jet axis locates along the center axis of the concave surface. This paper firstly studies the jet position effects on the leading edge heat transfer by using the transient liquid crystal method 27. The tangential jet impingement is introduced by moving the axis of jet toward the edge of the test surface. The test surface is a semi-cylinder, which models the leading edge region. The full heat transfer distribution is obtained, which provide a baseline for the leading edge impingement heat transfer design (either normal jet or tangential jet). It can be used to optimize the impinging jet position according to the blade leading edge curvature and the

combustion hot gases direction. Secondly, this paper carefully studies the camera viewing angle effects on the experiments. Since the liquid crystal color is sensitive to the viewing angle from a curved test surface, the in-situ “Hue-Temperature” calibration profiles are essential to obtain the precise Nusselt number further. Thirdly to better understand the flow physics inside the impingement cavity, the CFD simulations were performed using RANS with two turbulence models, realizable  $k-\epsilon$  (RKE) and shears stress transport  $k-\omega$  model (SST). The RKE model is selected due to the better predictions. The comparisons between the experimental and numerical results are presented.

The three-row compound angle film cooling study 50 shows that two-row staggered with same angle and two-row in-line with opposite angle provide better effectiveness. Therefore, the present study firstly aims to investigate and optimize the two-row flat plate film cooling design based on previous three-row film cooling conclusions. Currently, the two-row cooling hole are designed as staggered row, same orientation angle with  $\beta_1 = +45^\circ$ ,  $\beta_2 = +45^\circ$  (design A) and inline row, opposite orientation angle with  $\beta_1 = +45^\circ$ ,  $\beta_2 = -45^\circ$  (design B). As correlations for two-row compound angle cooling hole are almost non-existent in the open literature. Hence, with all the experimental data, the two-row flat film cooling correlations will be proposed for design A and design B respectively, which are expected to be helpful to the turbine heat transfer and cooling designers.

The third of this study will focus on the film cooling performance on turbine vane endwall with considering the upstream injection and two endwall cooling hole design pattern under varying coolant condition. Previous findings have shown that upstream injection with high-momentum overcomes the endwall secondary flows and provides better protection on the passage. When the upstream injection is sufficient, it will strongly interact with the secondary flows and has the

potential to cover an even larger zone. However, cooling holes locating at the mid-chord region or downstream region on the platform are necessary because the extremely hot flow with accelerating speed creates higher heat load in this region. In this study, two-row of staggered cylindrical holes (37 holes for the 1<sup>st</sup> row, 38 holes for the 2<sup>nd</sup> holes, with  $d = 0.175$  cm) are implemented in front of the vane leading edge for upstream injection; then two-row of staggered compound angles holes (9 holes per row, with  $d = 0.15$  cm) are implemented on endwall surface: at mid-chord or downstream region. The main objectives of this paper are summarized below: 1. Investigate and compare the film cooling effectiveness for endwall film cooling at mid-chord and downstream region with the upstream injection. 2. Study the effects of coolant-to-mainstream mass flow ratio (MFR) and density ratio (DR) on the cooling effectiveness by varying the cooling condition. 3. By varying the MFR of upstream injection ( $MFR = 0-1.5\%$ ) and the MFR of endwall injection ( $MFR = 0-1.5\%$ ) from low to high, the coolant amount distribution between upstream and the endwall can be optimized to efficiently save the coolant.

## **2. TURBINE BLADE LEADING EDGE COOLING WITH ONE ROW OF NORMAL OR TANGENTIAL IMPINGING JETS\***

### **2.1 Experimental setup and method**

The Figure 2 shows a 3-D view of the experimental setup. This facility mainly consists of a large plenum with honeycomb inserted, a jet plate and a half-cylindrical test surface modeling the leading edge region. During the tests, the flow first entered the larger plenum, then impinged on the test surface and finally discharged from the exit slots. The test surface is made of clear Plexiglas, which is optically transparent and thermally resistive. A layer of liquid crystal film will be attached on the inner surface of the test surface to visualize the surface temperature distribution. The jet flow was supplied by an air compressor system with a standard orifice meter measuring the airflow rate. A regulator adjusts the mass flow rate. An inline heater was connected to heat the flow. The dimension of the thin-layer liquid crystal film (30 °C to 35 °C) is 15.24 cm (W) and 30.48 cm (L). This liquid crystal film is commercially available from Edmund Optics Website. A CCD camera is used to record the liquid crystal images, which allows a  $232 \times 568$  pixels' resolution. Two illuminating lights provides the lighting source.

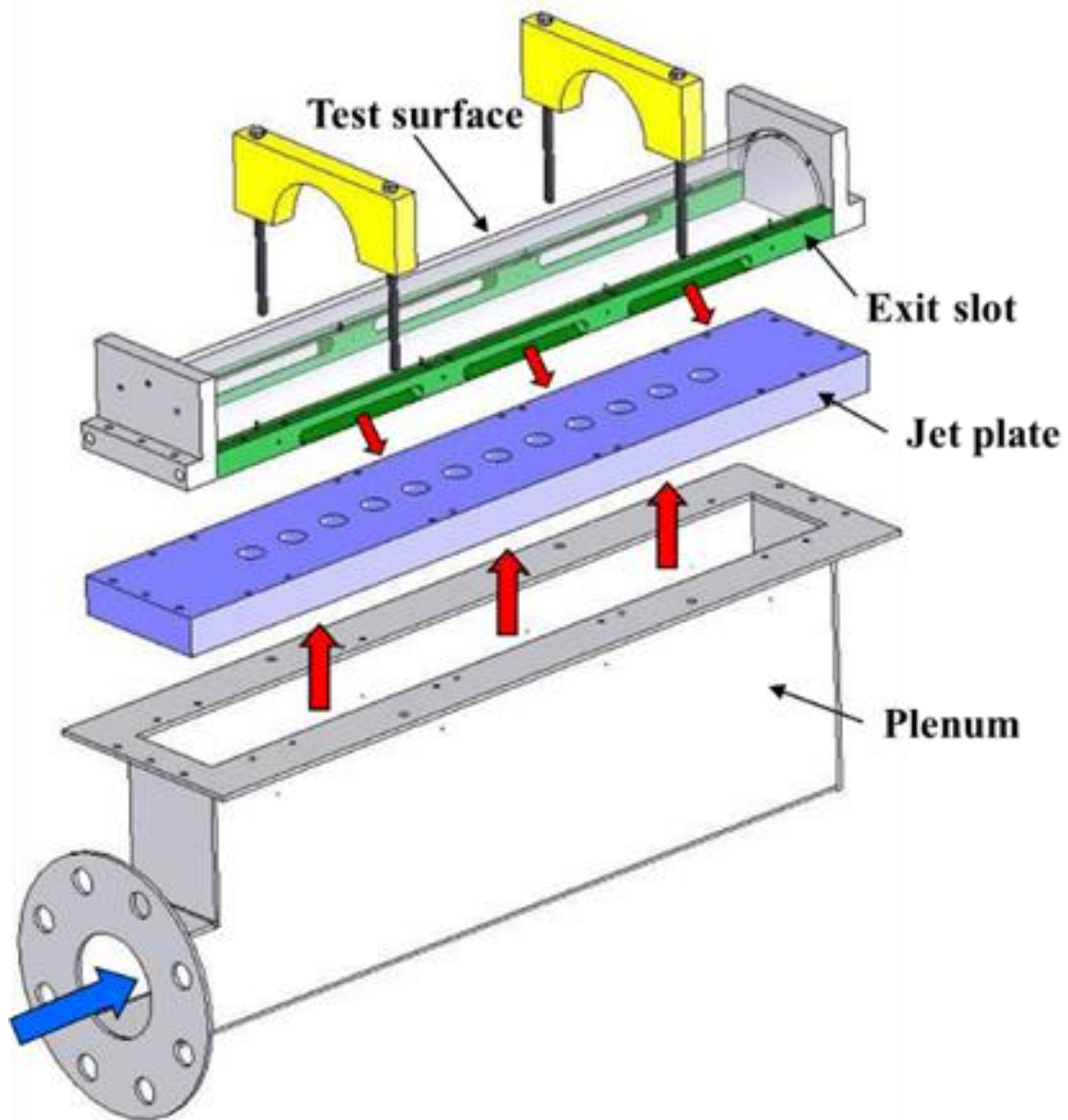


**Figure 2 Schematic diagram of the test facility**

Figure 3 shows the entire air loop. In the transient liquid crystal experiments, each test run is a thermal transient process initiated by a sudden introduction of hot air to the target surface. The procedure is firstly adjusting the mass flow rate to a particular jet Reynolds number. When the flow becomes steady, the air is routed to the bypass line and heated up to around 60 °C. A T-type thermocouple is used monitor this temperature inserted upstream of the three-way valve. Once the flow temperature is steady, the hot air flow is routed into the test section by switching the valve. Simultaneously, the CCD camera recording system and the temperature DAQ system starts to collect the curved surface RGB hue images and the inlet temperature variation of the jet flow. The camera is set to record the liquid crystal image every 0.5 seconds. About 2 minutes later, since most of the test surface area is a blue color, the test procedure is consider as finished.

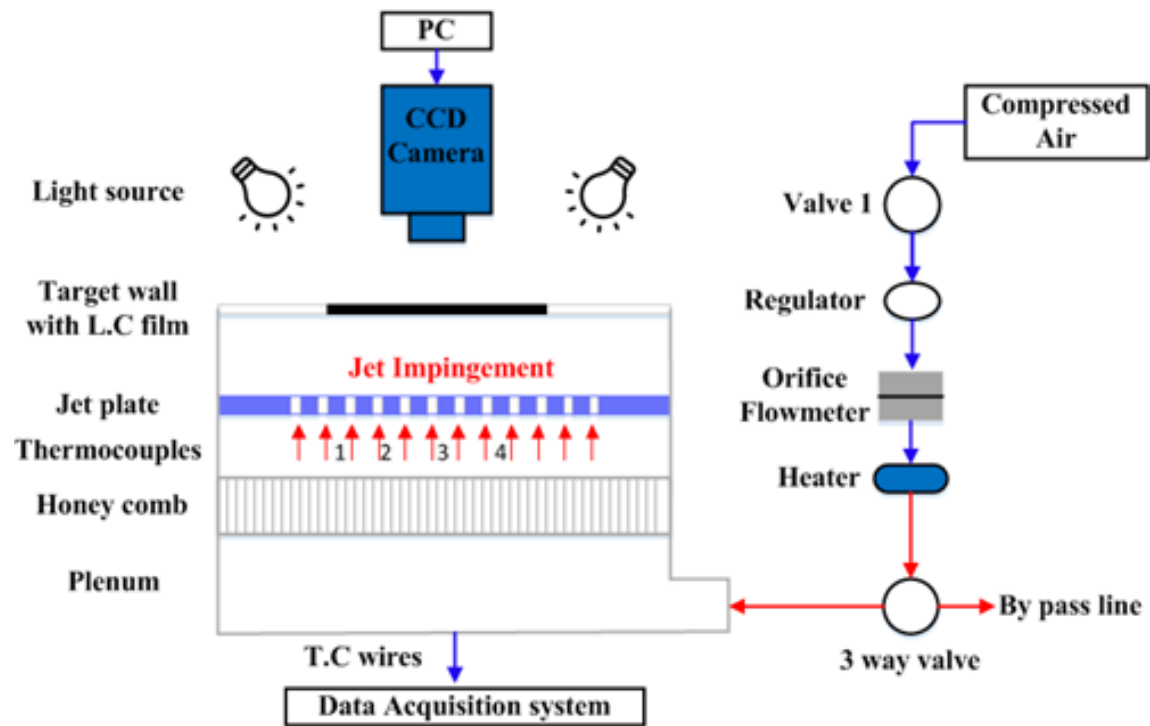
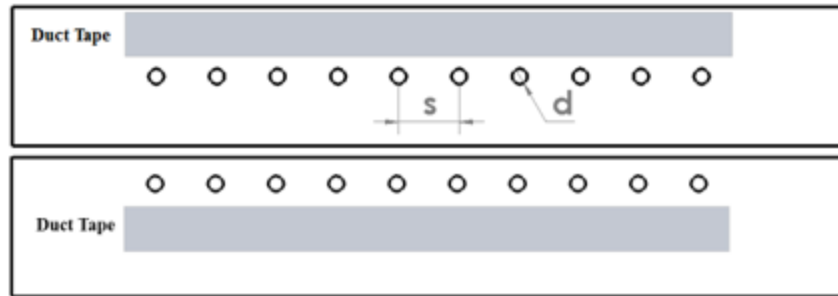


Figure 3 Schematic diagram of the air loop and test setup

In order to study the jet-hole position effect, a jet plate with two jet-hole locations is fabricated. Figure 4 gives the jet plate configurations. The jet plate is 83.83cm (33in) long, 13.79cm (5.5 in) wide with a thickness of 2.45cm (1in). The jet-hole diameter is  $d$  1.524cm (0.6in). The jet-to-jet spacing ( $s$ ) is  $4d$  and jet-to-target-plate distance ( $z$ ) is  $5d$ . Two jet-hole locations are manufactured on one jet plate. During the normal jet tests, the sideline jet holes are sealed with duct tape. During the tangential jet tests, the center-line jet holes are sealed. Figure 5 presents the jet flow direction for two jet impingent positions. The normal jets perpendicularly impinge on the test surface stagnation region through center-line jet holes and discharge from the exit slots on both sides. However, the tangential jets tangentially impinge on the test surface side wall through sideline jet holes and discharge from the exit slots oppose to the jet holes.





**Figure 4 Configuration of jet plate**

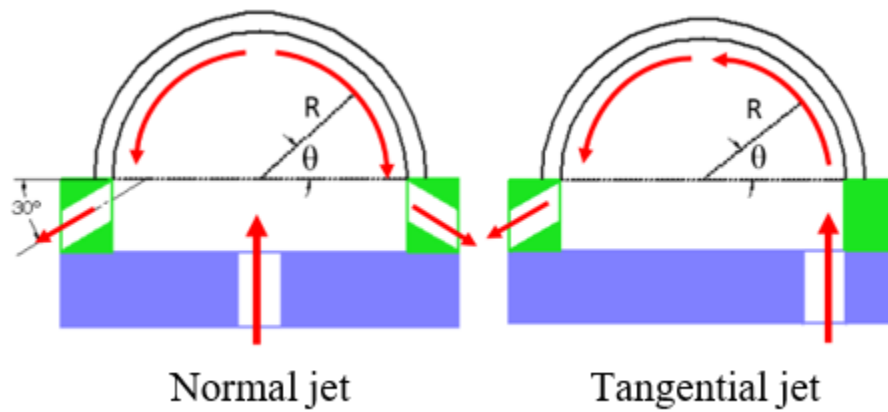


**Figure 5 Jet-hole position and flow direction**

### 2.1.1 Experimental measurement theory

The test surface is made of Plexiglas and its thickness is 0.635cm (0.25in). Therefore, the one-dimensional transient conduction into a semi-infinite body with convection boundary condition is applied. The surface temperature can be resolved by the following equations:

$$\frac{T_w - T_i}{T_m - T_i} = 1 - \exp\left(\frac{h^2 \alpha t}{k^2}\right) \operatorname{erfc}\left(\frac{h\sqrt{\alpha t}}{k}\right) \quad (2.1)$$

$$Nu = \frac{hd}{k} \quad (2.2)$$

$$T_w - T_i = \sum_{j=1}^N \left[ 1 - \exp\left(\frac{h^2 \alpha (t - \tau_j)}{k^2}\right) \times \operatorname{erfc}\left(\frac{h\sqrt{\alpha (t - \tau_j)}}{k}\right) \right] [\Delta T_{m_j}] \quad (2.3)$$

The heat transfer coefficient  $h$  at each pixel can be obtained from Eq. (2.1) by knowing the initial surface temperature ( $T_i$ ) measured by thermocouples, jet mainstream inlet temperature ( $T_m$ ) measured by four thermocouples, surface temperature ( $T_w$ ) measured by liquid crystal images w.r.t time and the test surface material properties. In the experiments, the bead size of the thermocouples is about 0.5mm. The response time of the thermocouples is about 0.374s. Figure 6 shows the mainstream temperature ( $T_m$ ) variation with time (t) during the TLC tests of Re=10k, 20k and 30k. The figure indicates the duration of the TLC tests, which ranges from 100s to 140s depending on the flow condition. However, to satisfy the 1D transient conduction assumption, only the images during t=40s to 50s are used to calculate the heat transfer coefficients. Since  $T_m$  depends on time, using the Duhamel's superposition theorem, the solution in Eq. (2.1) is represented as Eq. (2.3). Here  $\Delta T_m$  and  $\tau_j$  are the temperatures and time step changes obtained from Figure 6. By applying

Eq. (2.2), the Nusselt number at each pixel on the measured region (232X568 pixels) is determined.

The details of this method are documented by Ekkad and Han [28].

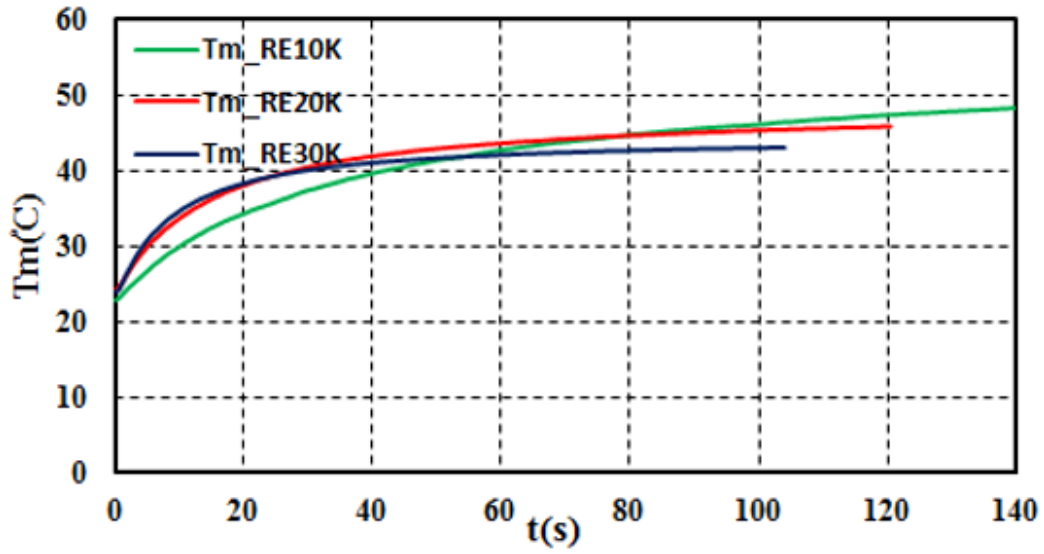


**Figure 6 Mainstream temperature variation with time**

### **2.1.2 Liquid Crystal Viewing Angle Calibration Setup and Procedure**

The calibration test section is schematically shown in Figure 7. The tests are conducted under  $90^\circ$  viewing angle and  $45^\circ$  viewing angle. A semi-cylindrical aluminum tube (OD = 10.16cm, L = 25.4cm) is fixed underneath the transparent surface. The aluminum tube outer surface is lined with the same kind of liquid crystal film. The aluminum tube inner surface is lined with a rubber heater with a dimension of 15.24cm (6in) width, 25.4cm (10in) length. The heater is used to provide uniform heat flux to the test section. Nine thermocouples are evenly embedded in the aluminum tube to measure the tube temperature. Because of the high thermal conductivity of the aluminum tube ( $k = 205\text{W/mK}$ ), the surface temperature measured by embedded thermocouples and by liquid crystal hue images are deemed identical.

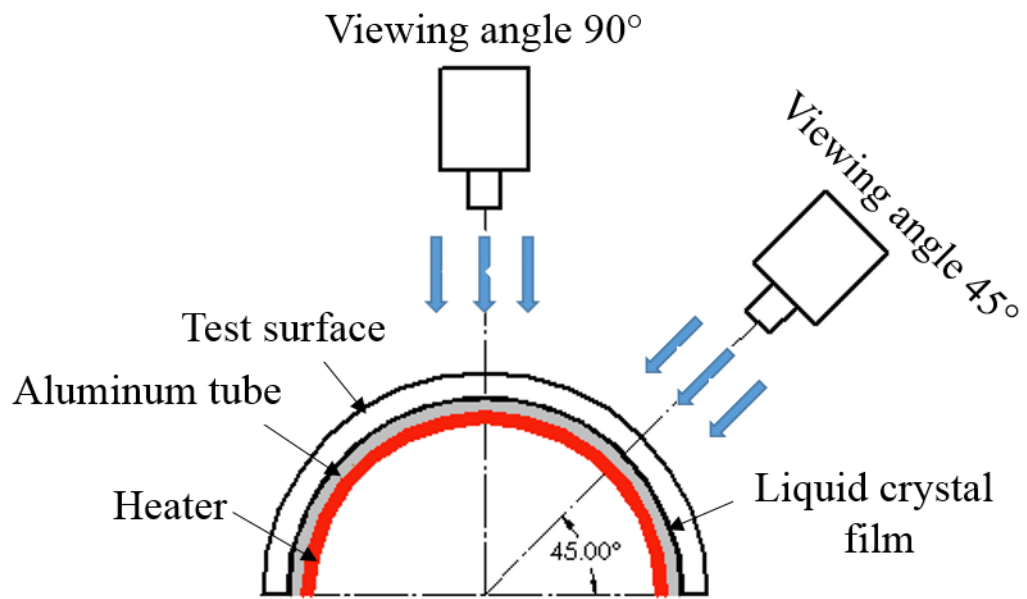
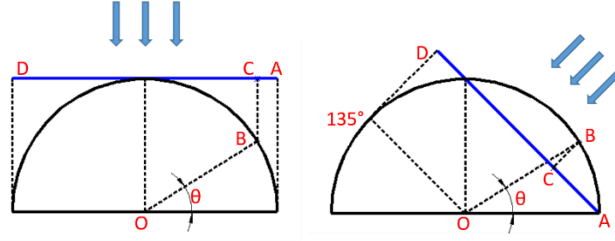


**Figure 7 Curved surface calibration test setup**

The calibration tests are thermal transient processes as well. They are performed under the same testing environment as liquid crystal tests but without the jet flow. During the tests, the DAQ system and the camera are switched on simultaneously. With the heater on, the surface temperature increases. The thermocouple data is recorded every 0.5 seconds, and the CCD camera is set to record LC images every 5 seconds. The average temperature of nine thermocouples varying from 30°C to 38°C is recorded and is correlated with the corresponding hue value. The temperature differences between the 9 thermocouples are within 0.3°C, which implies the temperature distribution on the test surface is very uniform.

For a curved test surface, the coordinate transformation step is needed to transfer the pixels on the flat image to the points. As the geometrical relationship shown in Figure 8, C is an arbitrary pixel on LC flat image viewed by a camera. B, the corresponding point on test curved surface, needs to be determined. The pixel length of AC can be known by measuring LC image. Through the geometrical relationship in Eq. (2.4) and Eq. (2.5),  $\theta$  is obtained and  $B(R \cos \theta, R \sin \theta)$  is determined as well. A viewing angle of 90° can capture a range from  $\approx 0^\circ$  to  $\approx 180^\circ$ , while a viewing angle of 45° can only capture a range from  $0^\circ$  to  $\approx 135^\circ$ .



B is expressed as  $B(R \cos \theta, R \sin \theta)$

$$AC = R - R \cos \theta, \text{ for } 90^\circ \text{ viewing angle} \quad (2.4)$$

$$AC = R \left( \frac{\sqrt{2}}{2} + \sin(\theta - 45^\circ) \right), \text{ for } 45^\circ \text{ viewing angle} \quad (2.5)$$

$R$ , the radius of test surface

**Figure 8 Coordinate transformation from image to surface**

Based on the temperature data provided by thermocouples, the hue value measured by liquid crystal film and coordinate transformation relations, the hue-temperature profiles at every  $\theta$  degree can be plotted. In present tests, due to the non-uniform hue distribution in the circumferential direction, the span-wise averaged hue value to the mean temperature value of thermocouples were correlated. The calibration curves at every  $\theta$  degree are plotted by MATLAB scripts. A group of 4th-order power fitting curves is used to fit the data points. Since the hue values have a subtle difference within  $5^\circ$ , the calibrations curves were generated at intervals of  $5^\circ$ . Finally, 36 and 27 calibration curves are obtained respectively for viewing angle at  $90^\circ$  and  $45^\circ$ .

It shows that the hue values ranges from 140 to 200 and the higher hue values indicate higher temperature. Figure 9 shows the data points and the fourth-order fitting curves for  $\theta=90^\circ$  with viewing angle  $90^\circ$  and Figure 10 shows the data points and the fourth-order fitting curve for  $\theta=45^\circ$  with viewing angle  $45^\circ$ . The fitting curves match the data points very well. The calibration profiles shown in Fig.8 evidently prove the hue variation in circumferential direction. It can be seen, at a certain temperature, the hue value at different  $\theta$  is different. Such non-uniform hue distribution on the curved surface shall affect the data analysis significantly and will be discussed in the following section.



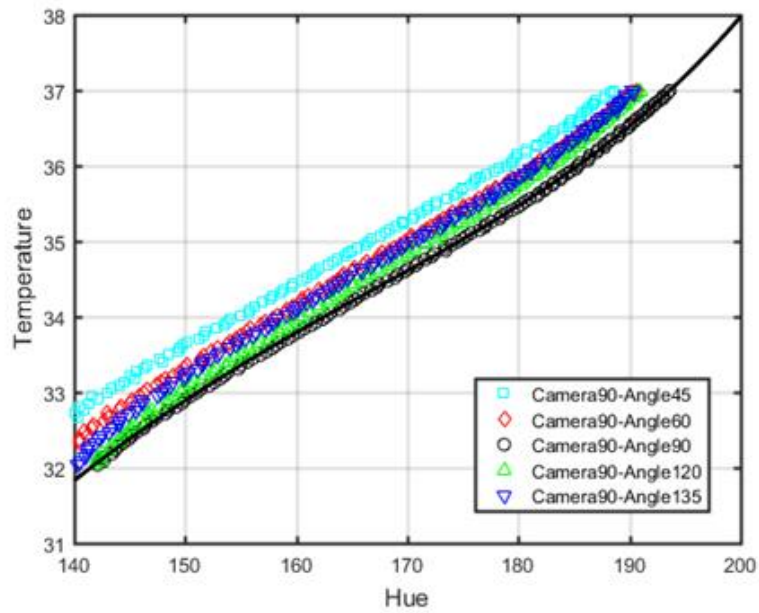


**Figure 9 Calibration curves for viewing angle 90°**

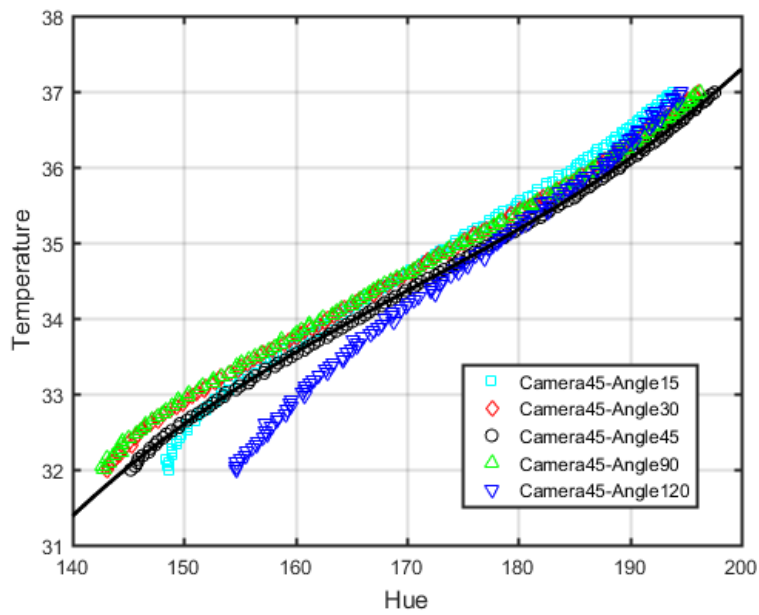


**Figure 10 Calibration curves for viewing angle 45°**

### 2.1.3 Calibration Curves Validity Test

The “Temperature-Hue” calibration profiles play an important role in determining Nusselt number results and should be validated. The case of normal jet impingement at  $Re=30,000$  is investigated. Figure 11 and Figure 12 compare the corrected and uncorrected Nusselt number profiles of viewing angle  $90^\circ$  and viewing angle  $45^\circ$ . The corrected Nusselt number profile is applied to the calibration curves obtained by the previously mentioned calibration tests. The uncorrected Nusselt number profile is only applied to the calibration curve at  $\theta = 90^\circ$  to calculate the  $T_w$ . Figure 11 shows that the uncorrected profile overlaps with the corrected profile near  $Y/d = 0$  (at viewing angle  $90^\circ$ ). The difference increases continuously as location far from the camera location (up to 15%). In Figure 12, the uncorrected and corrected profiles are coincident near location  $Y/d=2.5$  (at viewing angle  $45^\circ$ ). As far from the camera location, the uncorrected profile is gradually lower than corrected data. The maximum difference can reach up to 15%. This scenario can be explained by the calibration curves presented in Figure 9 and Figure 10. For a certain hue value at 170 in Figure 9, the calibration curve for  $90^\circ$  corresponds to  $34.5^\circ\text{C}$ , however, the calibration curve for  $45^\circ$  on test surface corresponds to  $35.2^\circ\text{C}$ , which is  $0.7^\circ\text{C}$  higher. Since the uncorrected data used the calibration curve belonging to  $90^\circ$  and calculate the temperature at  $45^\circ$ , it obviously causes an under-prediction of the temperature at  $45^\circ$  and ultimately under-predicted the Nusselt numbers. However, by applying the in-situ calibration curves, the effect of camera viewing angle, the effect of surface curvature and even the effect of non-uniform lighting source can be eliminated significantly. Figure 13 compares the corrected Nu results distribution with two viewing angles. It shows that the Nusselt number profiles obtained from viewing angle  $90^\circ$  and viewing angle  $45^\circ$  are almost coincident after proper corrections. It proves the curvature effect ( $\theta$ ) and the viewing angle effect ( $45^\circ$  or  $90^\circ$ ) to the Nusselt number profiles have been eliminated.

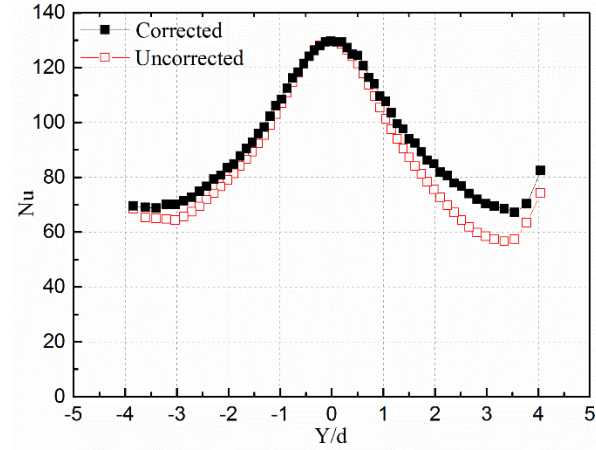


**Figure 11 Calibration curves effect at viewing angle 90°**

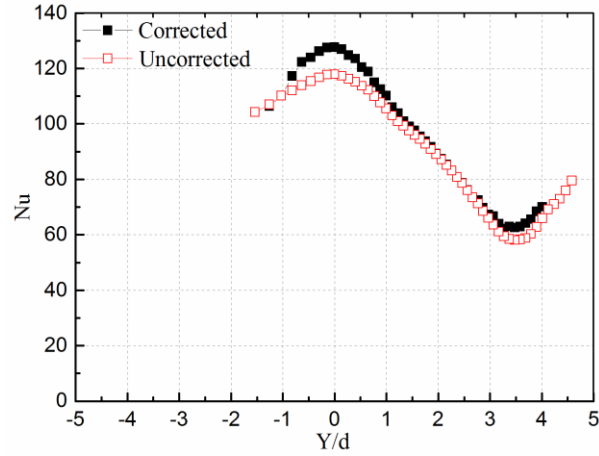


**Figure 12 Calibration curves effect at viewing angle 45°**

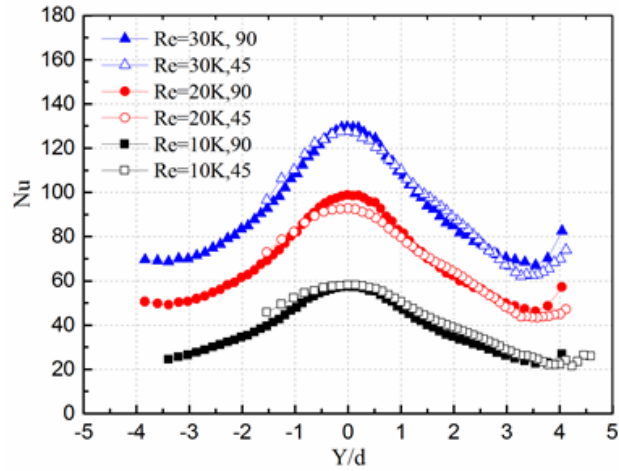


**Figure 13 Corrected results of two viewing angles**

Figure 14 shows the overall averaged Nusselt numbers with the variation of jet Reynolds numbers. It shows the present average Nusselt numbers have excellent agreement with data predicted by Chupp's correlation [5]. This further demonstrates the reliability of the calibration profiles in this TLC measurements.

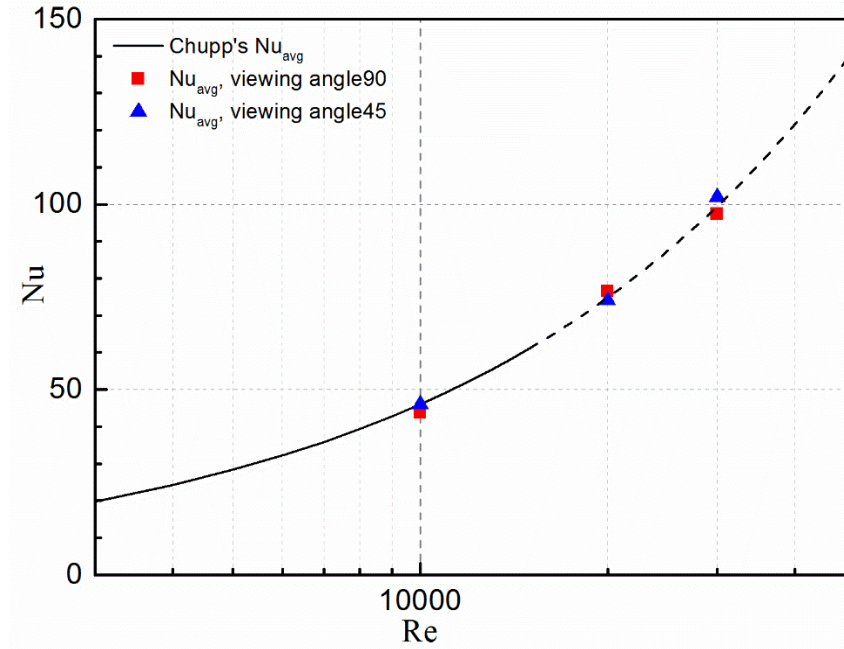


**Figure 14 Data comparison with published correlation**

#### 2.1.4 Experimental Uncertainty

The uncertainty of the jet Reynolds number is about 1.5%. The uncertainty of jet inlet temperature measured by thermocouples is about 2%. The uncertainty of experimental time reading is about 2%, the surface wall thermo-physical properties are about 3%. According to the method proposed by Kline and McClintock [65], the overall uncertainty in heat transfer coefficient calculations is estimated at 5%.

#### 2.2 Numerical setup and method

The commercial software FLUENT is used to simulate the heat transfer and flow field of jet impingement with the RANS models. As shown in Figure 15, the unstructured grids are generated using ICEM CFD. The coolant inlet is defined as mass flow rate boundary condition with 5% turbulence intensity. The coolant outlet is defined as the pressure outlet boundary condition. The periodic boundary condition is used on the cutting surfaces. The top test surface is a constant heat flux wall ( $q''=1070\text{w/m}^2$ ). Different heat flux value of  $1000\text{w/m}^2$ ,  $1070\text{w/m}^2$  and  $2070\text{w/m}^2$  have been applied on the top surface, however, the Nusselt number results are identical and not affected by the heat flux magnitude. The other surfaces are the adiabatic wall boundary condition. The mass flow rate at a particular Reynolds number is equal to the transient liquid crystal experiments. For this study, boundary layers on the curved surface wall, jet-hole plate, and plenum sidewall were created to promise the wall grid  $y^+$  is less than 1. The air properties vary with temperature. The numerical results are assumed converged with the residuals are lower than  $10\text{e-}4$ . Grid independence has been checked by comparing the results of three different grid size for each case. As show in Table 1, it is found that as the grid cell number grows, the relative difference of  $\text{Nu}_{\text{avg}}$  number decreases. To balance the numerical accuracy and the cost of

simulation time, 2.5 million mesh file is selected for the normal jet case and 3.5 million mesh file is selected for the tangential jet case, respectively.

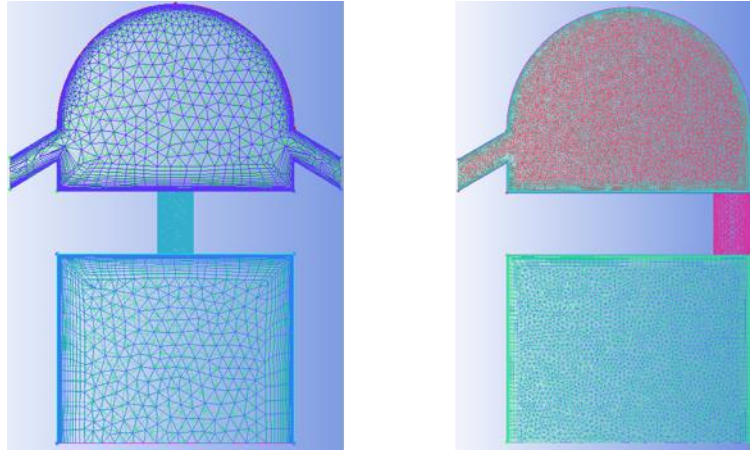


**Figure 15 Computational domain for two cases**

**Table 1 Grid independence study**

Normal Jet	Mesh 1 1.2 million	Mesh 2 2.5 million	Mesh 3 3.2 million
$Nu_{avg}$	78.65	80.55	80.16
Tangential Jet	Mesh 1 1.5 million	Mesh 2 3.5 million	Mesh 3 6.5 million
$Nu_{avg}$	85.97	87.04	87.09

The CFD calculations are carried out by the RANS turbulence models: SST and RKE. Figure 16 presents the comparison of the span-wised averaged Nusselt number profiles at  $Re=30,000$ . In this study, the numerical results predicted by the RKE model is closer to the TLC results than the SST model. Therefore, the RKE model is selected for the CFD calculations.

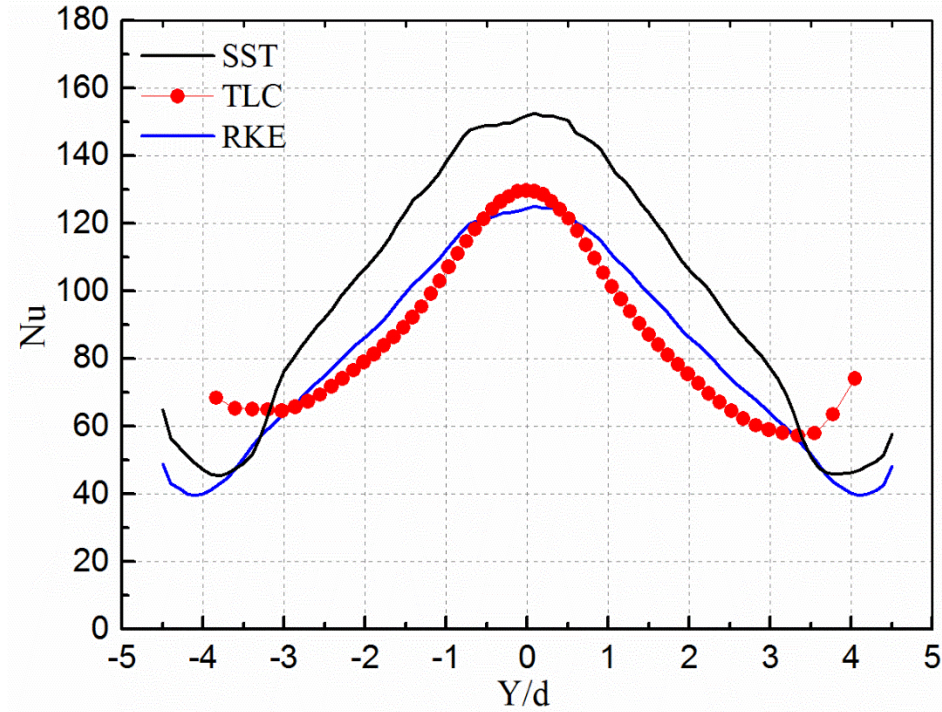


**Figure 16 Comparison of turbulence models at  $Re = 30k$**

### 2.3 Test Matrix

For leading edge jet impingement cooling test, the three jet Reynolds number ( $Re = 10,000, 20,000$  and  $30,000$ ) and two jet impinging positions (normal jets and tangential jets) will be studied. The jet Reynolds numbers were calculated based on the coolant mass flow rate ( $\dot{m}$ ) and jet hole diameter ( $d$ ). All 6 experimental cases ( $2 \text{ jet positions} \times 3 \text{ jet Reynolds number}$ ) and 6 corresponding numerical simulations are summarized in Table 2.

**Table 2 Test matrix for leading edge jet impingement study  
(Experimental & Numerical)**

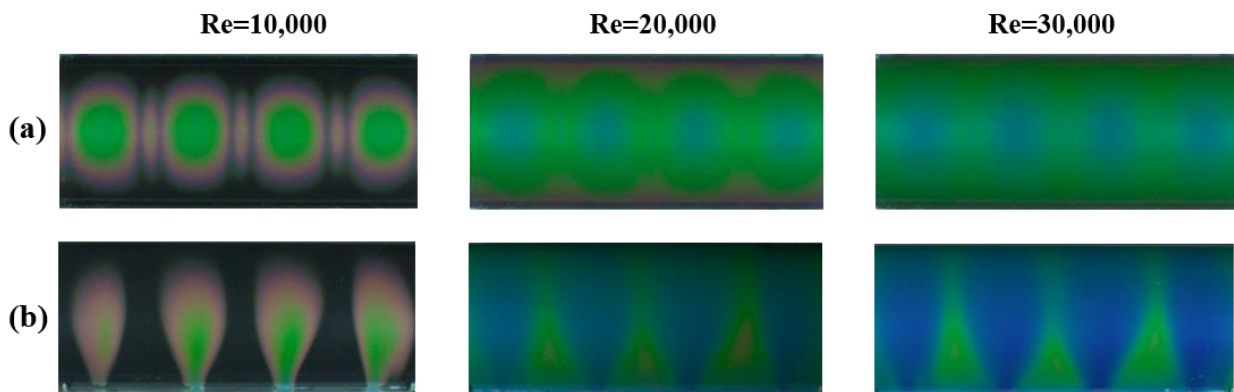
Normal jet	Tangential jet
$Re = 10,000$	$Re = 10,000$
$Re = 20,000$	$Re = 20,000$
$Re = 30,000$	$Re = 30,000$



## 2.4 Results and Discussion

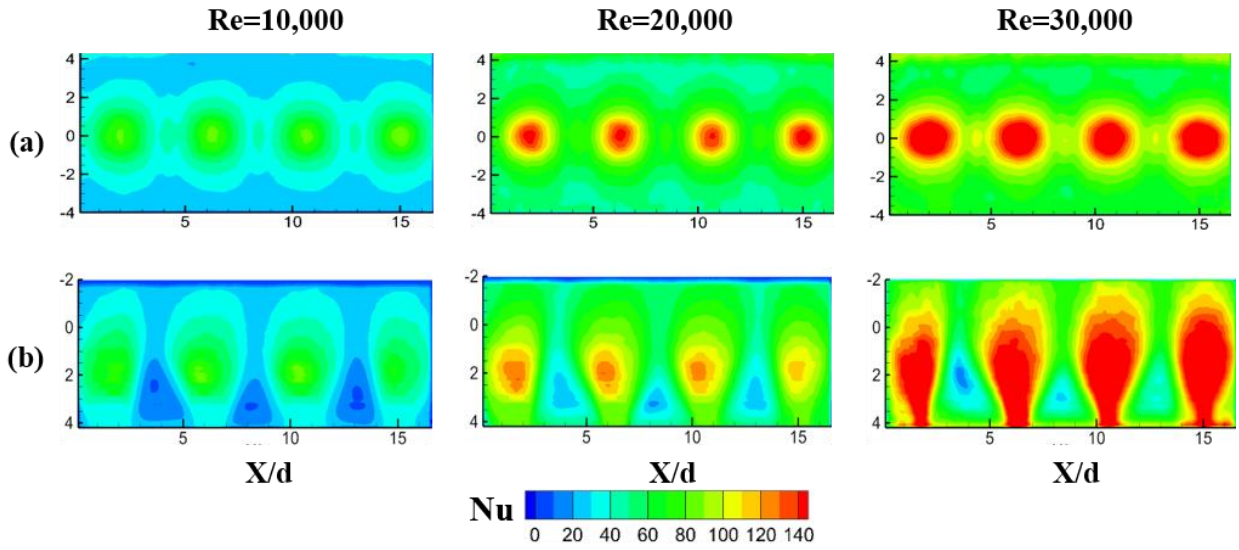
### 2.4.1 Experimental Detailed Local Heat Transfer Distribution

Figure 17 (a) and Figure 17 (b) present the surface images at  $t = 25\text{s}$  and  $45\text{s}$  taken by the CCD camera. The liquid crystal images of the normal jet impingement are recorded at viewing angle  $90^\circ$ ; the images for the tangential jet are recorded at viewing angle  $45^\circ$ . As the  $Re$  increases, the color of liquid crystal changes from red, green to blue. At the same time, the image is bluer (high Hue) when the jet Reynolds number is higher. The detailed local Nusselt numbers for all cases are presented in . Due to the limited length of liquid crystal film ( $L=25.4\text{cm}$ ), four jet holes are observed. Results are presented from  $X/d = 0$  to  $X/d = 16.7$  in the span-wise direction, where  $X$  is defined by the edge of liquid crystal film,  $d$  is the jet hole diameter ( $d=0.6\text{in}$ ). For the normal jet case, viewing angle  $90^\circ$ , the results are shown from  $Y/d = -4$  to  $Y/d = 4$  in the streamwise direction. For the tangential jet case, viewing angle  $45^\circ$ , the results are shown from  $Y/d = -2$  to  $Y/d = 4$ . In both figures,  $Y$  is the arc length defined from the curved surface center to the surface edge.



**Figure 17** Liquid crystal image (a) normal jet impingement at  $t=25\text{s}$ , viewing angle  $90^\circ$ ; (b) tangential jet impingement at  $t=45\text{s}$ , viewing angle  $45^\circ$ .

Figure 18 (a) shows the local Nusselt number distribution of the normal jet impingement. Overall, the increasing jet Re number indicates a higher heat transfer level due to the thinner boundary layer thickness. It is found that the Nusselt number contours are periodic with a circular region on the surface center. The higher heat transfer regions are just under the jet holes. Then the heat transfer level gradually decreases toward all directions due to the increase of boundary layer thickness. A slightly higher heat transfer region is found between the adjacent jets, which is due to the interaction of the adjacent jet flow. Figure 18 (b) shows the local Nusselt number distribution of the tangential jet impingement. The effect of jet Reynolds number is similar to the normal jet case. The higher jet Reynolds number indicates better heat transfer. However, the Nusselt number distribution is very different from the normal jet case. The heat transfer contour of the tangential jet impingement is periodic with a tear-drop heat transfer region. The higher heat transfer regions are near the jet entrance portion, then decreases gradually towards the jet exit. In addition, near the jet entrance, we notice the weak heat transfer zone between the adjacent jets.



**Figure 18 Detailed Nusselt number distribution (a) normal jet impingement; (b) tangential jet**

### 2.4.2 Numerical Detailed Heat Transfer Distribution

The numerically detailed heat transfer distributions of the two jet impinging positions are shown in Figure 19. Three jet Reynolds numbers ( $Re=10k$ ,  $20k$  and  $30k$ ) are calculated. The numerical heat transfer contours show excellent agreement with the experimental results. In Figure 19(a), the peak Nusselt number is at the stagnation region and gradually decreases toward the exits and forms a circular heat transfer contour. This heat transfer behavior agrees with the TLC findings. Additionally, the magnitudes of the local Nusselt numbers match well with those obtained from the TLC tests. In Figure 19 (b), the tear-drop contour shape predicted by the RKE model agrees with the TLC results. However, the predicted magnitudes of local Nusselt numbers are lower than that of the TLC tests, especially at the jet entrance region.

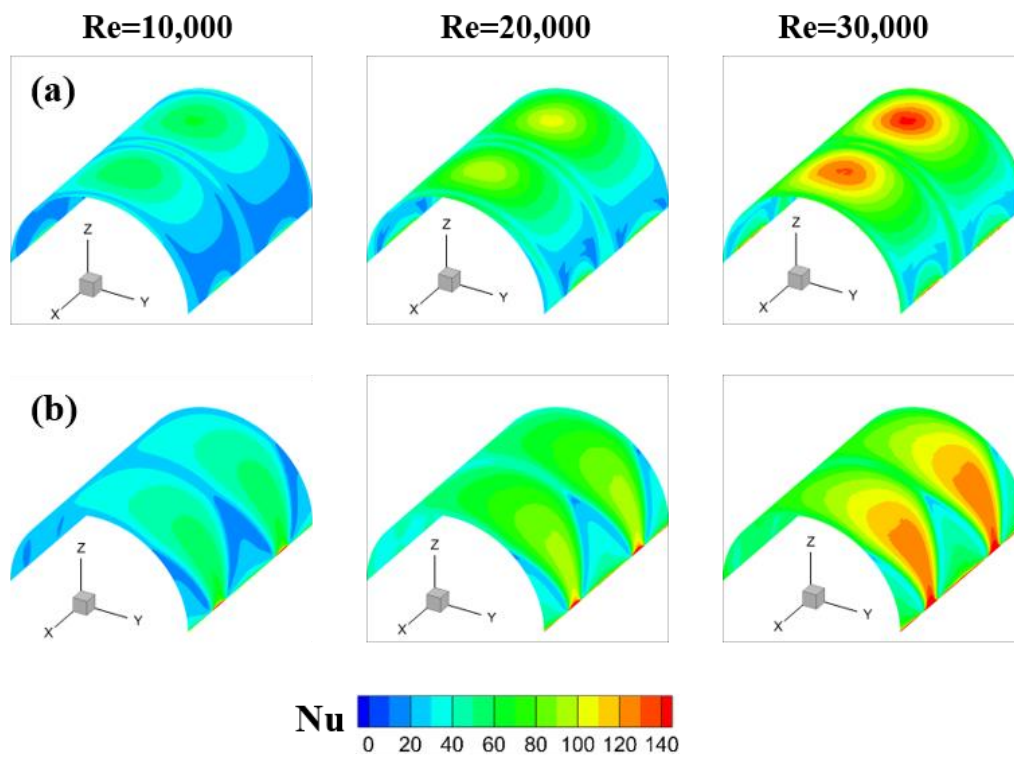


**Figure 19 Numerical Nu contour (a) normal jet; (b) tangential jet.**

Figure 20 shows the corresponding velocity field contours at YZ plane and cross the stagnation point of the two jet impinging positions. Obviously, the higher jet Reynolds number indicates higher velocity field. For the normal jet case in Figure 20 (a), the streamlines show that the jet directly impinges onto the test surface stagnation region, spreads in all directions and discharges from the exits. Due to the surface curvature, two symmetric vortexes are generated beside the stagnation region, which not only enhances heat transfer level near the wall but also strengthens the convection inside the impingement cavity.

The tangential jet impingement is obtained by moving the jet holes to the edge of the semi-cylinder. As shown in Figure 20 (b), the impinging jets are deflected along the curvature of the surface and discharged from the exit. The stagnation region disappears on the velocity contour. The velocity magnitude near the jet entrance region is higher than other regions, which explains the higher heat transfer in this region. In addition, a swirl flow is generated in the cavity center, which enhances the heat transfer on both the top test surface and the bottom surface.

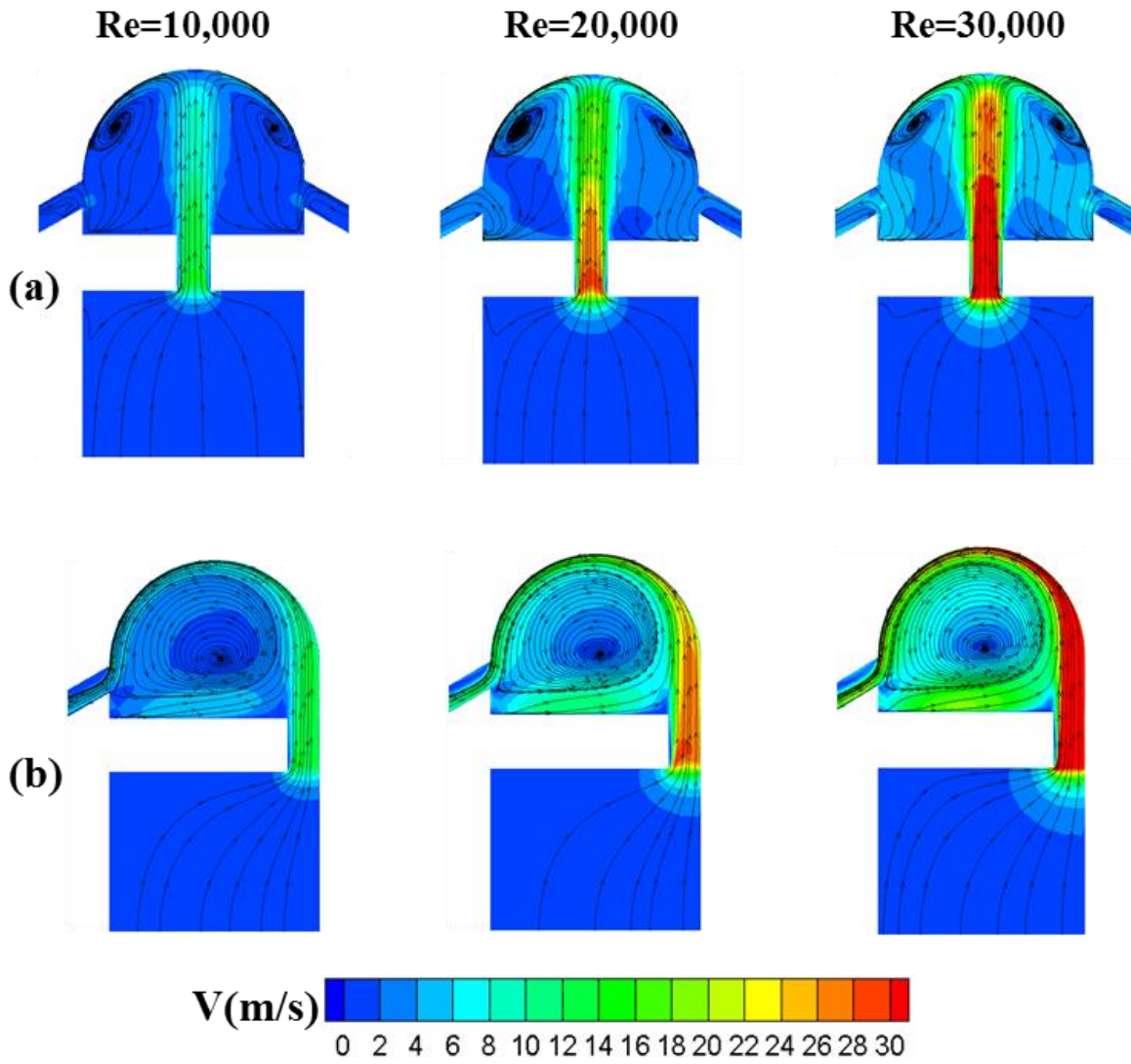
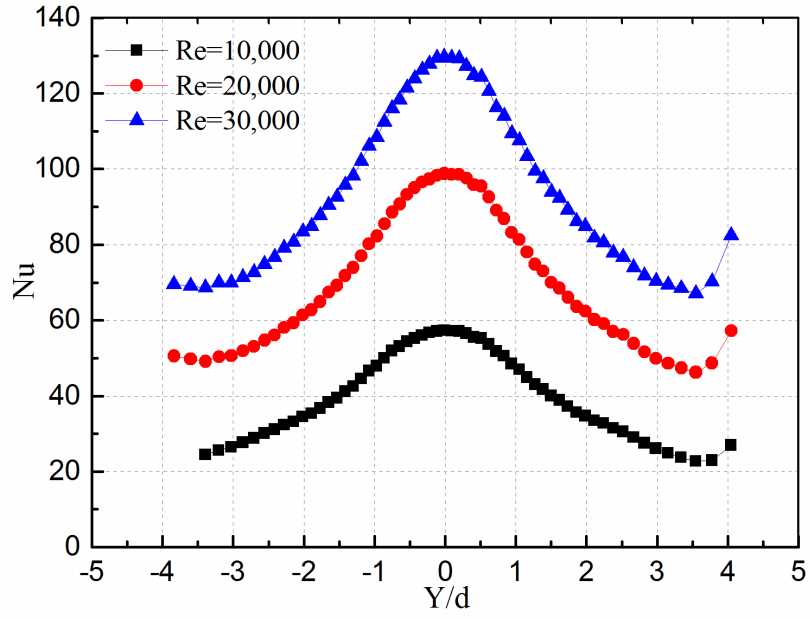


**Figure 20 Velocity contour on YZ plane (a) normal jet; (b) tangential jet.**

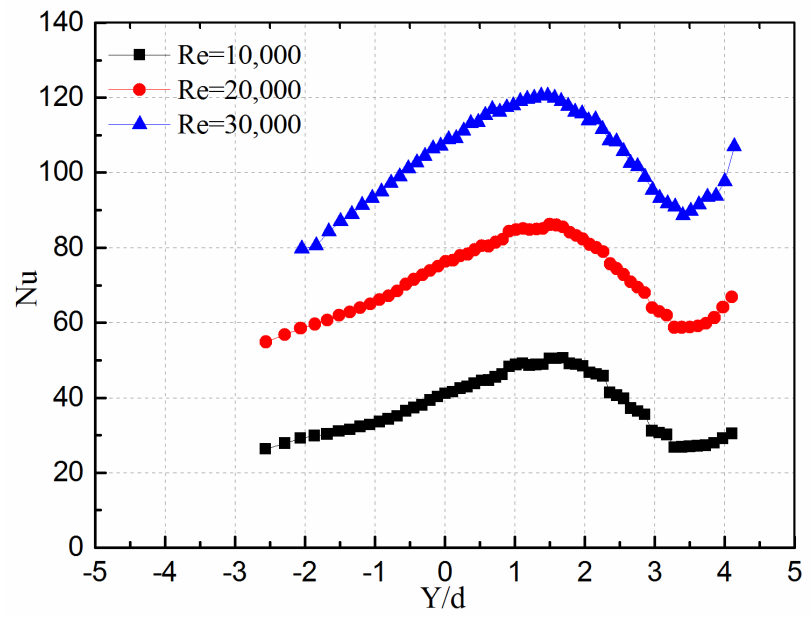
### 2.4.3 Span-wise Averaged Heat Transfer

Figure 21 (a) and Figure 21 (b) show the span-wise averaged Nusselt number of the TLC measurements of the two jet impinging positions and under three flow condition.  $Y/d$  is the non-dimensional location on the test surface.  $Y$  is the arc distance in the streamwise direction and defined from the curved surface center,  $d$  is the jet hole diameter. For the normal jet impingement, the peak Nusselt numbers are at  $Y/d = 0$ . The Nusselt numbers gradually decrease towards the exit due to the jet diffusion and the decreasing jet momentum. For the tangential jet impingement, the peak Nusselt numbers are at  $Y/d = 1.5$ , then decreases slowly toward the exit slots, which indicates the tangential jets provide more uniform heat transfer distribution.





(a) Normal jet

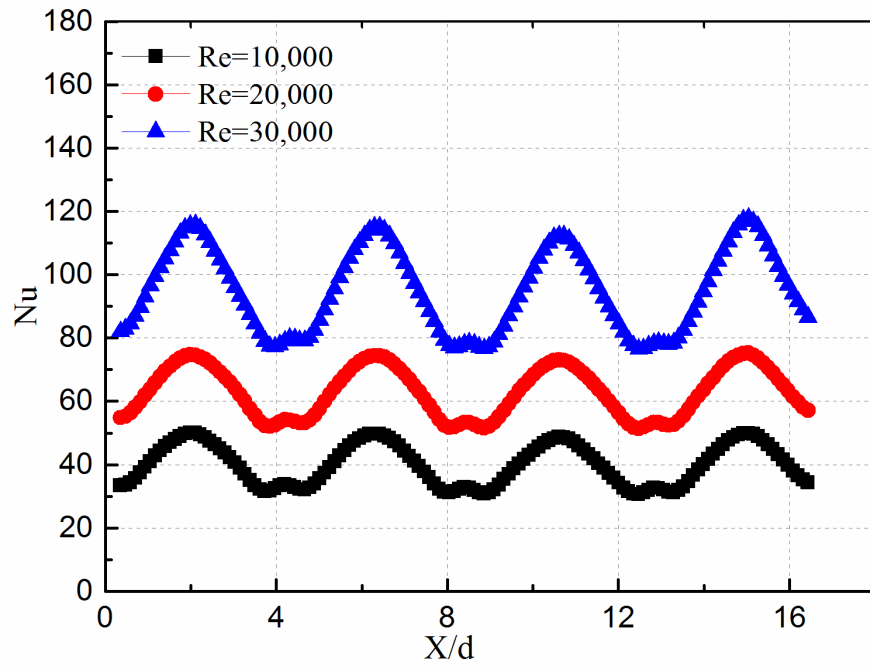


(b) Tangential jet

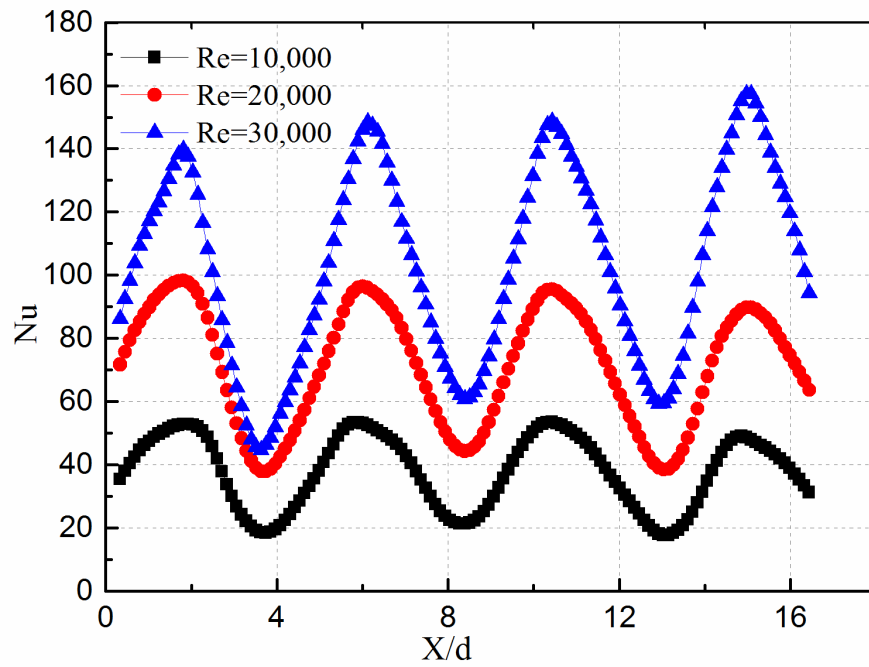
**Figure 21 Span-wise averaged Nusselt number**

#### 2.4.4 Stream-wise Averaged Heat Transfer

Figure 22 shows the stream-wise averaged Nusselt number profiles obtained by the TLC measurements for all cases.  $X$  is in the span-wise direction. For the two impinging positions, the Nusselt number profiles are very periodic. In Figure 22 (a), it shows that the increasing  $Re$  number leads to an improvement in the Nusselt number. The peak Nusselt number values are under the jet holes and abate symmetrically between jets. Between two jets, the tiny peaks of Nusselt number are noticed and they were clearly presented in Figure 22 (a) as well. These tiny peaks are due to the interaction of the adjacent jets. For normal jet impingement, the jets directly impinge onto the surface and the boundary layer develops in all directions. As the boundary layer thickness increasing in the span-wise direction, it was interrupted by the adjacent jets, which leads to higher  $Nu$ . In Figure 22 (b), in the tangential jet impingement, the peak Nusselt numbers are under the jet holes as well and drop more sharply between jets than the normal jet. Though increasing jet Reynolds number improves the surface heat transfer level, however, it creates more peak-to-valley heat transfer variation along the spanwise direction. It also finds that the peak Nusselt numbers of the tangential jet are higher than the peak values of normal jets. This can be explained by the velocity contour in Figure 20 (a) and Figure 20 (b). At the peak heat transfer region, the near wall velocity of the tangential jet is higher than the velocity of the normal jet under equal  $Re$  condition, so the boundary layer thickness is thinner, so the peak value of Nusselt number for the tangential jet is higher.



(a) Normal jet

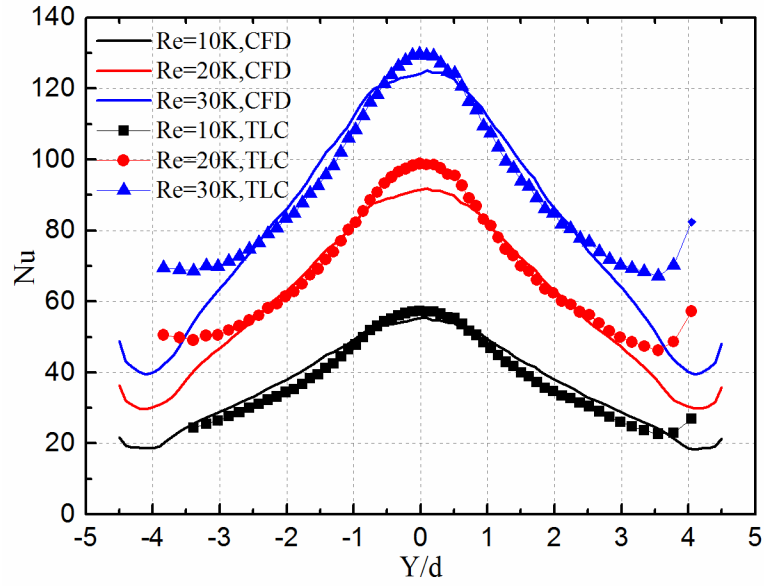


(b) Tangential jet

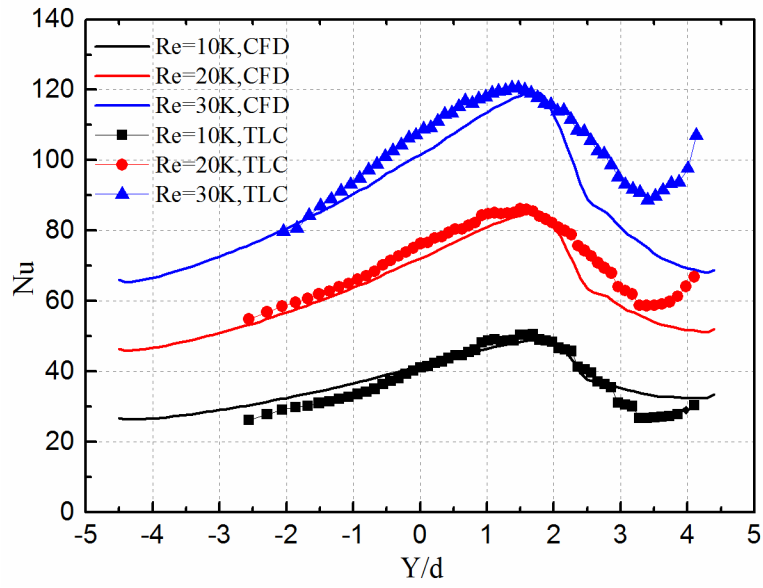
**Figure 22 Stream-wise averaged Nusset Number.**

#### 2.4.5 Numerical Analysis and Comparison with TLC Data

Figure 23 (a) shows the comparison of the spanwise averaged Nusselt number profiles of the normal jet impingement, which is obtained by the TLC tests and the RKE model. It shows that from  $Y/d = -3.0$  to  $Y/d = 3.0$ , the RKE model provides a fairly good prediction of the heat transfer distribution. The peak Nusselt numbers are at  $Y/d=0$ , the CFD results under predict the peak Nusselt numbers by 3.2% at  $Re=10k$ , 6.9% at  $Re=20k$  and 3.6% at  $Re=30k$  respectively. However, the numerical simulation under-predicts the jet exit region  $Y/d < -3.0$  and  $Y/d > 3.0$ . Figure 23 (b) shows the case of tangential jet. It shows the predicted results are fairly close to the TLC results from  $Y/d < 2$ . But near the jet entrance region ( $Y/d > 2$ ), the RKE model under predicts the heat transfer level up to 20%, which is probably due to the underprediction of the RKE model in the lateral mixing.



(a) Normal jet



(b) Tangential jet

**Figure 23 CFD and TLC comparison**

## 2.4.6 Area-Averaged Nusselt Numbers

Figure 24 presents the area averaged Nusselt numbers comparison for all cases ( $0^\circ < \theta < 135^\circ$ ). The figure firstly indicates the averaged Nu increases with the increasing Re. The averaged Nusselt numbers of the normal jet and the tangential jet is very close though very different heat transfer distributions are found. Lastly, the RKE model under predicts the averaged Nusselt numbers on the test surface by 1% to 10% depending on the jet Reynolds number.

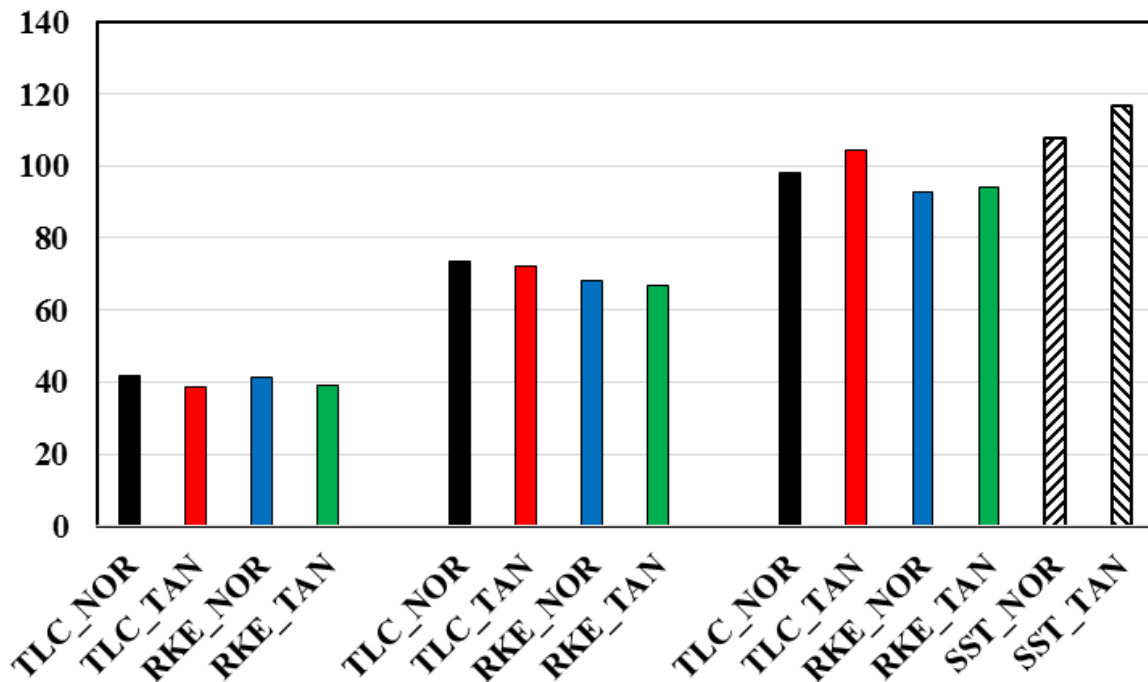


Figure 24 Averaged Nusselt numbers ( $0^\circ < \theta < 135^\circ$ ).

## 2.5 Conclusions

The present study firstly investigates the effect of jet impinging position on the leading edge heat transfer. One row of normal jets and one row of the tangential jets impinge on a semi-cylindrical surface under three flow conditions. The TLC technique is used to measure the surface heat transfer coefficients. Secondly, an in-situ calibration test is performed on the semi-cylindrical surface in order to eliminate the effect of surface curvature and the effect of camera viewing angle. Lastly, the CFD simulations are performed to understand the jet flow behavior and select a better turbulence model. The conclusions are as follows:

To eliminate the error arising from viewing angle for TLC experiments, the in-situ calibration was performed on the semi-cylindrical test surface. The calibration curves corresponding to different viewing angles were obtained and used in data reduction. Without viewing angle correction, an error up to 15% under-prediction can be seen in the derived Nusselt numbers.

The local Nusselt numbers increase with increasing jet Reynolds number.

The heat transfer distribution on test surface is significantly affected by the jet position. From the TLC results, the normal jet impingement produces circular heat transfer contour, however, the tangential jet produces the tear-drop contours. The tangential jet provides more uniform heat transfer distribution than the normal jet, but the area averaged Nusselt numbers are similar.

The RKE turbulence model shows good capability in predicting the heat transfer of normal jet impingement. For the tangential jet impingement, the RKE model predicts the heat transfer trend well but it under-predicts the heat transfer level up to 20% at the entrance portion.

### **3. FILM COOLING EFFECTIVENESS FROM TWO-ROW OF COMPOUND ANGLED CYLINDRICAL HOLES USING PSP TECHNIQUE\***

#### **3.1 Experimental setup and method**

Figure 25 and Figure 26 schematically show the experiment setup and coolant feed geometry. The unit of the dimensions in Figure 26 is inch. The injection plate is placed in a low-speed suction-type wind tunnel, which is used to generate steady mainstream flow. The Reynolds number of mainstream flow is 285,000 based on the hydraulic diameter of the channel inlet. The inlet velocity measured by pitot-static tube is around 21.8 m/s. A turbulence grid is installed to generate a controlled turbulence intensity as the inlet condition; it provides flow with turbulence intensity around 6%. The coolant supplied from gas cylinders is ducted to the plenum chamber and finally discharged through the two-row film cooling holes. The rotameters are connected in the test loop to control the coolant flow rate. LED light and CCD camera are equipped for the PSP measurement procedure. The test plates are sprayed with PSP and located at 20 cm downstream of the turbulence grid. It is well embedded in the wind tunnel.



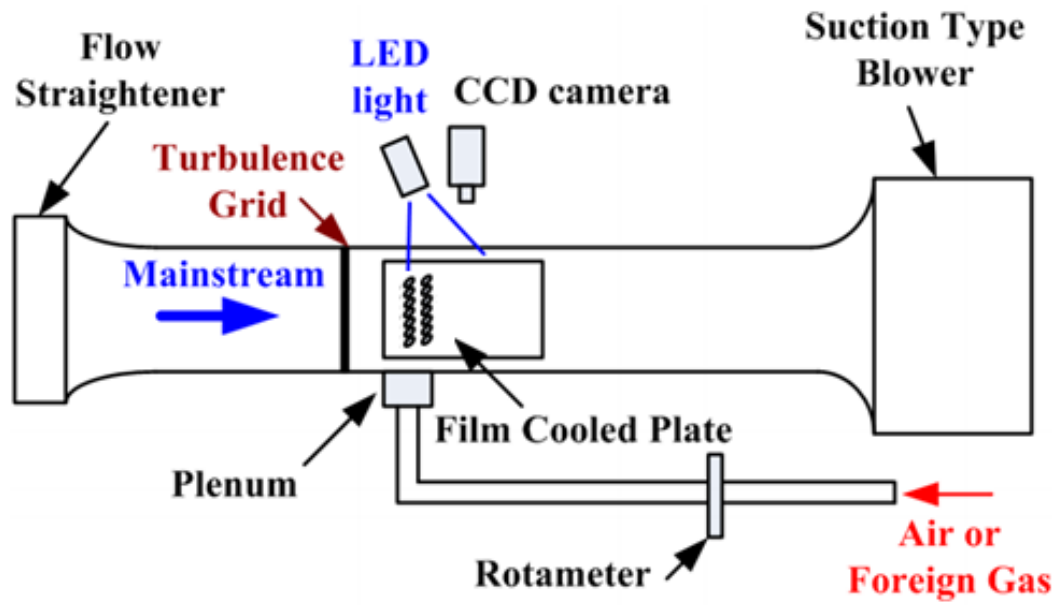


Figure 25 Schematic diagram of test loop

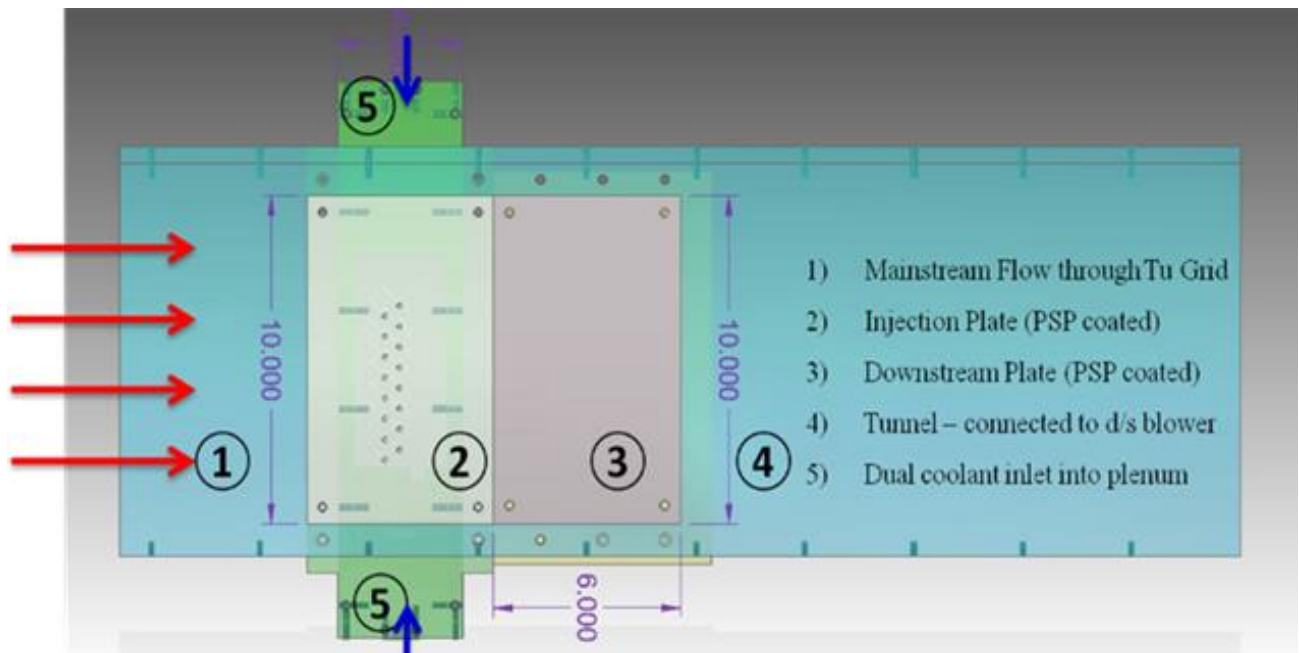
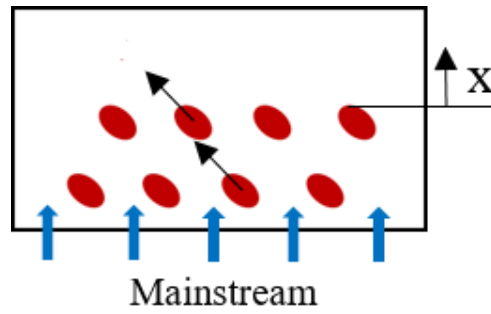
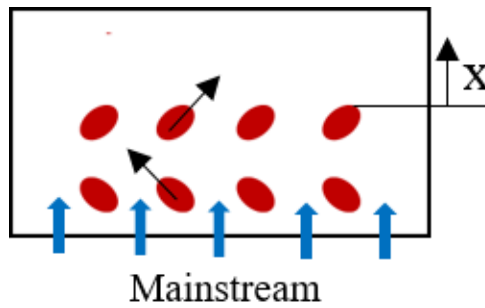


Figure 26 Coolant feed geometry

Figure 27 shows the two-row cooling hole designs for  $p/d = 4$ . As can be seen, in design A the two-row compound cylindrical holes are staggered with the same orientation angle:  $\beta_1 = +45^\circ$ ,  $\beta_2 = +45^\circ$ . The holes, in design B, are in-line row with opposite orientation angle  $\beta_1 = +45^\circ$ ,  $\beta_2 = -45^\circ$ . For all geometries, the cylindrical hole diameter ( $d$ ) is fixed at 4mm, the inclination angle is  $30^\circ$ , and the space between rows is  $3d$ . There are eight holes for  $p/d = 4$  and six holes for  $p/d=6$  per row. Nitrogen and  $\text{CO}_2$  are used as the coolant to obtain the density ratio of 1.0 and 1.5. To simulate engine-like condition ( $\text{DR}=1.7\sim 2.0$ ), mixture gas with 15%  $\text{SF}_6$  and 85% Ar are used to obtain the density ratio of 2.0.



(a) Design A,  $p/d = 4$ , staggered,  $\beta_1 = +45^\circ$ ,  $\beta_2 = +45^\circ$



(b) Design B,  $p/d = 4$ , inline,  $\beta_1 = +45^\circ$ ,  $\beta_2 = -45^\circ$

**Figure 27 Two-row designs for  $p/d = 4$**

### 3.1.1 Experimental measurement theory

The adiabatic film cooling effectiveness is expressed by:

$$\eta = \frac{T_{aw} - T_m}{T_c - T_m} \quad (3.1)$$

where  $T_{aw}$  is the adiabatic wall temperature,  $T_m$  is the mainstream temperature and  $T_c$  is the coolant temperature. If  $\eta = 1$ , then  $T_{aw} = T_c$ , so the surface is perfectly covered by the coolant. By applying the heat and mass transfer analogy when turbulent Lewis number equals to 1, the film cooling effectiveness can be approximately determined by the concentration of the corresponding temperature parameters:

$$\eta = \frac{T_{aw} - T_m}{T_c - T_m} \approx \frac{C_{c,w} - C_m}{C_c - C_m} \quad (3.2)$$

In Eq. (3.2),  $C_c$  and  $C_m$  are the concentration of coolant and the concentration of the mainstream (air) respectively, which are fixed parameters determined by the given coolant/mainstream conditions.  $C_{c,w}$  is the coolant concentration on the wall, which is mixed with the mainstream, gradually been diluted. The higher  $C_{c,w}$  value indicates the more coolant attached on the wall, obviously the cooling performance is better.

The fundamental principle of PSP measurement is based on the fact that the concentration of oxygen in the mainstream (air) is fixed and the concentration of oxygen in the foreign cooling gas equals to zero. When the foreign gas served as the coolant (zero oxygen) and ejected onto the surface, the foreign gas (zero oxygen) is mixed with the mainstream air (fixed oxygen

concentration), the surface oxygen concentration distribution is changed. Then, the film cooling effectiveness can be related to the oxygen concentration distribution on the wall. The lower oxygen concentration indicates more foreign gas attached on the wall, which means higher film cooling performance. As the oxygen concentration can be related to the oxygen partial pressure, we have Eq. (3.3).

$$\begin{aligned}
 \eta &\approx \frac{C_{c,w} - C_m}{C_c - C_m} = \frac{C_{fg,w} - C_{air}}{C_{fg} - C_{air}} \\
 &= \frac{C_{O2,fg,w} - C_{O2,air}}{C_{O2,fg} - C_{O2,air}} \\
 &= 1 - \frac{C_{O2,fg,w}}{C_{O2,air}} \\
 &= 1 - \frac{P_{O2,fg,w}}{P_{O2,air}} \\
 &= 1 - \frac{P_{O2,fg,w}/P_{O2,ref}}{P_{O2,air}/P_{O2,ref}}
 \end{aligned} \tag{3.3}$$

When the density of foreign cooling gas is different from 1.0, the film cooling effectiveness is calculated by Eq. (3.4), where  $W_{fg}$  and  $W_{air}$  are the molecular weights of the foreign gas and air.

$$\eta = 1 - \frac{1}{\left( \frac{P_{O2,air}/P_{O2,ref}}{P_{O2,fg,w}/P_{O2,ref}} - 1 \right) \frac{W_{fg}}{W_{air}} + 1} \tag{3.4}$$

Pressure-sensitive paint (PSP) is a photo-luminescent material and responsive to the partial pressure of oxygen. It emits light under the excitation of LED light, and the intensity of the emitted light is inversely proportional to the partial pressure of oxygen. Figure 28 shows the typical PSP calibration curves at different temperatures, which was obtained by the PSP calibration tests.  $P_{ref}$

is the ambient pressure, and  $I_{ref}$  is light intensity measured at  $P_{ref}$ . The intensity measured at lower pressures is denoted as  $I$ . To clear the background noise, the intensity under the black environment is obtained, and it will be subtracted from  $I$  and  $I_{ref}$ . As shown in Figure 28, as the partial pressure of oxygen increases, the light intensity emitted by PSP painted surface gradually decreases. It should note that PSP is sensitive to the surface temperature, so ensuring that the reference temperature is identical to the tested temperature allows the curves to overlap together as shown in Figure 28. A robust calibration is indispensable for a high accuracy PSP film cooling measurement. During the measurement process, the PSP painted surface is excited by a light in the blue region of the spectrum (around 400nm, usually through a LED array), then the paint emits a light in the red region (>600nm). A CCD camera with a long pass filter is used to record the emission intensity. So the calibration profile can be obtained.

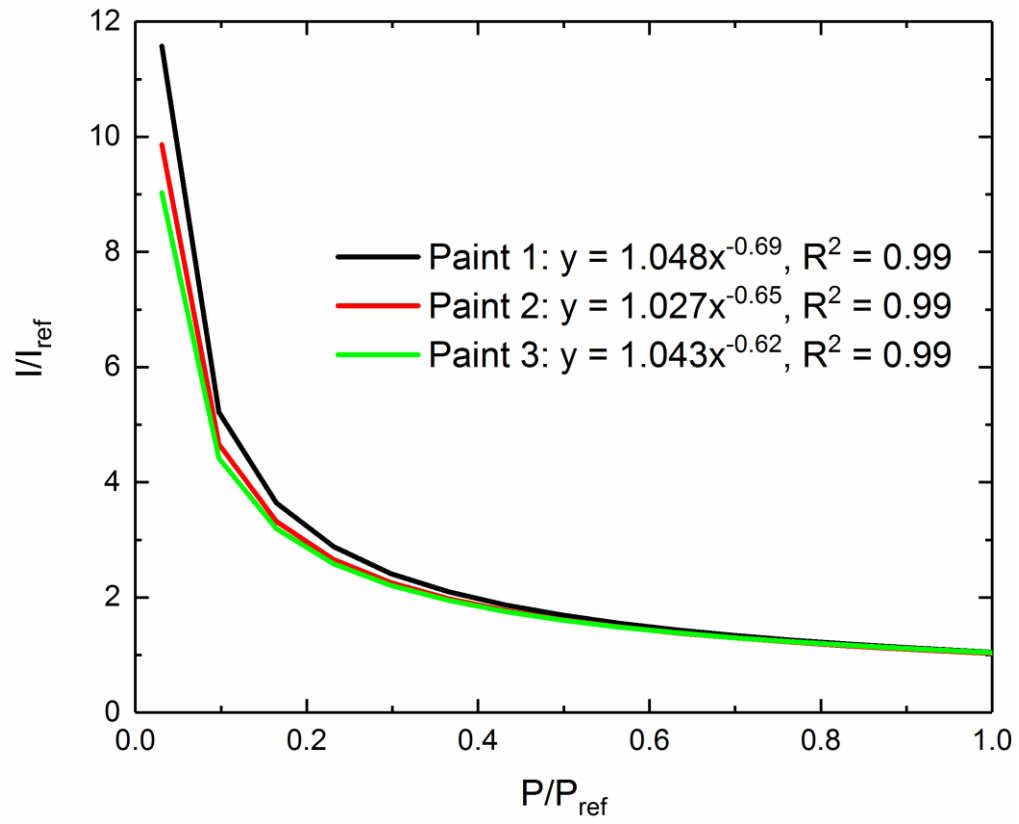


**Figure 28 PSP calibration curves**

### 3.1.2 Experimental Uncertainty

The uncertainty for the derived film cooling effectiveness values mainly comes from the PSP emission intensity value captured by the camera. There is a maximum of 1% error in the mainstream velocity and a maximum 6% error of the coolant flow rates which is expected at the lowest coolant flow rate. Therefore, based on the method of Kline-McClintock [65] at a 95% confidence level, the uncertainty is estimated to be around 9% at  $\eta = 0.3$  and 5% at  $\eta = 0.5$ .

### 3.2 Test Matrix

The film cooling blowing ratio effects of the two-row cooling hole were studied at four different blowing ratios  $M = 0.5, 1, 1.5$  and  $2.0$ . The effects of coolant-to-mainstream density ratio (DR) were tested at  $DR = 1, 1.5$ , and  $2$ . Nitrogen and  $CO_2$  are used as the coolant to obtain the density ratio of  $1.0$  and  $1.5$ . To simulate engine-like condition ( $DR=1.7\sim2.0$ ), mixture gas with 15%  $SF_6$  and 85% Ar are used to obtain the density ratio of  $2.0$ . The two designs with three  $p/d$  ratios for design A and design B are represented by A1 ( $p/d = 4$ ), A2 ( $p/d = 6$ ), A3 ( $p/d = 8$ ) and B1 ( $p/d = 4$ ), B2 ( $p/d = 6$ ), B3 ( $p/d = 8$ ). All 72 test cases are summarized in Table 3.

Table 3 Test matrix for two-row film cooling study

	Geometry ( $d = 4\text{mm}$ , $s/d=3$ )				Geometry and Coolant flow parameters		
	$\alpha$	$\beta_1$	$\beta_2$	Arrangement	$p/d$	M	DR
<b>A</b>	$30^\circ$	$+45^\circ$	$+45^\circ$	In-line	4,6,8	0.5, 1.0, 1.5, 2.0	1.0, 1.5, 2.0
<b>B</b>	$30^\circ$	$+45^\circ$	$-45^\circ$	Staggered	4,6,8	0.5, 1.0, 1.5, 2.0	1.0, 1.5, 2.0



### 3.3 Experimental Results and Discussion

In this section, we present film cooling effectiveness concerning local distribution contours, span-wise laterally averaged curves and area-averaged plots. Typical cases are selected to discuss the combined effects of geometry, blowing ratio, density ratio, and  $p/d$  ratio. It is noteworthy that there is a joint between injection plate and downstream plate, covered with scotch tape, is used to maintain flow uniformity. Hence, the data at this location is not available and appears as a discontinuity gap in contours and plots. To avoid edge effect, data of the middle three pitches are taken to show in contours and laterally averaged film cooling effectiveness curves. In all line plots,  $x/d = 0$  denotes the downstream edge of the second-row hole. The two designs with three  $p/d$  ratios for design A and design B are represented by A1 ( $p/d = 4$ ), A2 ( $p/d = 6$ ), A3 ( $p/d = 8$ ) and B1 ( $p/d = 4$ ), B2 ( $p/d = 6$ ), B3 ( $p/d = 8$ ).

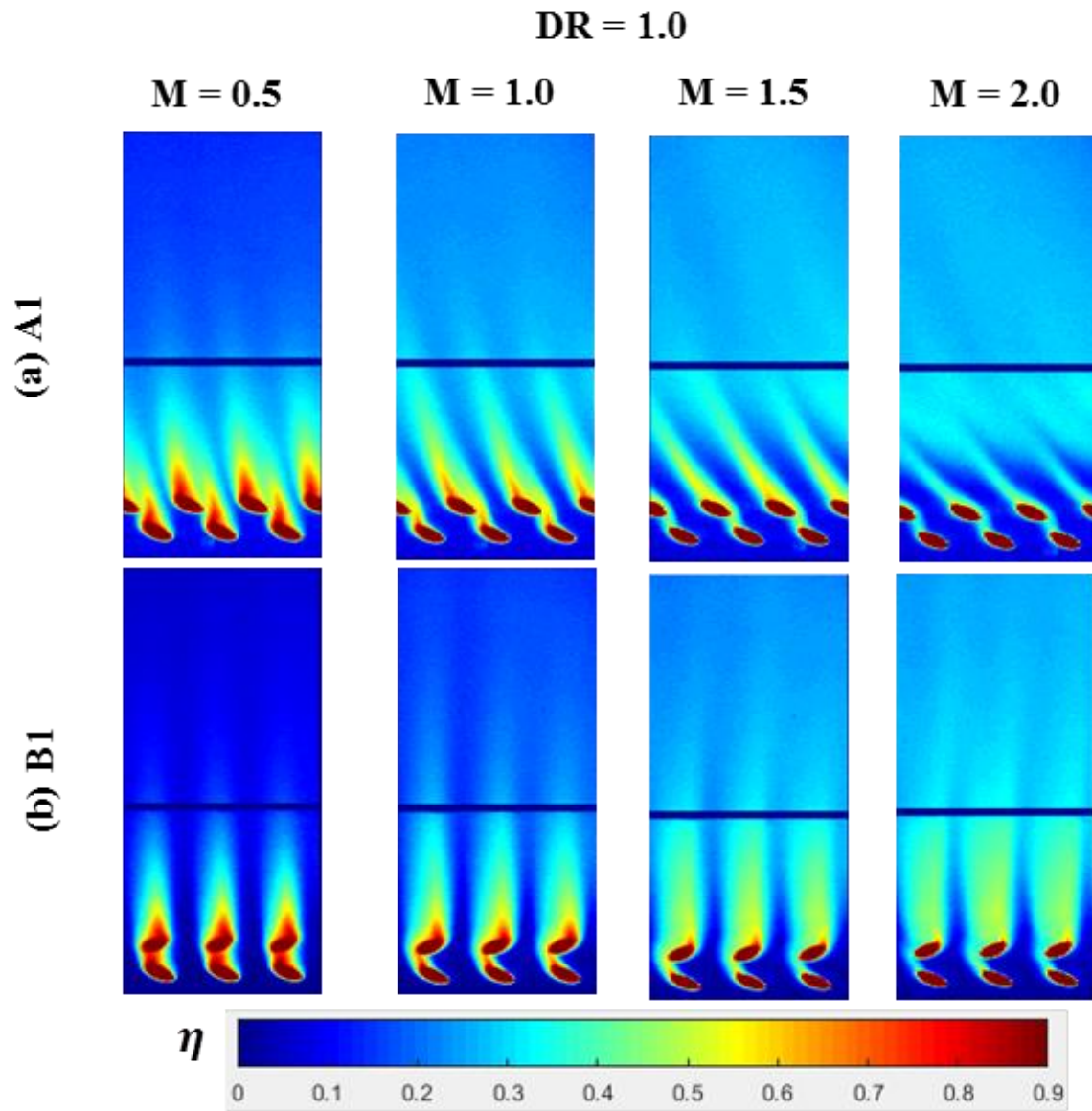
#### 3.3.1 Combined Effect of Blowing Ratio and Geometry

Figure 29 and Figure 30 show the film cooling effectiveness distribution for two designs with increasing blowing under  $DR = 1.0$  and  $DR = 2.0$  respectively. The results of  $p/d = 4$  are selected. The overall characteristics observed from design A and design B is that the film cooling effectiveness is considerably high at the cooling holes ( $\eta \approx 1.0$ ). As extending further away from the cooling holes, the coolant streaks are gradually weakened at lower blowing ratios ( $M = 0.5$  and  $1.0$ ).

As can be seen from design A (Figure 29 (a) and Figure 30(a)), the coolant jets initially attached to the surface at low blowing ratio and started to lift-off from the surface as blowing ratio gradually increasing. Such streaks behavior is not strange, which happens to one-row of the cooling hole as well. Because at higher  $M$ , the coolant jet with higher momentum is more likely to

penetrate into the mainstream flow. From Figure 29 (a) and Figure 30 (a), it is observed that the streaks lift-off from the surface and caused the film cooling effectiveness decreases in the low  $x/d$  region. But the effectiveness increases in the downstream due to coolant reattachment. It is also found that at higher blowing ratio ( $M = 1.5$  and  $2.0$ ), the flow orientations of the streaks are less deflected by the mainstream, because of the higher jet momentum again.

In Fig. Figure 29 (b) and Figure 30 (b), due to the geometry effect, the coolant streaks in design B are very different from the ones in design A. The streaks here are relatively wide and straight. Geometry effect is significant at high blowing ratios. At the blowing ratio of  $2.0$ , the geometry effect is most distinct. The observable coolant jets are remain well attached to the surface. The film streaks are more extensive and straightly extend along the streamwise direction, and the coolant film protects more area than the streaks in design A. In summary, design A performs better than design B at low-mid blowing ratio, but the trend is reversed at higher blowing ratio.



**Figure 29 Film cooling effectiveness distribution at DR 1.0**

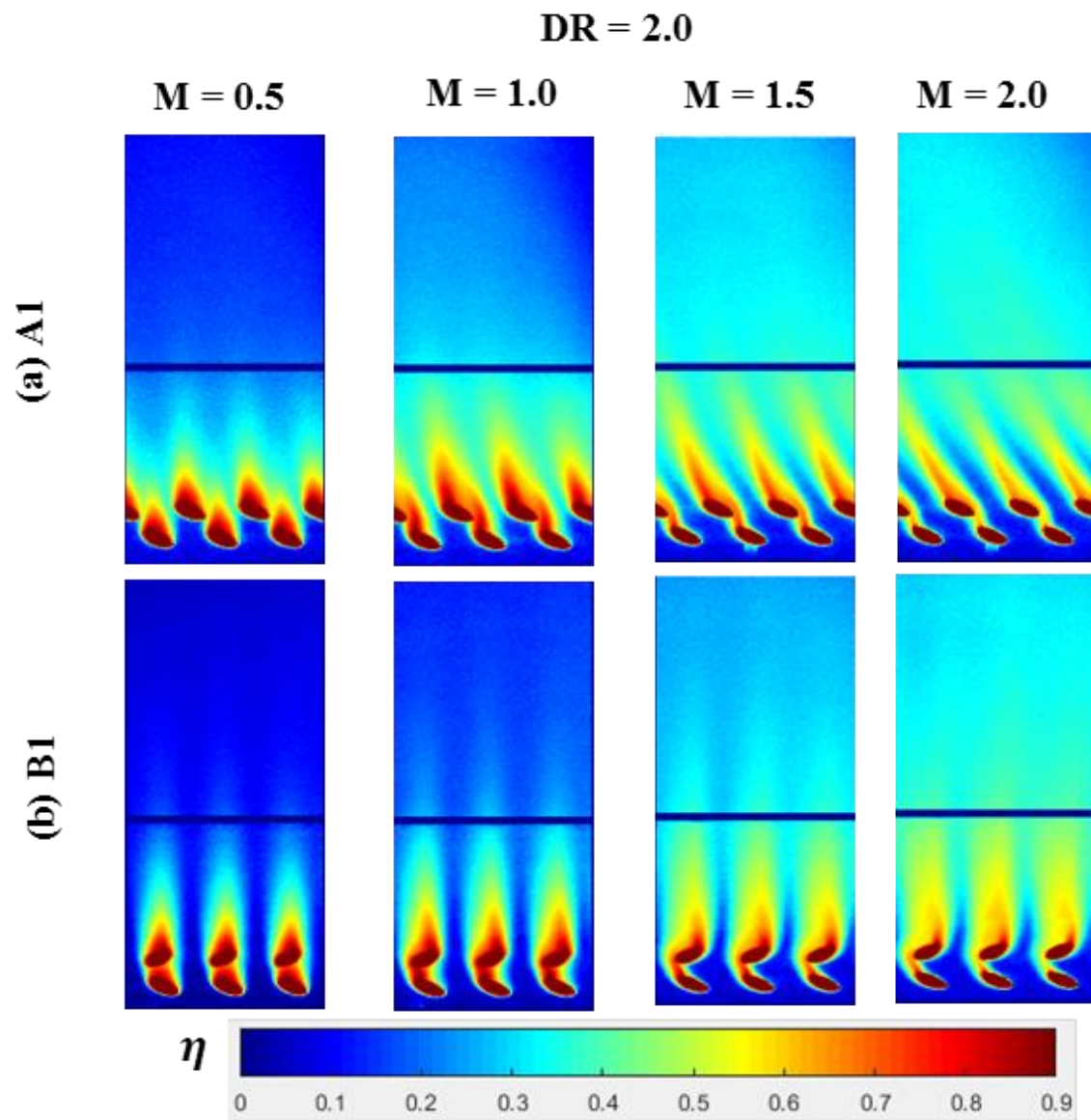


**Figure 30 Film cooling effectiveness distribution at DR 2.0**

The line curves in Figure 31 (a) and Figure 31 (b) give the laterally averaged film cooling effectiveness results corresponding to the contours in Figure 29 and Figure 30 respectively. In design A, at low blowing ratio, the effectiveness monotonically decreases in stream-wise direction. At higher blowing ratio, due to the lift-off and reattachment behavior, the effectiveness firstly declined to a lower value and increases again at about  $x/d = 2.5$ . In design B, blowing ratio has a monotonic effect on the cooling effectiveness, and  $M = 2.0$  produces the highest averaged effectiveness.

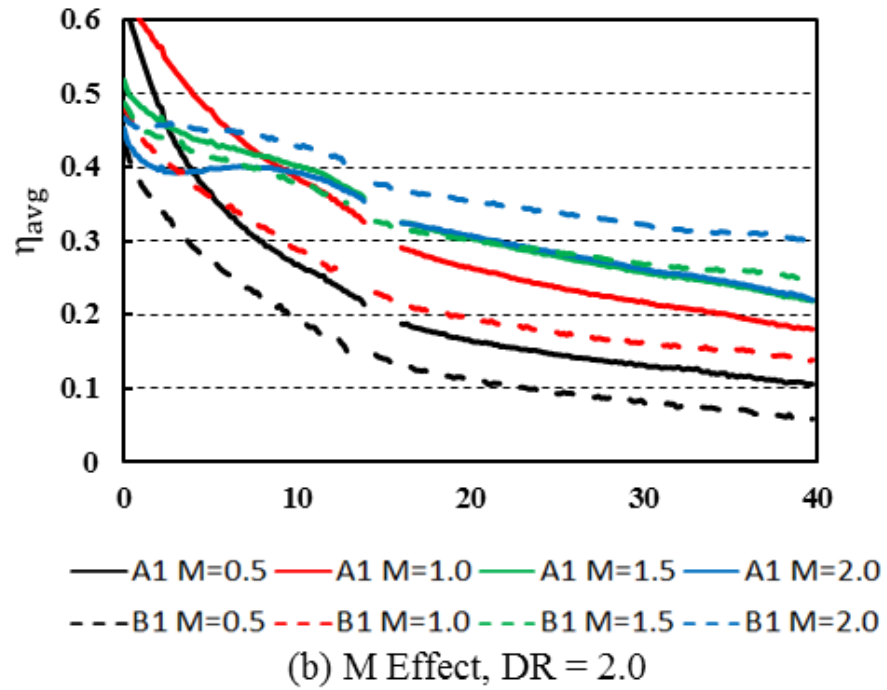
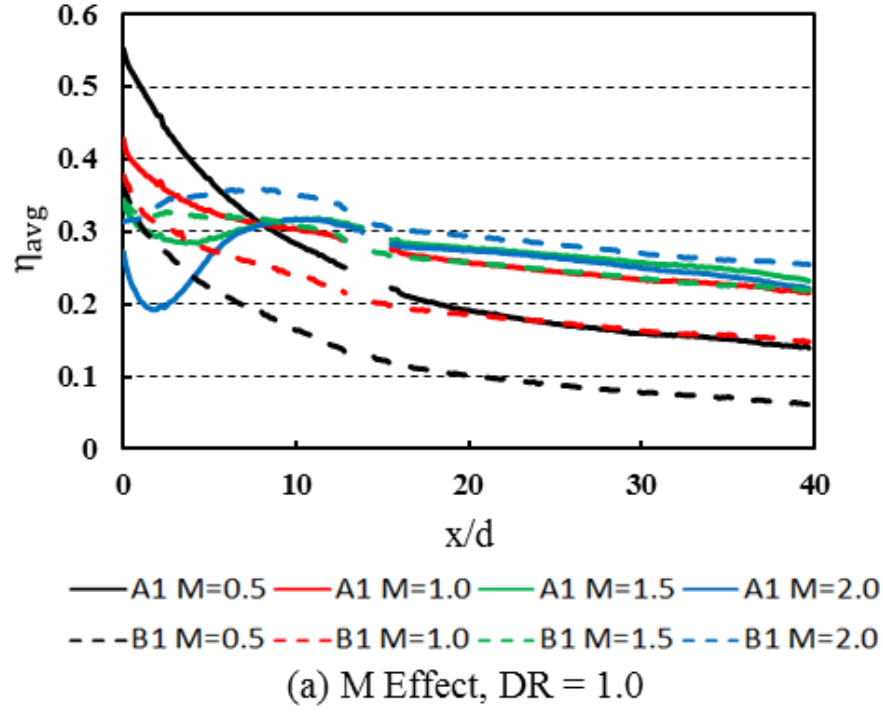
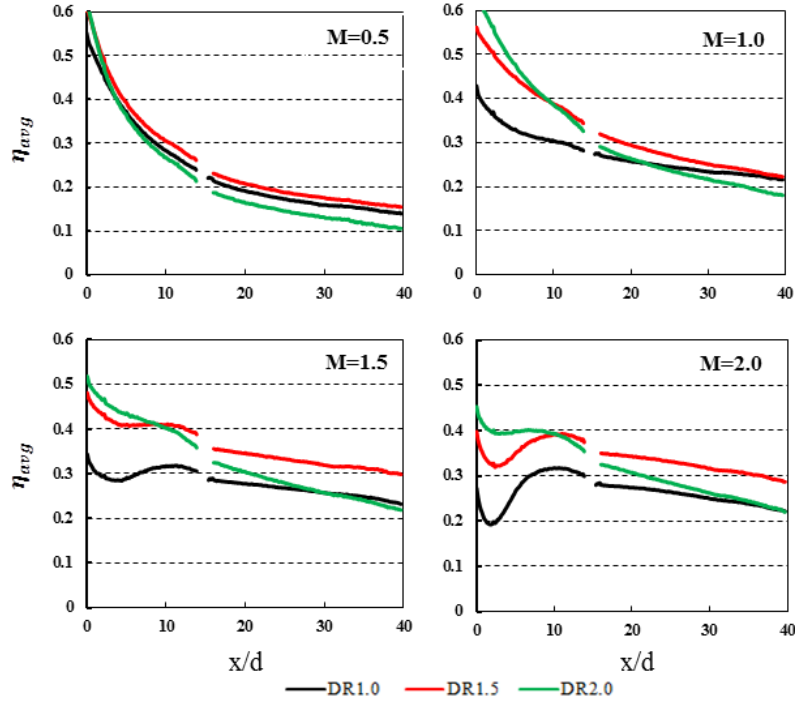


**Figure 31 Laterally averaged film-cooling effectiveness for A1 and B1 with all M (a)  $DR=1.0$  , (b)  $DR=2.0$**

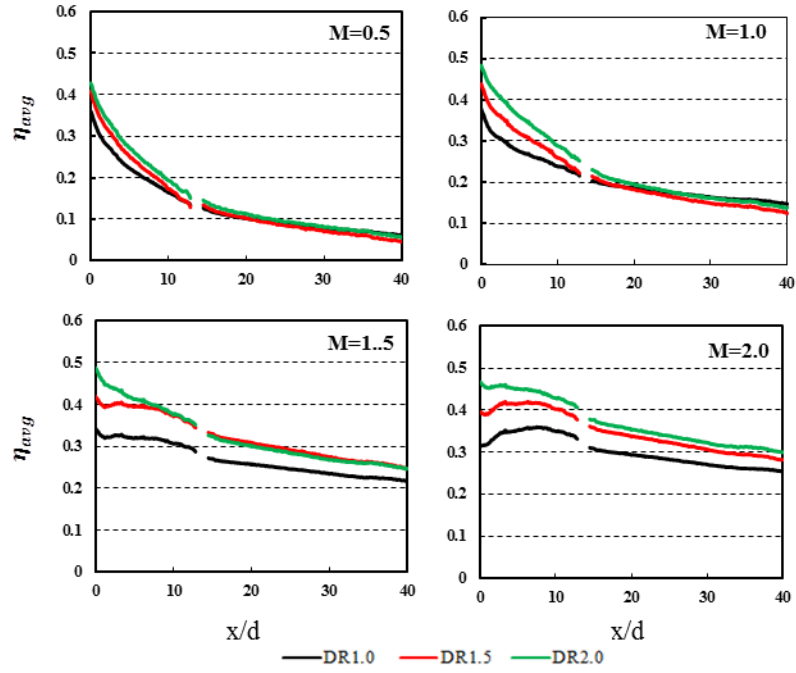
### 3.3.2 Effect of Density Ratio

Density ratio, serving as one of the parameters influencing the cooling performance, generally has a positive impact on cooling effectiveness for a fixed blowing ratio. There are three density ratios  $DR = 1.0, 1.5,$  and  $2.0$  in current tests. In general, increasing  $DR$  produces higher film cooling effectiveness. Because at the same  $M$ , the heavier coolant with less momentum has a lower tendency to lift-off from the surface. Additionally, the coolant jet with lower momentum are less interacted and diluted by the mainstream flow.

To analyze the density ratio effects on the two designs, the laterally averaged cooling effectiveness of  $p/d = 4$  are presented in Figure 32. A common characteristic of cooling effectiveness for both designs is that the density ratio effect at low blowing ratio ( $M = 0.5$ ) is small. This is due to the fact that the high-density coolant does not have the sufficient momentum to have the film propagates far downstream, which results in low performance downstream. It shows that increasing density ratio has a negative impact in design A. From geometry effect aspect, coolant in design A is more likely to lift-off from the surface. Therefore, the heavier coolant helps to reduce the lift-off behavior in the upstream portion, resulting in higher effectiveness. In the downstream portion,  $DR = 1.5$  is better than  $DR = 1.0$  and  $2.0$ . Since the coolant ejected from design B is less susceptible to lift-off from the surface, the density ratio effect is not significant compared with design A. Increasing density produces increasing spanwise averaged effectiveness in design B. It also shows that the increment from  $DR = 1.5$  to  $DR = 2.0$  is smaller than that from  $DR = 1.0$  to  $DR = 1.5$ .



(a) DR Effect, A1,  $p/d = 4$



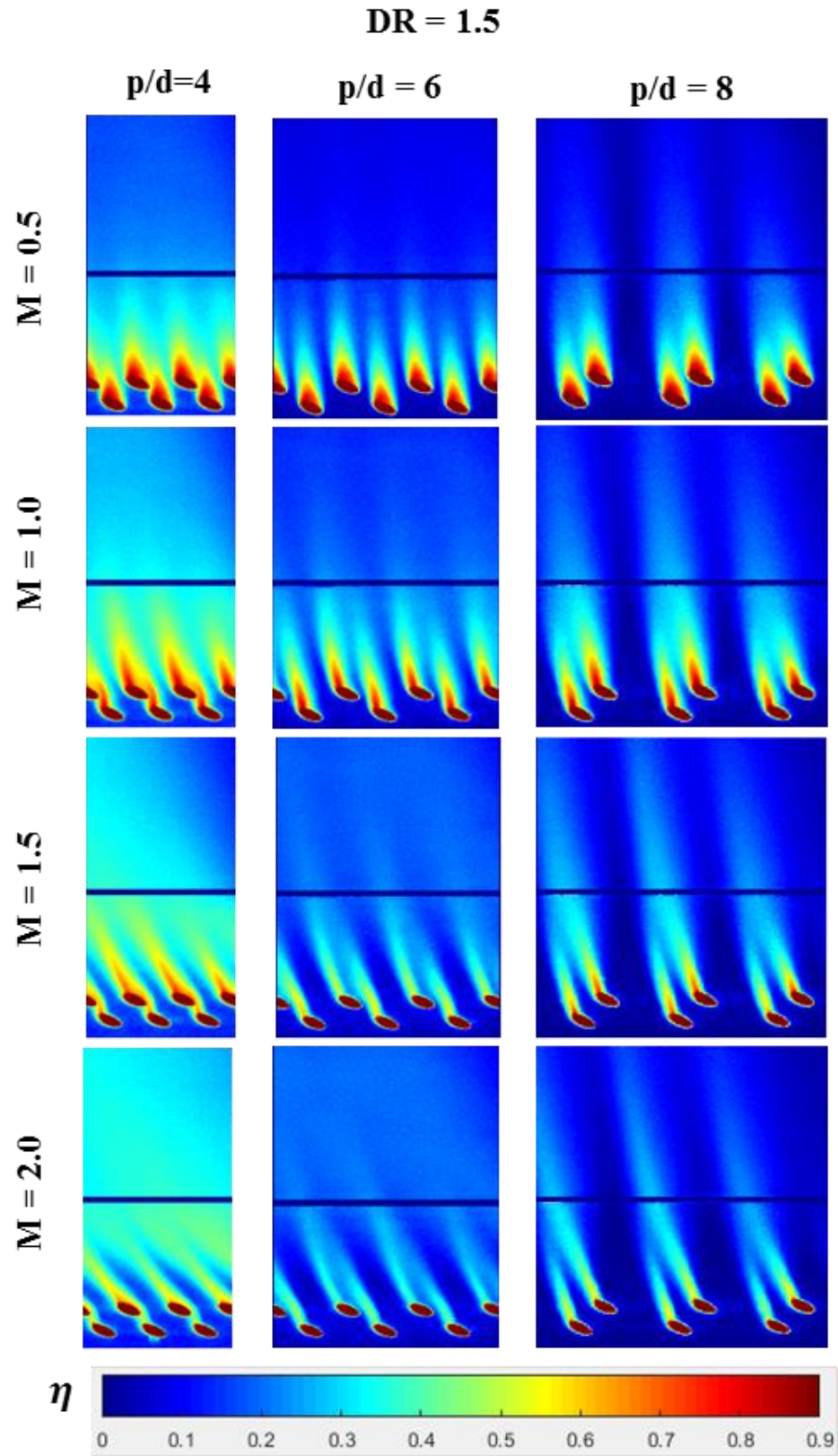
(b) DR Effect, B1,  $p/d = 4$

Figure 32 Laterally averaged film-cooling effectiveness with all  $M$



### 3.3.3 Effect of $p/d$

Figure 33 and Figure 34 present the local film cooling effectiveness distributions concerning  $p/d = 4, 6$ , and  $8$  under all coolant/mainstream conditions for design A and design B respectively. The contours in Figure 33 show that with small hole-spacing the interaction occurred between jets is significant; with large hole spacing ( $p/d = 6$  and  $8$ ), the streaks are more independent, and the interaction between coolant jets is hardly observed. It is noticed that the expected uniform coolant film becomes intermittent jets and results in low spanwise averaged film cooling effectiveness. Design B in Figure 34 has a similar effectiveness variation trend.



**Figure 33 Film cooling effectiveness distribution of design A at DR = 1.5**

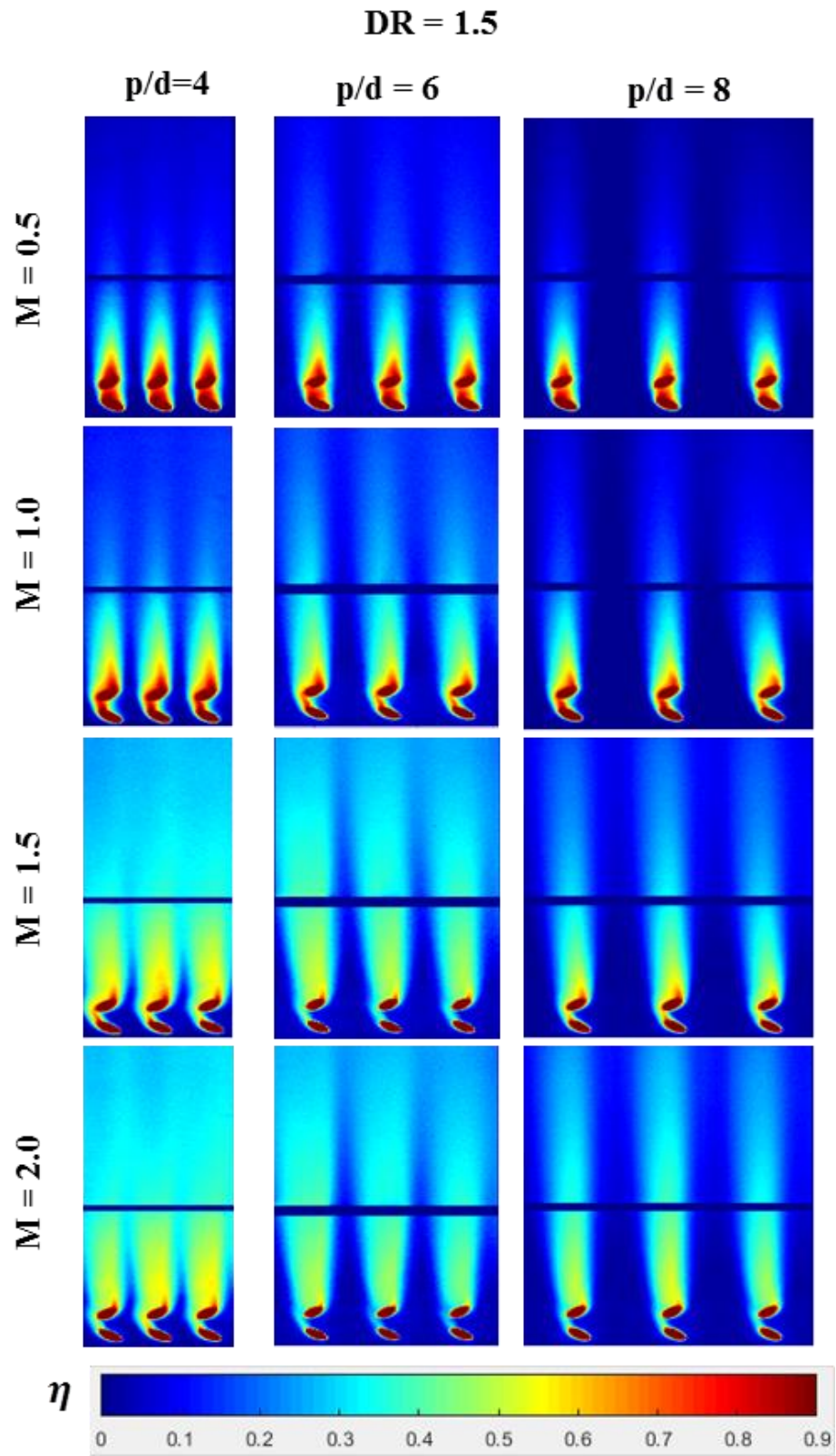


**Figure 34 Film cooling effectiveness distribution of design B at DR = 1.5**

Figure 35 and Figure 36 compare the laterally averaged film cooling effectiveness ( $\eta_{avg}$ ) corresponding to Figure 33 and Figure 34. The figures suggest that as the hole spacing increasing, the spanwise averaged film cooling effectiveness decreases consistently. One apparent reason is that the increasing of  $p/d$  reduces the number of cooling hole in the calculated region. With less cooling hole per row, the area protected by the coolant decreases, resulting in lower film cooling effectiveness. However, the reduction of effectiveness value is not always linear with the decreasing number of cooling holes. It shows that the number of cooling holes reduced by half, the reduction of cooling effectiveness is not necessarily half. This implies that the interaction and coalescence between coolant jets play an essential role in determining the film effectiveness. The figures also reveal that smaller hole-spacing design is relatively more sensitive to the variation of density ratio, i.e., A1 & B1 is more prone to be influenced by density ratio than A2 & B2 and A3 & B3.

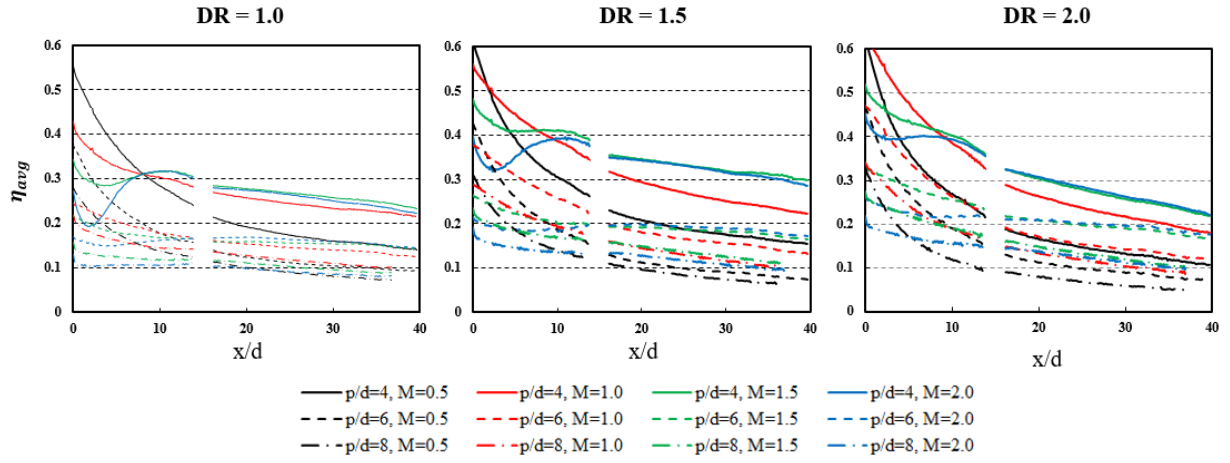


**Figure 35 Effect of  $p/d$  on spanwise averaged effectiveness on design A**

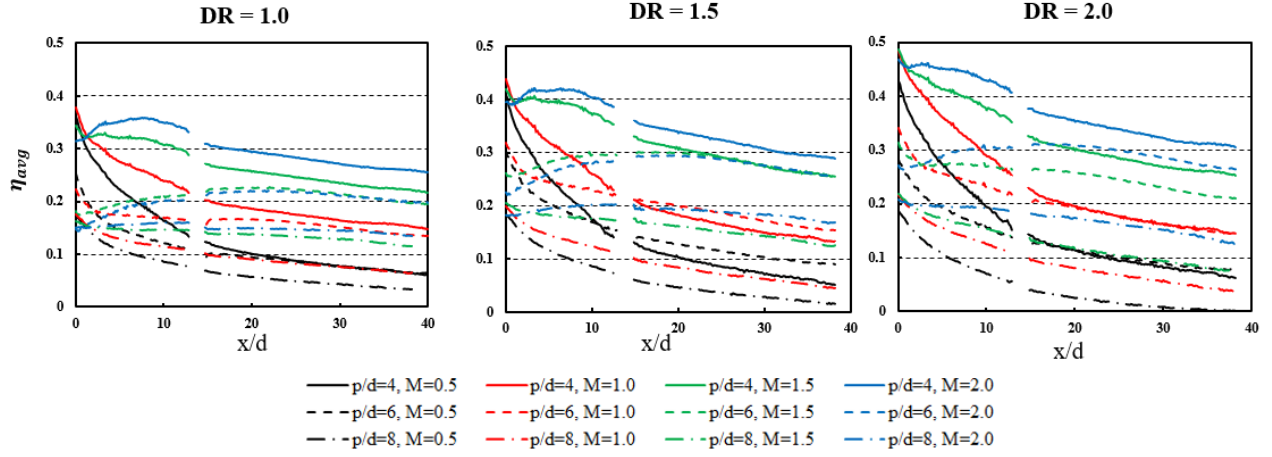
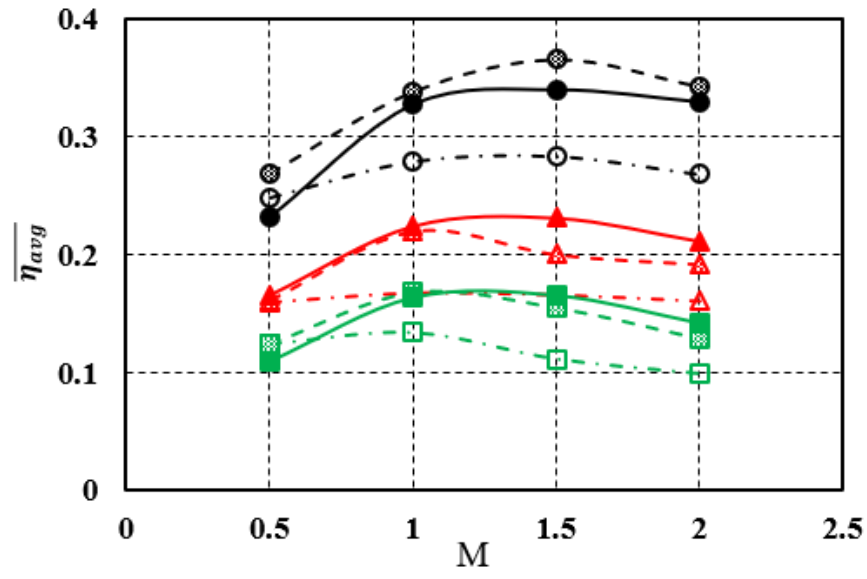


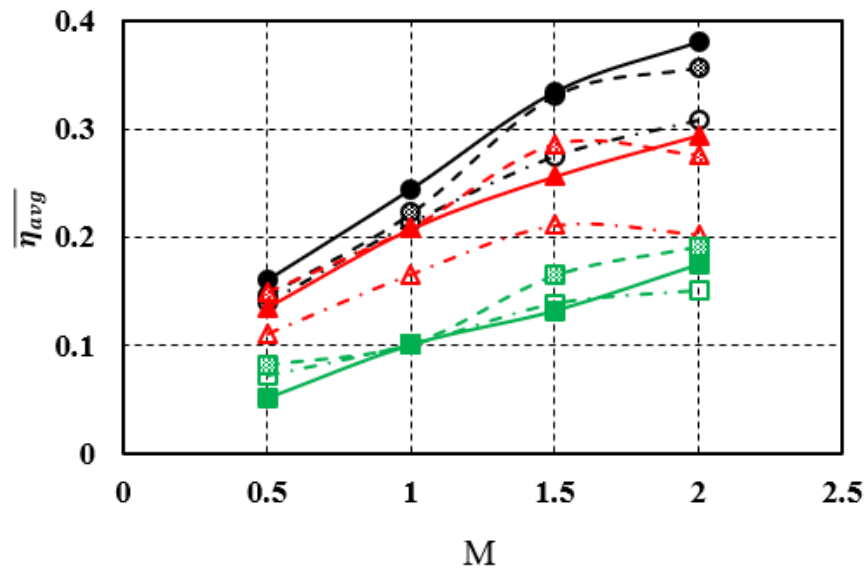
**Figure 36 Effect of  $p/d$  on spanwise averaged effectiveness on design B**

### 3.3.4 Area averaged film cooling effectiveness

Figure 37 shows the area averaged cooling effectiveness ( $\overline{\eta_{avg}}$ ) for design A and design B respectively. The region used to calculate the area averaged effectiveness ranges from  $x/d = 0$  to 35. For each geometry, 36 cases are shown including four blowing ratios, three density ratios, and three  $p/d$  designs. The effectiveness is largely affected by  $p/d$  ratio. The area-averaged effectiveness of  $p/d = 4$  is much higher than  $p/d = 6$  and 8. Blowing ratio effect takes the second place. For design A, area averaged effectiveness first increases and then decreases when  $M$  increases from 0.5 to 1.0, 1.5, and 2.0. It seems that the value of  $M$ , which corresponding to the highest averaged effectiveness, increases when  $DR$  increases or  $p/d$  decreases. For design B, in general, area averaged effectiveness increases when  $M$  increases. Increasing  $M$  produces relatively stable variation in design A but an escalating trend in design B, which is mainly due to the geometry effect.



(a) Area averaged cooling effectiveness of design A



(b) Area averaged cooling effectiveness of design B

**Figure 37 Area averaged cooling effectiveness**



### 3.3.5 Two- row compound cylindrical Holes Correlation

To consolidate the information and provide the designers a straightforward approach to applying the film cooling design proposed in this study, an attempt for individual correlations development of the spanwise averaged effectiveness for design A and B are proceeded based on the current datasets (72 sets). All the parameters in this study are included in the correlations, the form of the correlations for the current two-row hole configurations are proposed in Eq. (3.5).

$$\bar{\eta} = K \frac{M^{c3} DR^{c4}}{\left(\frac{x}{d}\right)^{c1} \left(\frac{p}{d}\right)^{c2}} \quad (3.5)$$

Equation (3.5) can be further linearized as Eq. (3.6),

$$\begin{aligned} \ln(\bar{\eta}) = & \ln(K) + c3 \cdot \ln(M) + c4 \cdot \ln(DR) \\ & - c1 \cdot \ln\left(\frac{x}{d}\right) - c2 \cdot \ln\left(\frac{p}{d}\right) \end{aligned} \quad (3.6)$$

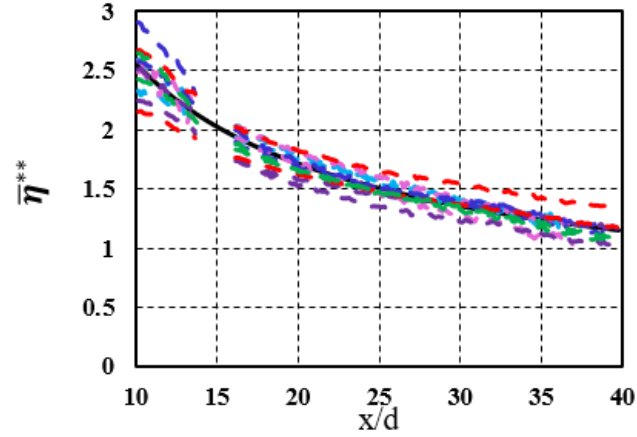
With the linearized form of Eq. (3.5) as above, the coefficients (K, c1, c2, c3 and c4) were determined by multiple linear regression using Minitab® 18. Since the linear models were used to conduct the regression analysis, the coefficient of determination ( $R^2$ ) can be used to statistically explain the percentage of the variation in averaged effectiveness by the regression model in the pre-defined parameter range.

A preliminary analysis on the overall data trend was performed to make sure the proposed correlations are meaningful with satisfactory predictability. First, only the mid and high DR data are included. Second, from Figure 37 (a), it is found that for design A, a monotonic effectiveness variation trend can be achieved if the data is divided into two groups using  $M = 1.0$ . Two separate coefficients sets were therefore proposed to correlate the averaged effectiveness for design A in the lower M ( $0.5 \leq M \leq 1.0$ ) region and higher M ( $1.0 \leq M \leq 2.0$ ) region, respectively. Similarly, from Figure 37 (b), it is found that the effectiveness decay is not uniform when

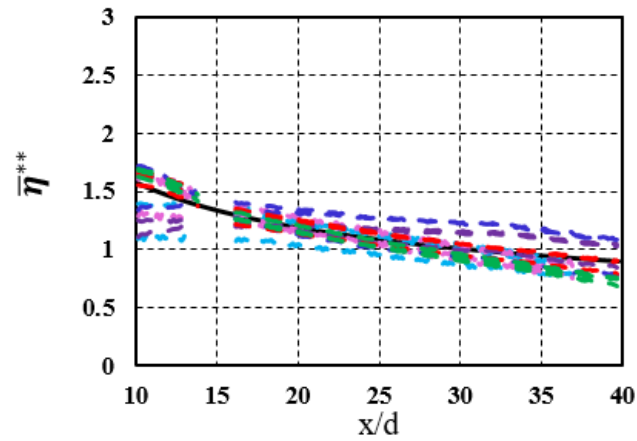
increasing  $p/d$  under different  $M$  for design B. So, two separates coefficients were used to correlate the averaged effectiveness for design B in the lower  $p/d$  ( $p/d = 4, 6$ ) region and higher  $p/d$  ( $p/d = 6, 8$ ) region, respectively. However, the data of design B when  $p/d = 8$  are unable to be correlated with a satisfactory  $R^2$  value, therefore, unlike design A, the correlation for design B is presented for lower  $p/d$  only. The coefficients in Eq. (3.5) with applicable parameter range and the corresponding  $R^2$  values are shown in Table 3. The data used in the correlation development are plotted in terms of  $\bar{\eta}^{**}$  to demonstrate how data are scattered around the correlation curve as shown in Figure 38 (the solid black line is the correlation and the scattered dots are the data in this study).  $\bar{\eta}^{**}$  is defined as,

$$\bar{\eta}^{**} = \frac{\bar{\eta} \left( \frac{p}{d} \right)^{c_2}}{M^{c_3} D R^{c_4}} \quad (3.7)$$

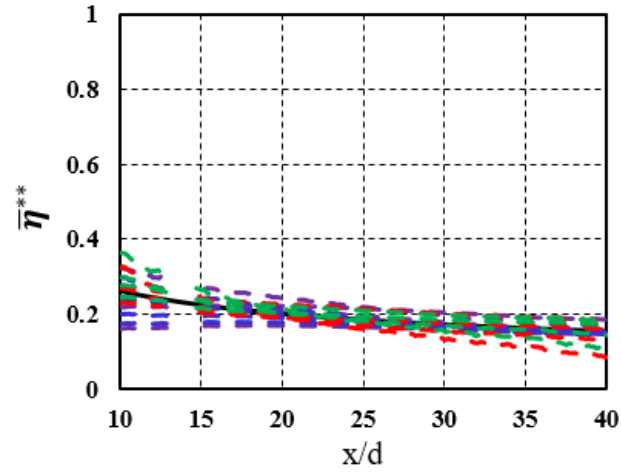
From Figure 38, it is clear that the proposed correlations for the two-row configurations can capture the effectiveness variation in both value and trend within the study parameter range.



(a) Design A,  $0.5 \leq M \leq 1.0$



(b) Design A,  $1.0 \leq M \leq 2.0$



(c) Design B,  $4 < p/d < 6$

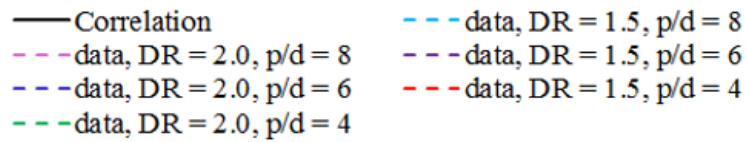


**Figure 38 Data distribution along the proposed correlation**

### 3.4 Conclusions

The film cooling performance of two-row of compound angle cylindrical hole with two hole-geometries is investigated by PSP technique. Based on the experimental results, some critical observations and finding are summarized below.

1. Blowing ratio effect. Coolant ejected from design A is prone to lift-off from the surface and mixing with the mainstream flow at higher blowing ratios. It directly resulted in the decrease of cooling effectiveness. Due to geometry effect, the injectant from design B well attaches to the surface and keeps increasing film cooling effectiveness as the blowing ratio increases. Hence, at higher blowing ratio conditions, design B is preferred over design A.

2. Hole geometry effect. Generally the staggered row arrangement is expected to produce higher effectiveness than the inline row arrangement. However, combined the effect from the hole orientation angle, the inline row with opposite angle (design B) orientation produces higher effectiveness than staggered one (design A), especially at higher blowing ratio.

3. Density ratio effect. DR has significant effect from 1 to 1.5, but the effect is greatly diminished between 1.5 and 2.0. Results indicate that the film effectiveness is less influenced by density ratio compared to the blowing ratio effect and geometry effect.

4. Hole spacing effect. Large hole-spacing ( $p/d = 6$  or  $8$ ) is not favorable. Because it causes non-uniform film cooling effectiveness distribution in the spanwise direction, the area between cooling holes hardly can be protected. But it considerably reduces the coolant consumption.

5. Area averaged effectiveness. Compared with the two designs in terms of area-averaged effectiveness, for  $M = 0.5$  and  $1.0$ , design A is better than design B; for  $M = 1.5$ , design A is a little better at high-density ratio ( $DR = 2.0$ ) and design B is a little better at low-density ratio ( $DR = 1.0$  and  $1.5$ ); for  $M = 2.0$ , design B is better than design A.

6. Two-row flat plate film cooling correlations. Flat-plate span-wise averaged film cooling effectiveness correlations have been developed for two-row compound angle cylindrical holes over a range of flow and geometry parameters. These correlations can be useful for the preliminary turbine blade film cooling design selection and analysis.

## **4. TURBINE VANE ENDWALL FILM COOLING FROM MID-CHORD OR DOWNSTREAM ROWS AND UPSTREAM COOLANT INJECTION**

### **4.1 Experimental setup and method**

The measurement were conducted in a four-passage, high-speed wind tunnel facility as shown in Figure 39. Chowdhury et al. [62] described more details of this cascade facility. A 325 psi high-pressure compressor supplies the mainstream air. Before entering the linear cascade test section, the mainstream air flows through a dryer and a storage tank. The mainstream velocities at inlet and exit were determined by recording the total pressure and the static pressure locating at  $0.5C_{ax}$  upstream of the vane's leading edge and trailing edge respectively. The inlet mainstream speed can be as high as 33.96 m/s. A turbulence grid was installed at  $2.72 C_{ax}$  upstream of the vane's leading edge, which creates a turbulence intensity of about 19% with an integral length scale 1.7cm, measured by the hot-wire anemometer. The coolant supplying system consists of a medium-pressure compressor, a dryer, and a storage tank. Three foreign gas cylinders: N<sub>2</sub>, CO<sub>2</sub>, and SF<sub>6</sub> & Ar mixture, are connected to upstream injection plenum and the endwall injection plenum for providing the coolant with different density ratio. The cascade test section is mainly made of aluminum, while the center endwall plate and the upstream injection plate are formed by the SLA process using a material called Accura® Xtreme™ White 200. There is a transparent window on the top of the center endwall, which allows the optical access to the area of interest. Two LED excitation lights and CCD camera were equipped for the PSP measurement procedure.

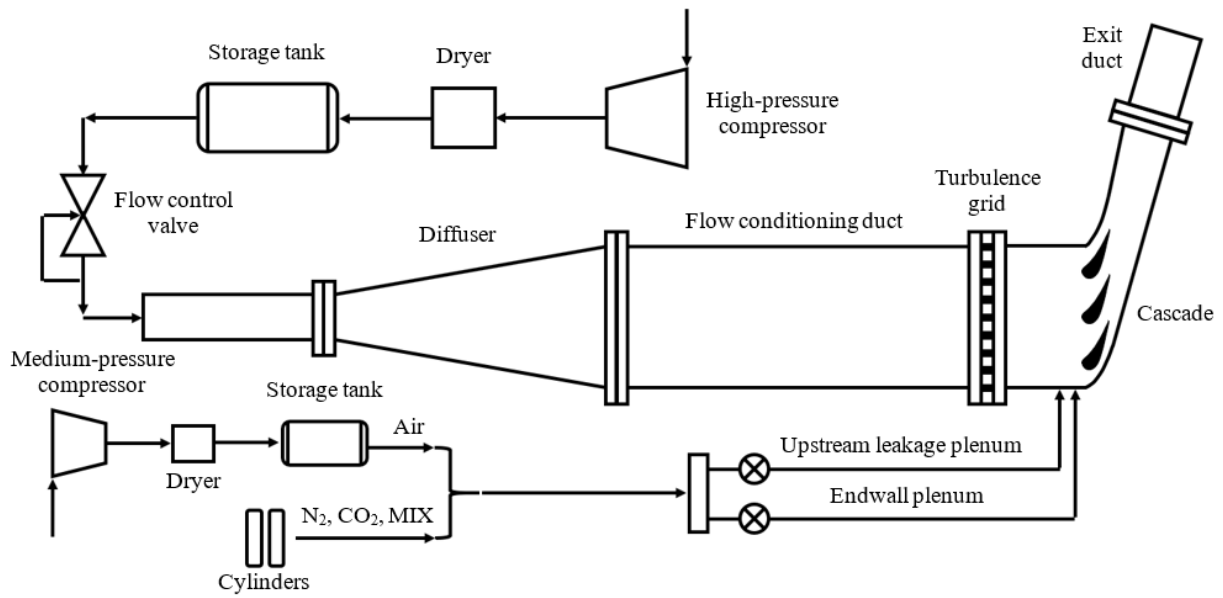


**Figure 39 Flow loop of the endwall cascade facility**

Figure 40 clearly shows a three-dimension view of the endwall test section. It mainly consists of the upstream injection plate, the simulated turbine vane airfoils and the endwall injection plate. The injection plate is made of the SLA material. As it shows, there are two-row of staggered film cooling holes: 37 holes in the first row and 38 holes in the second row, totally 75 holes. With the hole-diameter of 0.175cm and the row-row spacing is fixed at  $4d$ . The second row locates  $0.38C_{ax}$  upstream from the vane's leading edge. The injection angle of the upstream coolant is fixed at  $30^\circ$ .

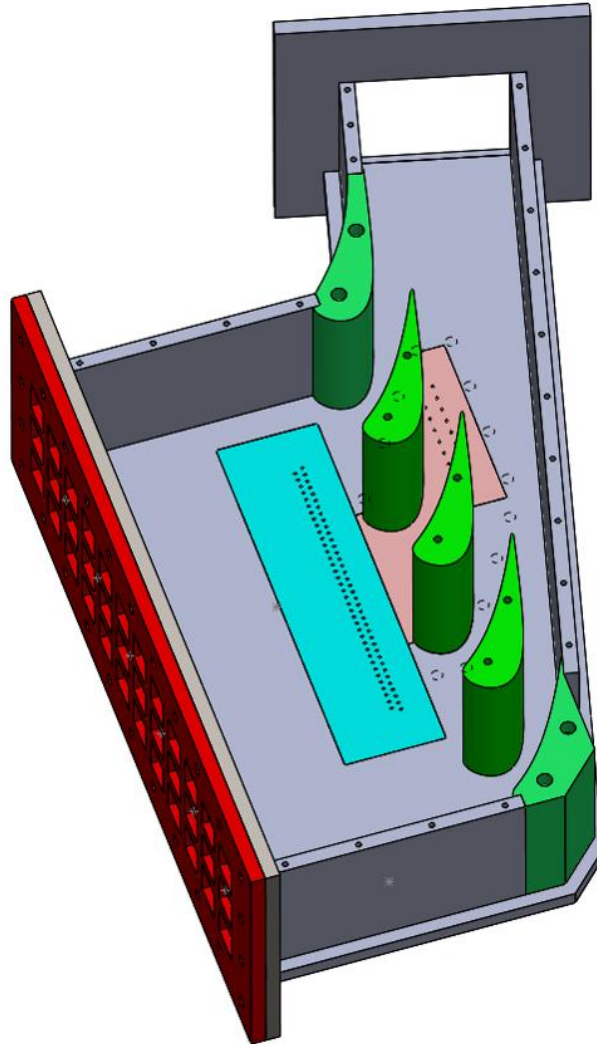


**Figure 40 Schematic view of the endwall test section**



Figure 41 shows the schematic view of the two endwall cooling-hole configurations. To evaluate the potential coverage from the upstream injection on the endwall passage, we designed endwall cooling holes at the mid-chord region or the downstream region, named as mid-chord row and downstream row. There are nine cooling holes per row. The cylindrical hole diameter on the endwall is fixed at 0.15cm; the inclination angle is  $30^\circ$  and the hole exit angle is  $20^\circ$ . For the hole in mid-chord row and downstream row, the pitch to diameter ratio is 6 and 8, respectively.

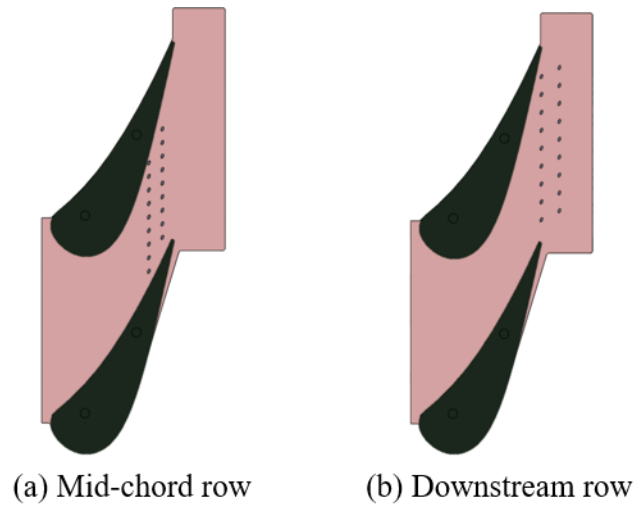


**Figure 41 Schematic of film-hole patterns on the endwall**

## 4.2 Test Matrix

Two endwall cooling configurations: mid-chord row and downstream row with upstream injection were tested under a various cooling condition, summarized in Table 4. Case no.3 with  $IL = 1\%$ ,  $EW = 1.0\%$  and  $DR = 1.5$  serves as the baseline case.  $CO_2$  are used for providing the cooling condition at  $DR = 1.5$  for case 1 to case 7; Nitrogen was used for case 8 at  $DR=1.0$ ; to simulate engine-like condition ( $DR=1.7\sim 2.0$ ), mixture gas with 15%  $SF_6$  and 85% Ar are used to obtain  $DR = 2.0$  for case 9. Nine tests were performed for each configuration to evaluate the effects of endwall injection, upstream injection and the effects of density ratio, additionally, the optimized coolant combination of upstream and endwall injection can be obtained.

**Table 4 Test matrix for endwall film cooling study.**

Case No.	MFR (%)			DR
	IL	EW	$\Sigma$	
1	1.0	0	= 1.0	1.5
2	1.0	0.5	= 1.5	1.5
<b>3 (BL)</b>	<b>1.0</b>	<b>1.0</b>	<b>= 2.0</b>	<b>1.5</b>
4	1.0	1.5	= 2.5	1.5
5	0	1.0	= 1.0	1.5
6	0.5	1.0	= 1.5	1.5
7	1.5	1.0	= 2.5	1.5
8	1.0	1.0	= 2.0	1.0
9	1.0	1.0	= 2.0	2.0

### 4.3 Experimental results and discussion

In this section, the results are presented with detail effectiveness contours obtained by using the PSP technique so the uncooled or over-cooled areas can be directly identified. The pitchwise averaged film cooling effectiveness for all cases are plotted to compare the cooling effectiveness level. Lastly, the area-averaged film cooling results are summarized for geometry, coolant amount and density ratio selection.

Effects of the endwall MFR ratio, upstream MFR ratio and the density ratio for the two configurations are discussed. It is noteworthy that there is a junction between the upstream injection plate and the endwall injection plate, so the data at this location appears as a discontinuity in all line plots. Additionally,  $x/Cax = -0.5$  denotes the upstream edge of the first row of the upstream injection.

#### 4.3.1 Endwall film cooling MFR effect

Figure 42 (a) and Figure 42 (b) show the local film cooling effectiveness distributions for studying the endwall injection effects for the mid-chord row and the downstream row respectively. In Figure 5, the MFR at the upstream injection is fixed at  $IL = 1.0\%$  and the DR is fixed at  $DR = 1.5$ ; but the mass flow ratio of the endwall injection is varying from  $EW = 0\%$  to  $1.5\%$ . It is firstly noticed that the film contours are deflected from the pressure side to the suction side due to the pressure distribution in the flow field. Since the cooling condition at the upstream is fixed at  $IL = 1\%$  and  $DR = 1.5$ , so the effectiveness distributions upstream from the endwall injection are quite stable and consistent for all four MFR cases in each configuration. As the increasing MFR at the enwall injection, the overall cooling effectiveness is gradually improved and the area of higher-effectiveness zone is enlarged for both designs. The film covered areas in the downstream cases are wider, but the effectiveness levels are lower as compared to the mid-chord cases.

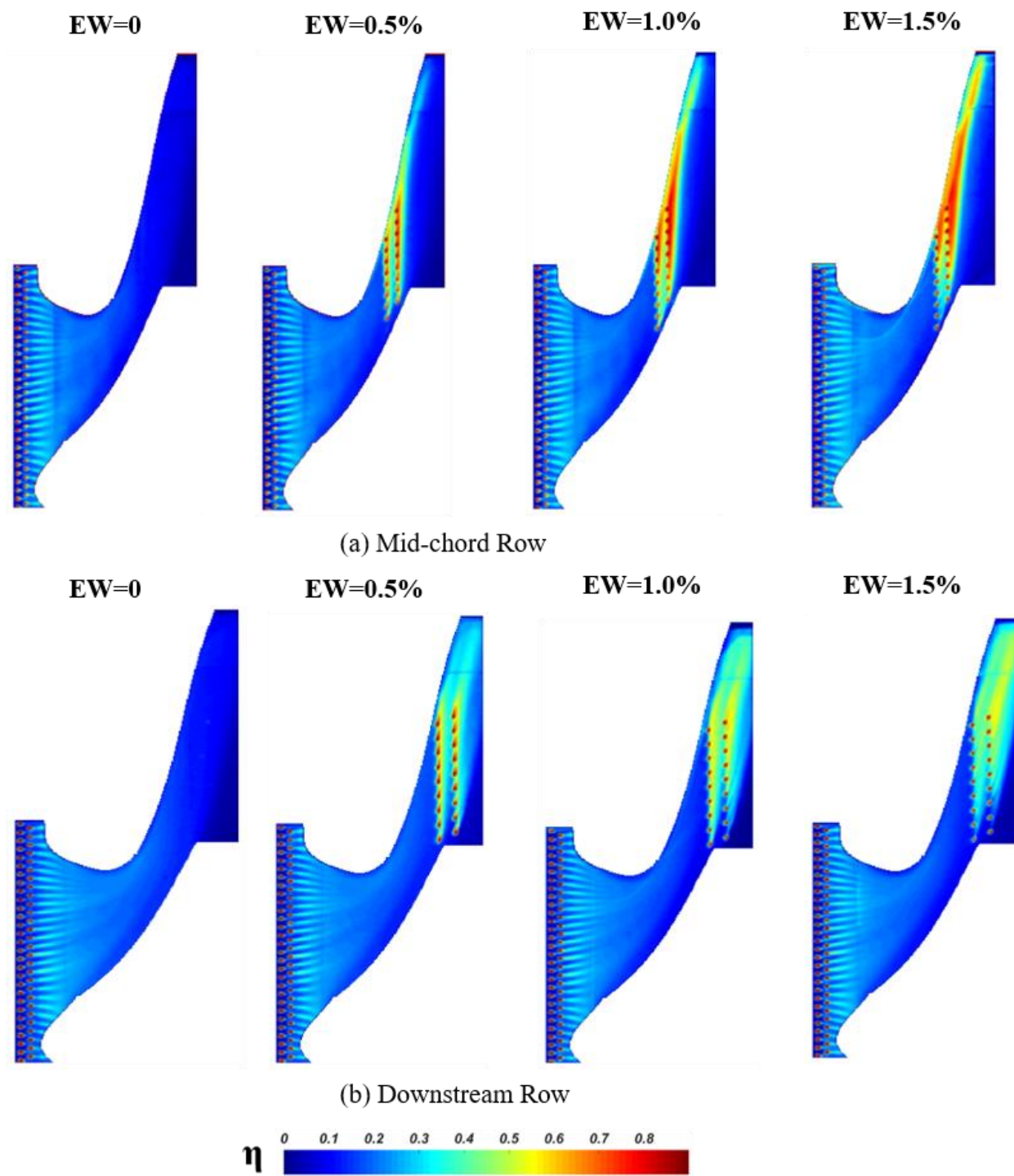
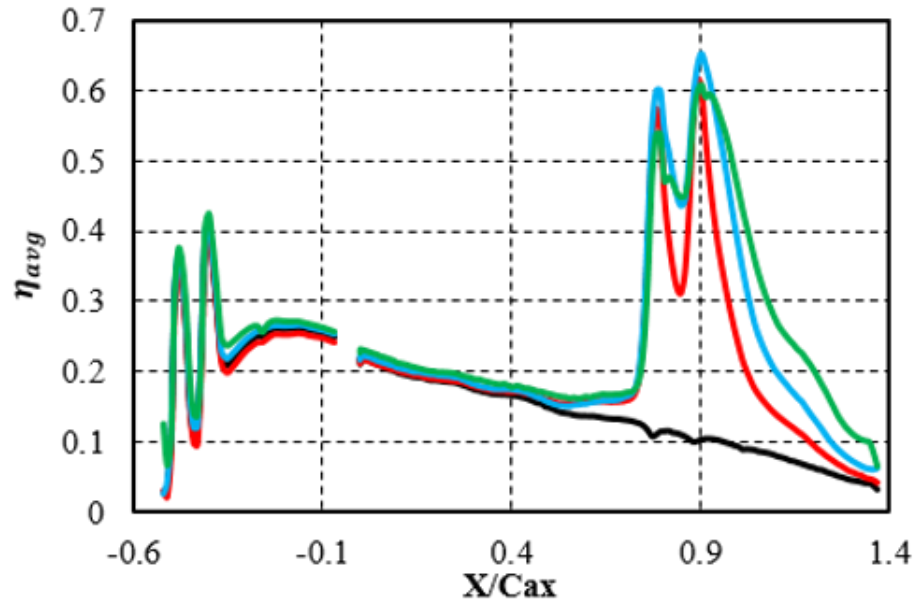
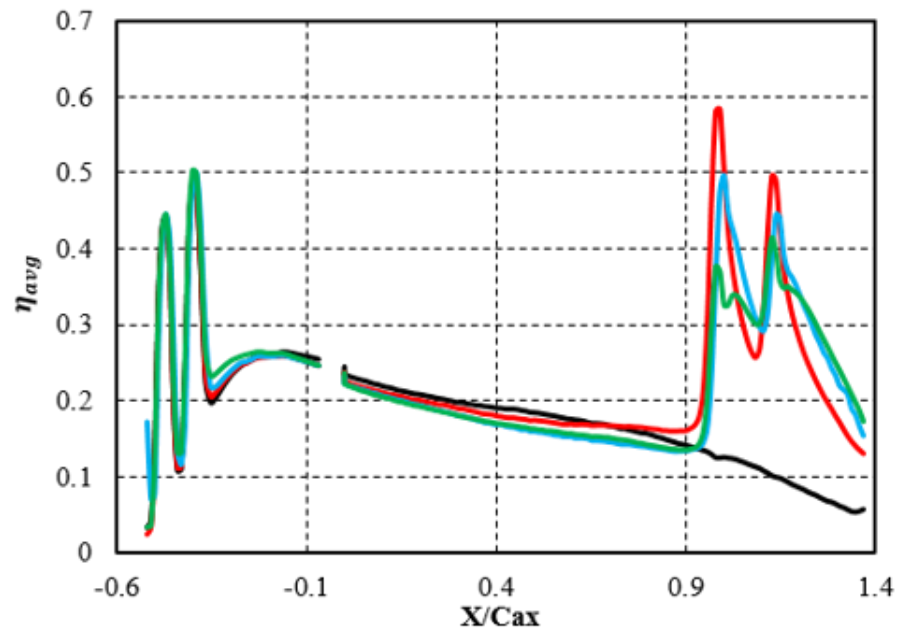


Figure 42 Local film cooling effectiveness, IL=1.0%, DR=1.5

Figure 43 (a) and Figure 43 (b) shows the pitchwise averaged film cooling effectiveness distribution corresponding to the contours given in Figure 42. As the upstream cooling condition:  $IL = 1\%$ ,  $DR = 1.5$  is fixed, it shows the typical two-row film cooling distribution patterns as expected: there are two peak effectiveness values ( $x/Cax = -0.48$  and  $-0.4$ ), then the cooling effectiveness decreases gradually with increasing  $x/Cax$ . Due to the two-row injection at the mid-chord/downstream region, there are two peak effectiveness values, then the effectiveness drastically decreases at further downstream. At the enwall injection region, the film cooling effectiveness are found to increase with the increasing the MFR for the mid-chord design, but the reversed trend is found for the downstream design. According to the contours and the plots, the downstream case provides diffusive but lower effectiveness distribution as compared to the mid-chord case.



(a) Mid-chord row



(b) Downstream Row

Figure 43 Pitchwise averaged film cooling effectiveness, IL=1.0%, DR=1.5

#### 4.3.2 Upstream film cooling MFR effect

Figure 44(a) and Figure 44(b) show the local film cooling effectiveness distributions for studying the upstream injection effects for the two endwall configurations respectively. In Figure 7, the cooling condition at the endwall injection is fixed:  $EW = 1\%$  and  $DR = 1.5$ . The MFR at the upstream injection is varying from  $IL = 0\%$  -  $1.5\%$ . With  $EW = 1\%$  and  $DR = 1.5$  is fixed, the cooling effectiveness immediately downstream from the endwall injections for both configurations are relatively high, indicated by the red and yellow color. As the upstream injection varies from  $IL = 0$  -  $1.5\%$ , it is noticed that at  $IL = 0$ , no film coverage is observed before the mid-chord or downstream film holes. With the MFR at the upstream increasing, the cooling effectiveness is gradually increased and the film covered area is increased as well as expected. For both endwall configurations, the film is clearly deflected from the pressure side to the suction side, however, the downstream cases are less shifted compared to the mid-chord ones and resulted in more uniform film coverage. The upstream injection also shows a positive influence on the cooling performance downstream from the endwall injection. With higher MFR of the upstream injection, the pitchwise distribution near the trailing edge region is more uniform and the film covered area extends further.



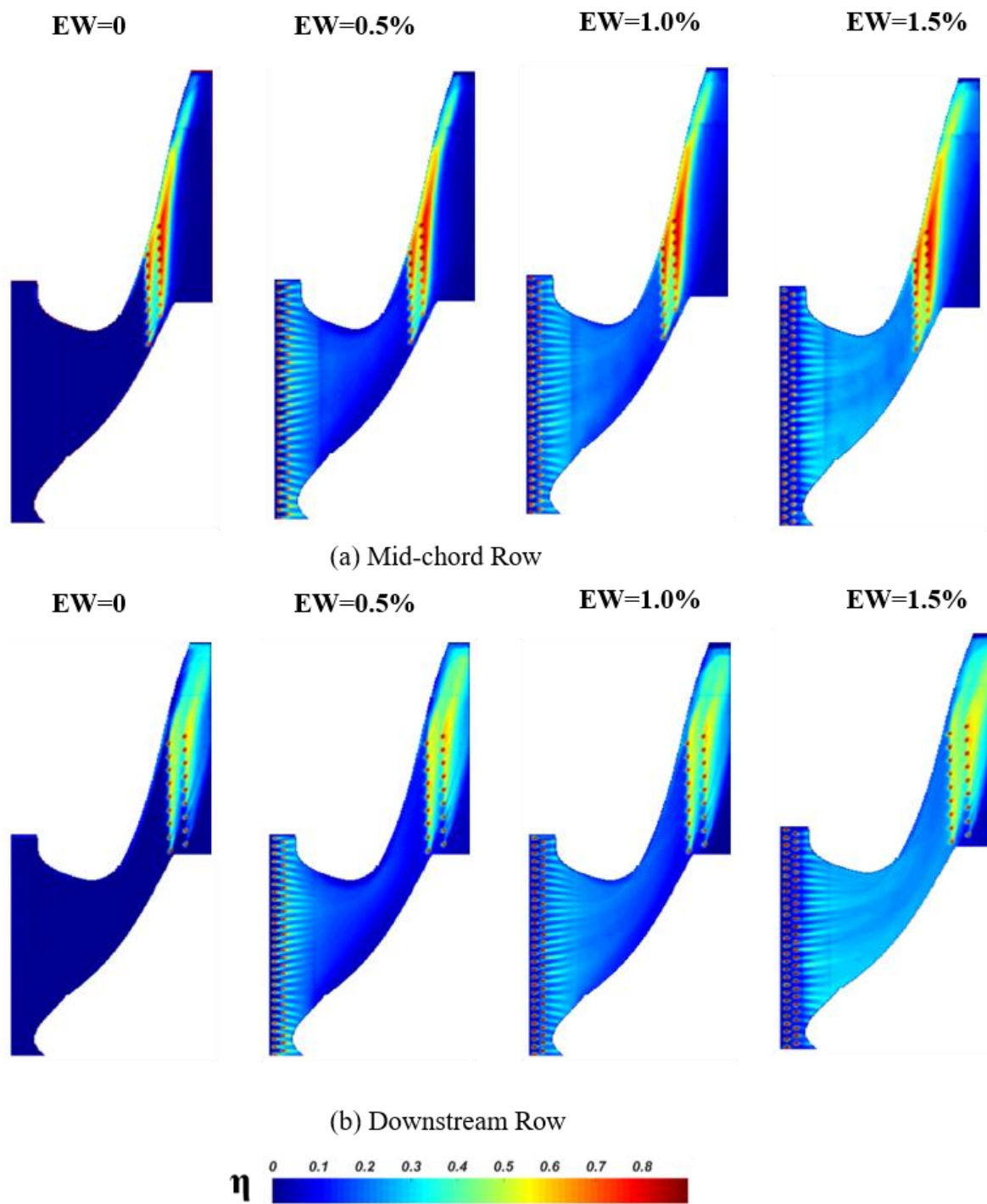
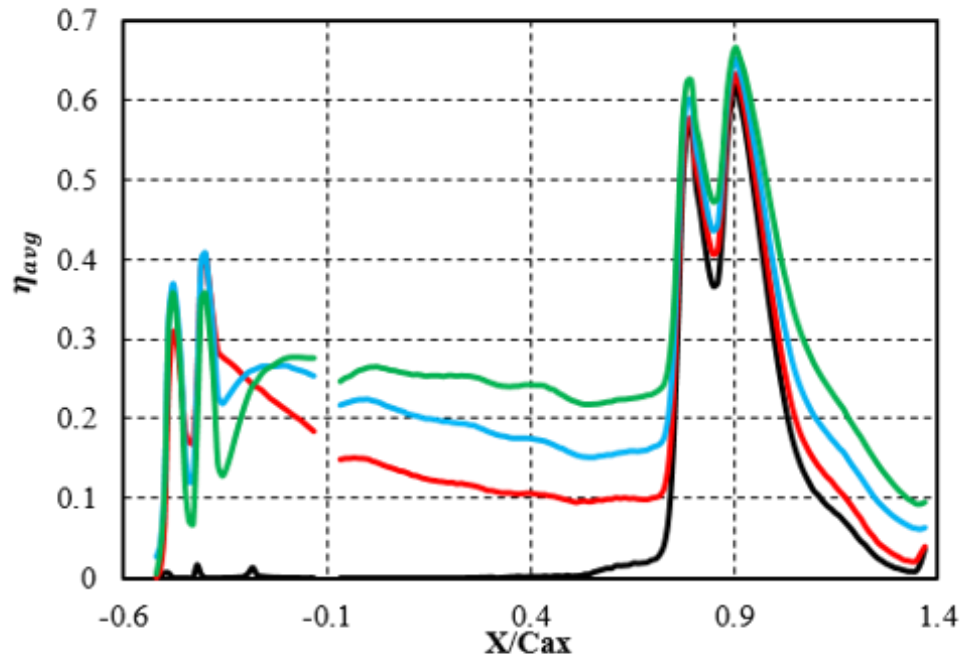
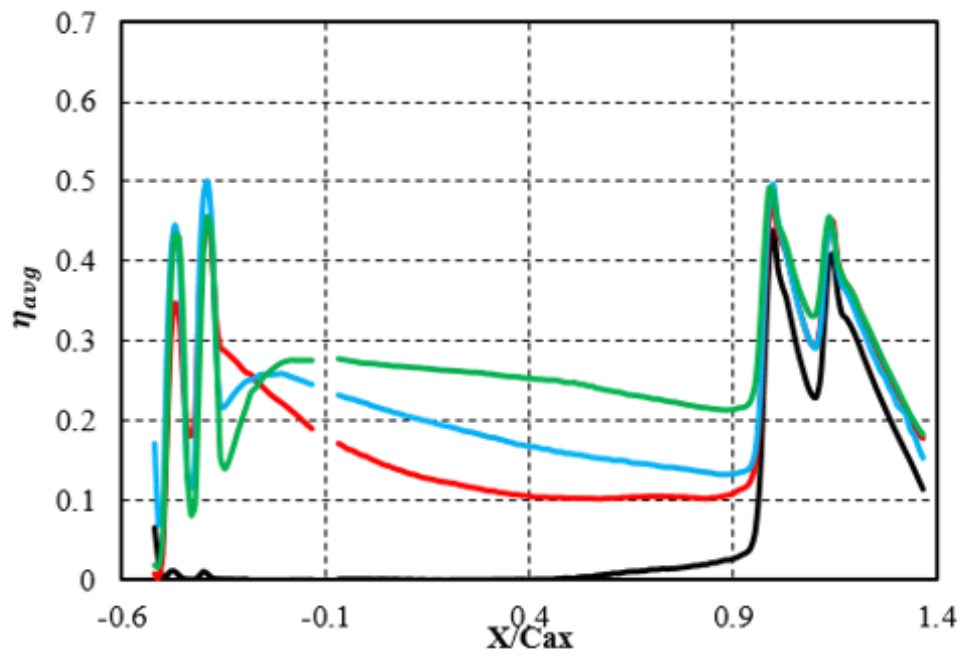


Figure 44 Local film cooling effectiveness,  $EW=1.0\%$ ,  $DR=1.5$

To quantitatively study the MFR effects of upstream injection, Figure 45 (a) and Figure 45 (b) shows the spanwise averaged film cooling effectiveness for the corresponding contours in Figure 44. In both figures, there are four peaks of the effectiveness value, which respectively indicate the upstream two-row injection and the mid-chord/downstream two-row injection. For the upstream two-row injection, the effectiveness value has two peaks at the injection region ( $x/Cax = -0.48$  and  $-0.4$ ), then the effectiveness gradually decreases with increasing  $x/Cax$ . Such cooling effectiveness profiles display the typical two-row film cooling distribution patterns. The effects of MFR ratio on the cooling effectiveness follow the two-row of film cooling patterns as well. It is noticed that at higher MFR ratios, such as  $IL = 1.0\%$  and  $1.5\%$ , the effectiveness value dropped significantly downstream from the second cooling hole due to jet lift-off, then it climbed to a higher level from the valley, which is created by the jet reattachment. For the endwall injection at mid-chord/downstream region, the two injection locations provide the two peak effectiveness values as expected, then the effectiveness value dramatically decreases at further downstream for both designs. For mid-chord configuration, coolant with increasing MFR provides the higher effectiveness; for downstream configuration, coolant with increasing MFR does not provide higher effectiveness as expected. However, the downstream case can provide more diffuse but lower effectiveness distributions as compared to the mid-chord case.



(a) Mid-chord row



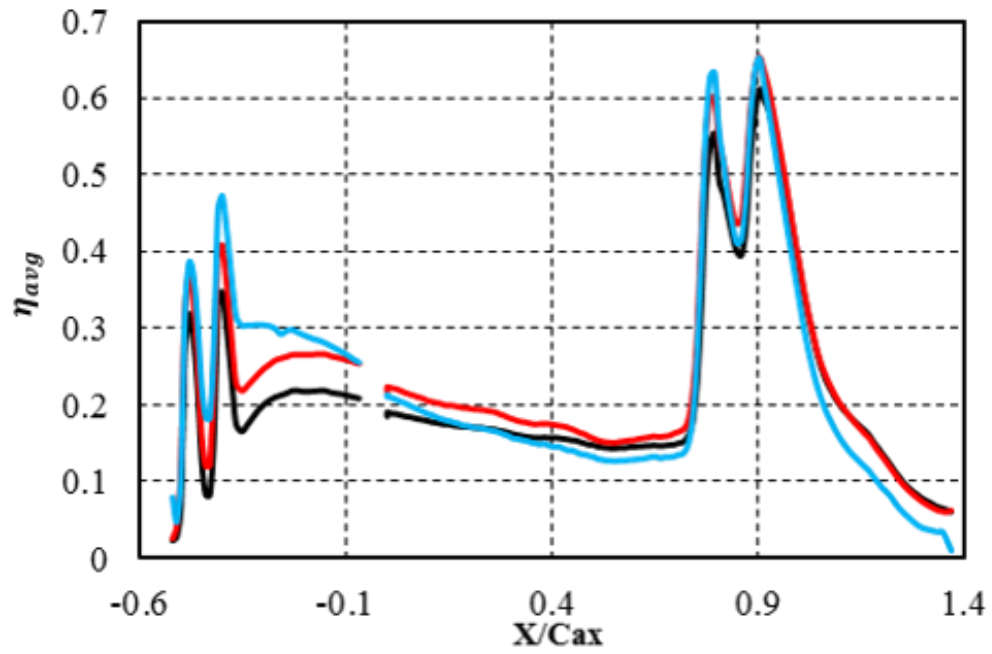
(b) Downstream Row

Figure 45 Pitchwise averaged film cooling effectiveness, EW=1.0%, DR=1.5

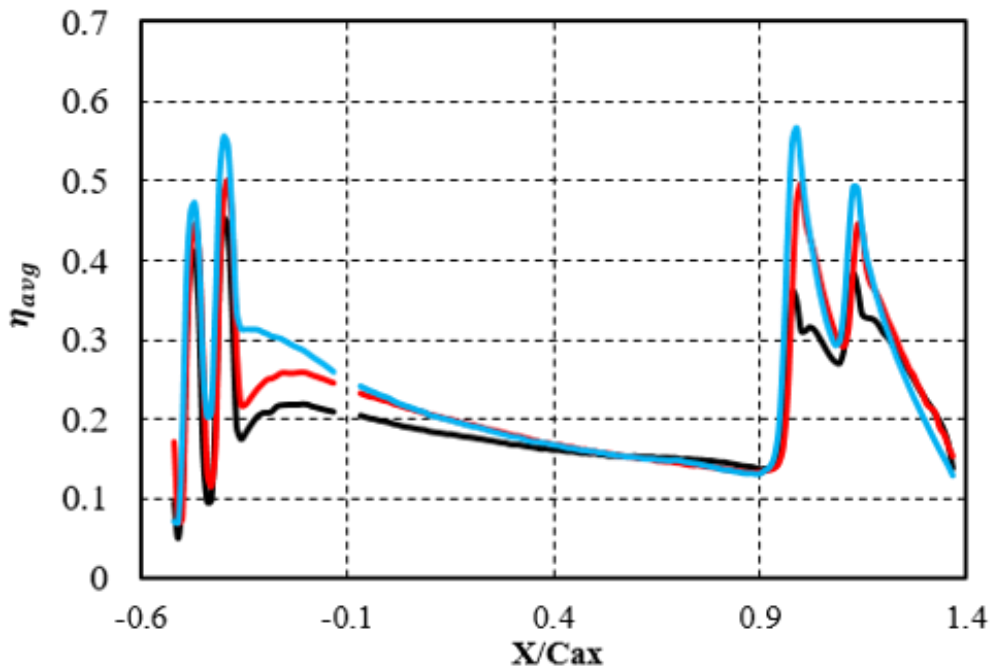
### 4.3.3 Density ratio effect

Coolant-to-mainstream density ratio, one of the parameters affecting the cooling performance, generally shows positive impacts on cooling effectiveness at a given MFR ratio. Coolant with higher DR produces higher cooling effectiveness because at a given MFR, the heavier coolant with less momentum has a lower tendency to lift-off from the surface, providing better thermal protection. Additionally, coolant jet with lower momentum is less interacted and diluted by the mainstream flow. There are three density ratios  $DR = 1.0$ ,  $1.5$ , and  $2.0$  examined in current test, under a fix MFR ratio:  $IL = 1\%$  and  $EW = 1\%$ .

Figure 46 (a) and Figure 46 (b) show the laterally averaged cooling effectiveness distributions for the two cases. A common characteristic is that upstream from the leading edge and downstream from the second upstream injection hole ( $-0.35 < x/Cax < -0.1$ ), the effectiveness distributions suggest the typical density ratio effect on two-row flat plate film cooling, which raises with increasing density ratio from  $DR = 1.0$  to  $DR = 2.0$ . Then downstream from the leading edge to the upstream of the endwall injection, the density ratio effect is gradually reduced. Then downstream from the endwall injection, for the mid-chord row design, higher density ratio coolant produces even slightly lower cooling effectiveness downstream from the endwall ejection region; for the downstream row design,  $DR = 1.5$  and  $2.0$  give equivalent cooling effectiveness level, which is much higher than the  $DR = 1.0$  case near the endwall injection region. Therefore, for both endwall cooling configurations, the density ratio effect is very limited, and coolants with mid-to-high density ratio show a similar cooling effectiveness level.



(a) Mid-chord row



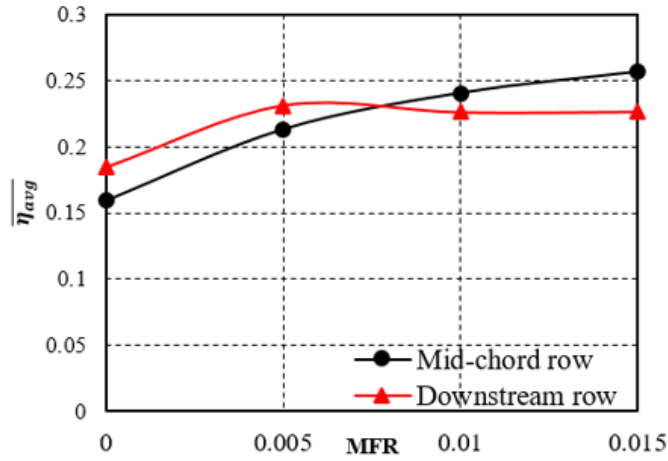
(b) Downstream Row

— DR = 1.0    — DR = 1.5    — DR = 2.0

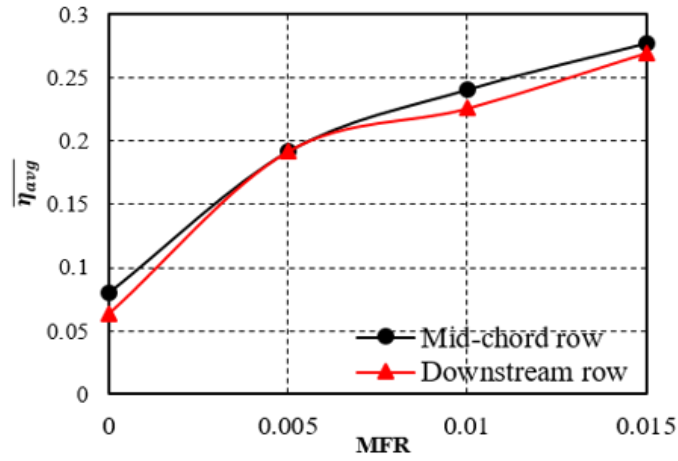
Figure 46 Pitchwise averaged film cooling effectiveness, IL = 1%, EW = 1%

#### 4.3.4 Area-averaged film cooling effectiveness comparison

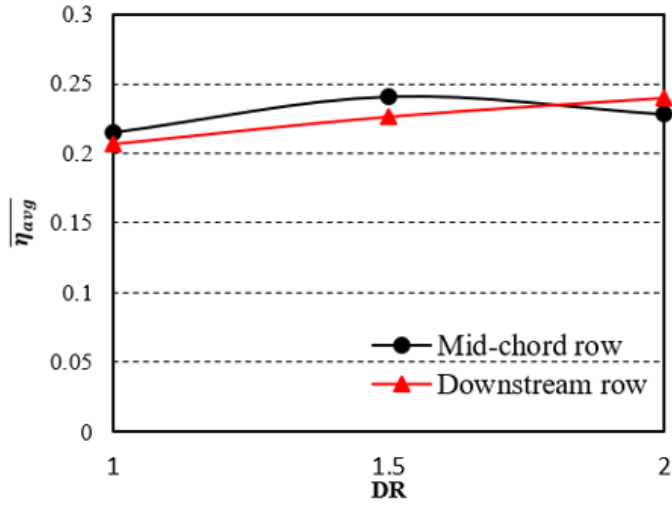
Figure 47 (a) shows the area averaged cooling effectiveness on the endwall passage for varying the endwall injection. Since the upstream injection is fixed at  $IL = 1.0\%$ , it shows the area-averaged effectiveness increases from around 0.17 to around 0.24 for the two cases when the endwall injection increase from  $EW=0$  to  $EW = 1.5\%$ . Figure 47 (b) shows the results for varying the upstream injection, and the area-averaged effectiveness is improved from around 0.06 to 0.27 when the upstream injection increases from  $IL = 0$  to  $IL=1.5\%$ . By comparing the two figures, it shows the upstream injection effect is more pronounced than the endwall injection because the cooling effectiveness increases rapidly with the increase of upstream injection. Figure 47 (c) indicates the area-averaged cooling effectiveness concerning the density ratio variation. The cooling effectiveness curves are quite flat as  $DR$  increases from  $DR = 1.0$  to  $2.0$  for both cases, so it is reasonable to conclude that the density ratio effects on the current endwall cooling design are very mild.



(a) Endwall injection MFR effect, IL=1%, DR = 1.5



(b) Upstream injection MFR effect, EW=1%, DR = 1.5



(c) Density ratio effect, IL = 1%, EW = 1%

**Figure 47 Area averaged film cooling effectiveness**

## 4.4 Conclusions

Film effectiveness distributions were measured on the endwall surface in a four-passage cascade for two endwall film cooling configurations: the mid-chord row configuration and the downstream row design. The endwall cooling is incorporated with the upstream injection in front of the vane leading edge. The tests were performed under various cooling conditions to optimize the coolant distribution between the upstream and endwall injection. The main conclusions are summarized below:

1. Endwall injection effect. The endwall injection does not influence the cooling distribution upstream of the endwall ejection. Coolant with higher MFR ratio gives the higher cooling effectiveness for the mid-chord row cases, but may not provide the desired film cooling results for the downstream row cases. The overall film cooling effectiveness increases slowly and within limits as the endwall injection increases.

2. Upstream injection effect. The cooling effectiveness significantly increases with the increasing of upstream MFR ratio for both configurations. When the MFR ratio is sufficiently strong, the film covered area is increased, and the protected zone can be extended further downstream.

3. Density Ratio effect. Upstream from the leading edge, higher density ratio produces higher cooling effectiveness, which can be considered as the typical two-row flat plate film cooling case. The DR effect on the endwall passage is minimal. It just influences the area near the injection region, and the higher density ratio gives the higher peak. Regarding the area-averaged film cooling effectiveness, the upstream injection is the most influential; then the effects of the endwall injection takes the second place; the density ratio effect is quite minimal in this study.



4. Geometry effect. The cooling effectiveness distributions given by the downstream row case are more diffusive than the mid-chord row case, although the effectiveness levels are slightly lower.

## 5. SUMMARY

In this study, we investigated three topics: (1) turbine blade leading edge cooling with one row normal or tangential impinging jets, (2) film cooling effectiveness from two-row of compound angled cylindrical holes using PSP technique, (3) turbine vane endwall film cooling from mid-chord or downstream rows and upstream coolant injection. Topic (1) used the transient liquid crystal method to measure the internal heat transfer coefficient. Topic (2) and Topic (3) used the PSP technique to measure the external film cooling effectiveness. The realizable  $k-\epsilon$  (RKE) turbulence model was selected for the numerical simulation. The important conclusions are summarized as the followings:

In Topic 1, we investigated the effect of jet impinging position on the leading edge heat transfer. Secondly, the effect of surface curvature and the effect of camera viewing angle. It is found that without viewing angle correction, an error up to 15% under-prediction can be seen in the derived Nusselt numbers. The local Nusselt numbers increase with increasing jet Reynolds number. The normal jet impingement produces circular heat transfer contour, the tangential jet produces the tear-drop contours. The tangential jet provides more uniform heat transfer distribution than the normal jet, but the area averaged Nusselt numbers are similar.

In Topic 2, we studied the film cooling performance of two-row of compound angle cylindrical hole with two hole-geometries is investigated by PSP technique. Results show that at higher blowing ratio conditions, design B is preferred over design A. The film effectiveness is less influenced by density ratio compared to the blowing ratio effect and geometry effect. Large hole-spacing ( $p/d = 6$  or  $8$ ) is not favorable. Because it causes non-uniform film cooling effectiveness distribution in the spanwise direction, the area between cooling holes hardly can be protected. For  $M = 0.5$  and  $1.0$ , design A is better than design B; for  $M = 1.5$ , design A is a little better at high-

density ratio ( $DR = 2.0$ ) and design B is a little better at low-density ratio ( $DR = 1.0$  and  $1.5$ ); for  $M = 2.0$ , design B is better than design A. Lastly, the Two-row flat plate film cooling correlations was developed.

In Topic 3, we measured the film effectiveness distributions on the endwall surface in a four-passage cascade for two endwall film cooling configurations: the mid-chord row configuration and the downstream row design. The main conclusions are obtained. Coolant with higher MFR ratio gives the higher cooling effectiveness for the mid-chord row cases, but may not provide the desired film cooling results for the downstream row cases. The cooling effectiveness significantly increases with the increasing of upstream MFR ratio for both configurations. The DR effect on the endwall passage is minimal. The cooling effectiveness distributions given by the downstream row case are more diffusive than the mid-chord row case, although the effectiveness levels are slightly lower.

## REFERENCES

1. Han, J.C., 2018, Advanced Cooling in Gas Turbines 2016 Max Jakob Memorial Award Paper,” ASME J. Heat Transfer, Vol. 140(11), pp. 113001.
2. Amano, R.S., Sundén, B, 2014, Impingement Jet Cooling in Gas Turbines, WIT Press.
3. Weigand, B. and Spring, S., 2011, “Multiple Jet Impingement –A Review,” Heat Transfer Research, vol.42, no.2, pp. 101-142.
4. Wright, L.M., Han, J.C., 2013, “Heat Transfer Enhancement for Turbine Blade Internal Cooling,” ASME Paper No. HT2013-17813.
5. Chupp, R. E., Helms, D. E., McFadden, P. W., and Brown, T. R., 1969, “Evaluation of Internal Heat Transfer Coefficients for Impingement Cooled Turbine Airfoils,” AIAA J. of Aircraft, Vol. 6(3), pp. 203-208.
6. Florschuetz, L.W. and Isoda, Y., 1982, “Flow distributions and discharge coefficient effects for jet array impingement with initial crossflow,” Journal of Engineering for Power, 105: 3.
7. Florschuetz, L.W., Truman, C.R., and Metzger, D.E., 1981, “Streamwise Flow and Heat Transfer Distributions for Jet Array Impingement with Crossflow,” ASME J. Heat Transfer, Vol. 103, pp. 337-342.
8. Florschuetz, L. W., Berry, R. A., and Metzger, D. E., 1980, “Periodic Streamwise Variations of Heat Transfer Coefficients for Inline and Staggered Arrays of Circular Jets with Crossflow of Spent Air,” ASME J. Heat Transfer, Vol. 102, pp.132–137.
9. Huang, Y., Ekkad, S. V., and Han, J. C., 1998, “Detailed Heat Transfer Coefficient Distributions Under an Array of Inclined Impinging Jets Using a Transient Liquid Crystal

Technique,” 9th International Symposium on Transport Phenomenon in Thermal Fluids Engineering, ISTP-9, Singapore, June 25–28.

10. Ekkad, S.V., Huang, Y., and Han, J.C., 1999, "Impingement Heat Transfer on Target Plate with Film Cooling Holes,” *AIAA J. Thermophysics and Heat Transfer*, Vol. 13, No. 4, pp. 522-528
11. Jordan, C.N., Wright, L.M., and Crites, D.C., 2012, “Impingement Heat Transfer on a Cylindrical, Concave Surface with Varying Jet Geometries,” *ASME Paper No. GT2012-68818*.
12. Jordan, C.N., Wright, L.M., and Crites, D.C., 2012, “Effect of Impingement Supply Condition on Leading Edge Heat Transfer with Rounded Impinging Jets,” *ASME Paper No. HT2012-58410*.
13. Jordan, C.N., Elston, C.A., Wright, L.M., and Crites, D.C., 2013, “Leading Edge Impingement with Racetrack-shaped Jets and Varying Inlet Supply Conditions,” *ASME Paper No. GT2013-94611*
14. Azad, G. M., Huang, Y., and Han, J. C., 2000, “Jet Impingement Heat Transfer on Pinned Surfaces Using a Transient Liquid Crystal Technique,” *Proceedings of the 8th International Symposium on Transport Phenomena and Dynamics of Rotating Machinery*, pp. 731–738.
15. Azad, G. M., Huang, Y., and Han, J. C., 2000, “Jet Impingement Heat Transfer on Dimpled Surfaces Using a Transient Liquid Crystal Technique,” *AIAA J. Thermophysics. Heat Transfer*, 14(2), pp. 186–193.
16. Mhetras, S., Han, J.-C., and Huh, M., 2014, “Impingement Heat Transfer from Jet Arrays on Turbulent Target Walls at Large Reynolds Numbers,” *ASME Transactions Journal of Thermal Science and Engineering Applications*, Vol. 6, No.2, pp. 021003-1 to 021003-10.

17. Buzzard, W., Ren, Z., Ligrani, P., Nakamata, C., and Ueguchi, S., 2016, "Influences of Target Surface Roughness on Impingement Jet Array Heat Transfer: Part 1: Effects of Roughness Pattern, Roughness Height, and Reynolds Number," ASME Paper No. GT2016-56354
18. Buzzard, W., Ren, Z., Ligrani, P. M., Nakamata, C., and Ueguchi, S., 2016, "Influences of Target Surface Roughness on Impingement Jet Array Heat Transfer: Part 2: Effects of Roughness Shape, and Reynolds Number," ASME Paper No. GT2016-56355
19. Kumar, B.V.N.R. and Prasad, B.V.S.S.S., 2000, "Computational investigation of flow and heat transfer for a row of circular jets impinging on a concave surface," ASME Paper No. GT2006-90851.
20. Kumar, B.V.N.R. and Prasad, 2008, B.V.S.S.S.P, "Computational flow and heat transfer of a row of circular jets impinging on a concave surface," Heat Mass Transfer pp. 667–678.
21. Ling, J. P. C. W., Ireland, P. T., and Harvey, N. W., 2006, "Measurement of Heat Transfer Coefficient Distributions and Flow Field in a Model of a Turbine Blade Cooling Passage with Tangential Injection," ASME Paper GT2006-90352.
22. Taslim, M.E., Bethka, D., 2009, "Experimental and numerical impingement heat transfer in an airfoil leading-edge cooling channel with cross-flow," ASME J. Turbomach, vol. 131, pp. 011–021.
23. Xing, Y., Spring, S., and Weigand, B., 2010, "Experimental and Numerical Investigation of Heat Transfer Characteristics of Inline and Staggered Arrays of Impinging Jets," Journal of Heat Transfer, vol. 132, pp. 092201-1-092201-11.

24. Liu, Z., and Feng, Z.P., 2011, "Numerical simulation on the effect of jet nozzle position on impingement cooling of gas turbine blade leading edge," *Int. J. Heat Mass Transfer*, vol. 54, pp. 4949-4959.
25. Hossain, J., Garrett, C. Curbelo, A., Harrington, J., Wang, W. P., Kapat, J., 2016, "Use of Rib Turbulators to Enhance Post-impingement Heat Transfer for Curved Surface," ASME Paper No. GT2016-56638.
26. Parbat, S. N., Siw, S. C., and Chyu, M., 2016, "Impingement Cooling in Narrow Rectangular Channel with Novel Surface Features," ASME Paper No. GT2016-58084.
27. Ekkad, S.V., and Han, J.C, 2000, "A transient liquid crystal thermography technique for gas turbine heat transfer measurements," *Measurement Sci. Technol.* Vol. 11 pp. 957–968.
28. Han, J. C., and Ekkad, S., 2001, "Recent Development in Turbine Blade Film Cooling," *International Journal of Rotating Machinery*, 7(1), pp. 21-40.
29. Bunker, R. S., 2005, "A Review of Shaped Hole Turbine Film-Cooling Technology," *ASME J. Heat Transfer*, 127(4), pp. 441-453.
30. Bogard, D. G., and Thole, K. A., 2006, "Gas Turbine Film Cooling," *AIAA Journal of Propulsion and Power*, 22, pp. 249- 270.
31. Han, J. C., and Rallabandi, A., 2010, "Turbine Blade Film Cooling Using PSP Technique," *Frontiers in Heat and Mass Transfer (FHMT)*, 1, pp. 013001.
32. Ekkad, S. V., and Han, J. C., 2013, "A Review of Hole Geometry and Coolant Density Effect on Film Cooling," ASME Paper No. HT2013-17250.
33. Kianpour, E., Sidik, N. A. C., and Golshokouh, I., 2014, "Film Cooling Effectiveness in a Gas Turbine Engine: A Review," *Jurnal Teknologi*, 71(2), pp. 25-35.

34. Ito, S., Goldstein, R. J., and Eckert, E. R. G., 1978, "Film Cooling of a Gas Turbine Blade," ASME J. Eng. Power, 100(3), pp. 476–481.
35. Sinha, A. K., Bogard, D., and Crawford, M., 1991, "Film Cooling Effectiveness Downstream of a Single Row of Holes with Variable Density Ratio," ASME J. Turbomach., 113(3), pp. 442-449.
36. Haas, W., Rodi, W., and Schonung, " B., 1992, "The Influence of Density Difference Between Hot and Coolant Gas on Film Cooling by a Row of Holes: Predictions and Experiments," ASME J. Turbomach., 114(4), pp. 747–755.
37. Ekkad, S. V., Zapata, D., and Han, J. C., 1997, "Film Effectiveness over a Flat Surface with Air and CO<sub>2</sub> Injection through Compound Angle Holes using a Transient Liquid Crystal Image Method," ASME J. Turbomach., 119(3), pp. 587-593.
38. Goldstein, R. J., and Jin, P., 2001, "Film Cooling Downstream of a Row of Discrete Holes With Compound Angle," ASME J. Turbomach., 123(2), pp. 222–230
39. Lutum, E., Johnson, B. S., 1999, "Influence of the Hole Length-to-Diameter Ratio on Film Cooling with Cylindrical Holes," ASME J. Turbomach., 121(2), pp. 209-216.
40. Chen, A., Li, S. J., and Han, J. C., 2014, "Film Cooling for Cylindrical and Fan-Shaped Holes Using Pressure-Sensitive Paint Measurement Technique," AIAA Journal of Thermophysics and Heat Transfer, 29(4), pp. 1-10.
41. Jabbari, M.Y., Goldstein, R.J., 1978, "Adiabatic wall temperature and heat transfer downstream of injection through two rows of holes," ASME J. Eng. Power, 100(2), 303–307.



42. Jubran, B., and Brown, A., 1985, "Film Cooling from Two rows of Holes Inclined in the Streamwise and Spanwise Directions," *ASME J. Eng. Gas Turbines Power*, 107(1), pp. 84-89.
43. Sinha, A.K., Bogard, D.G., Crawford, M.E., 1991, "Gas turbine film cooling: flowfield due to a second row of holes," *ASME J. Turbomach.*, 113(3), pp. 450–456.
44. Ligrani, P.M., Wigle, J.M., Criello, S., Jackson, S.M., 1994, "Film cooling from holes with compound angle orientations: part 1— results downstream of two staggered rows of holes with 3d spanwise spacing," *ASME J. Heat Transfer*, 116(2), pp. 341–352.
45. Ahn, J., Jung, I. S., Lee, J. S., 2003, "Film cooling from two rows of holes with opposite orientation angles: injectant behavior and adiabatic film cooling effectiveness," *International Journal of Heat and Fluid Flow*, Vol. 21, pp. 91-99.
46. Jubran, B. A., Al-Hamadi, A., and Theodoridis, G., 1997, "Film Cooling and Heat Transfer with Air Injection through Two Rows of Compound Angle Holes," *Heat and Mass Transfer*, 33(1-2), pp. 93-100.
47. Jubran, B. A., and Maiteh, B. Y., 1999, "Film Cooling and Heat transfer from a Combination of Two rows of Simple and/or Compound Angle Holes in Inline and/or Staggered Configuration," *Heat and Mass Transfer*, 34, pp. 495-502.
48. Maiteh, B. Y., and Jubran, B. A., 2004, "Effects of Pressure Gradient on Film Cooling Effectiveness from Two Rows of Simple and Compound Angle Holes in Combination," *Energy Conversion and Management*, 45, pp. 1457-1469.
49. Yang, W., Liu, X., Li, G., Zhang, J., 2012, "Experimental Investigation on Heat Transfer Characteristics of Film Cooling Using Parallel-inlet Holes," *Int. J. Therm. Sci.*, 60, pp. 32-40.

50. Bashir, M. H., Shiau, C. C., Han, J. C., 2017, "Film Cooling Effectiveness for three-row compound angle hole design on flat plate using PSP technique," *International Journal of Heat and Mass Transfer*, 115, pp.918-929.
51. Jones, T. V., 1999 "Theory for the use of foreign gas in simulating film cooling", *International Journal of Heat and Fluid Flow*, 20(3), pp. 349-354.
52. Bunker, R. S., 2017, "Evolution of Turbine Cooling," ASME Paper No. GT2017-63205.
53. Han, J. C., 2013, "Fundamental Gas Turbine Heat Transfer," *ASME J. Thermal Sci. Eng. Appl.*, 5(2), p. 021007.
54. Ghosh, K. and Goldstein, R. J., 2012, "Effect of Inlet Skew on Heat/Mass Transfer from a Simulated Turbine Blade," *ASME J. Turbomach.*, 134(5), p. 051042.
55. Blair, M. F., 1974, "An Experimental Study of Heat Transfer and Film Cooling on Large-Scale Turbine Endwalls," *ASME J. Heat Trans.*, 96(4), pp. 524-529.
56. Granser, D. and Schulenberg, T., 1990, "Prediction and Measurement of Film Cooling Effectiveness for a First-Stage Turbine Vane Shroud," ASME Paper No. 90-GT-95.
57. Burd, S. W. and Simon, T. W., 2000, "Effects of Slot Bleed Injection Over a Contoured Endwall on Nozzle Guide Vane Cooling Performance: Part I: Flow Field Measurements," ASME Paper No. 2000-GT-199.
58. Zhang, L. and Jaiswal, R. S., 2001, "Turbine Nozzle Endwall Film Cooling Study Using Pressure-Sensitive Paint," *ASME J. Turbomach.*, 123(4), pp. 730-738.
59. Liu, G., Liu, S., Zhu, H., Lapworth, B. C., and Forest, A.E., 2004, "Endwall Heat Transfer and Film Cooling Measurements in a Turbine Cascade with Injection Upstream of Leading Edge," *Heat Transfer–Asian Research*, 33, pp. 141-152.

60. Knost, D. G. and Thole, K. A., 2005, "Adiabatic Effectiveness Measurements of Endwall Film-Cooling for a First-Stage Vane," ASME J. Turbomach., 127(2), pp. 297-305.
61. Zhang, L., Yin, J., Liu, K., and Moon, H. K., 2015, "Effect of Hole Diameter on Nozzle Endwall Film Cooling and Associated Phantom Cooling," ASME Paper No. GT2015-42541.
62. Chowdhury, N. H. K., Shiau, C. C., Han, J. C., Zhang, L., and Moon H. K., 2017, "Turbine Vane Endwall Film Cooling Study from Axial-Row Configuration with Simulated Upstream Leakage Flow," ASME Paper No. GT2017-63144.
63. Chowdhury, N. H. K., Shiau, C. C., Han, J. C., Zhang, L., and Moon H. K., 2017, "Turbine Vane Endwall Film Cooling from Cross-Row Configuration with Simulated Upstream Leakage Flow," ASME Paper No. GT2017-63145.
64. Chowdhury, N. H. K., Shiau, C. C., Han, J. C., Xu, H., and Fox M., 2017, "Film Cooling Effectiveness Comparison on Turbine Vane Endwall with Cluster Configurations Using PSP Measurement Technique," ASME Paper No. IMECE2017-72157.
65. Kline, S., and McClintock, F., 1953, "Describing Uncertainties in Single-Sample Experiments", Mechanical Engineering, 75(1), pp. 3 – 8.